

**UNCLASSIFIED**

---

**AD 295154**

*Reproduced  
by the*

**ARMED SERVICES TECHNICAL INFORMATION AGENCY  
ARLINGTON HALL STATION  
ARLINGTON 12, VIRGINIA**



---

**UNCLASSIFIED**

NOTICE: When government or other drawings, specifications or other data are used for any purpose other than in connection with a definitely related government procurement operation, the U. S. Government thereby incurs no responsibility, nor any obligation whatsoever; and the fact that the Government may have formulated, furnished, or in any way supplied the said drawings, specifications, or other data is not to be regarded by implication or otherwise as in any manner licensing the holder or any other person or corporation, or conveying any rights or permission to manufacture, use or sell any patented invention that may in any way be related thereto.

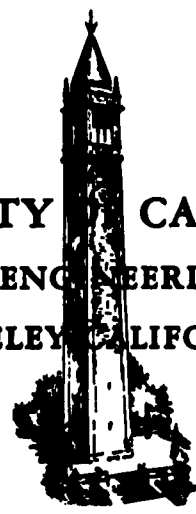
63-2-3

295154  
295154

CATALOGED BY ASTIA  
AS AD NO. \_\_\_\_\_

TECHNICAL REPORT  
HE-150-205

UNIVERSITY OF CALIFORNIA  
INSTITUTE OF ENGINEERING RESEARCH  
BERKELEY, CALIFORNIA



---

HYPERSONIC FLOW OVER A SLENDER CONE WITH GAS INJECTION

---

by

Hartley H. King

ASTIA  
1963  
JAN 1963

SERIES NO.....196.....  
ISSUE NO.....1.....  
DATE.....November 5, 1962.....

G.E. PURCHASE ORDER 214-J91534  
and CONTRACT N-onr-222(45)  
REPORT NO. HE-150-205  
SERIES NO. 196-1  
NOVEMBER 5, 1962

JOINTLY SPONSORED BY  
THE GENERAL ELECTRIC COMPANY  
THE OFFICE OF NAVAL RESEARCH AND  
THE OFFICE OF SCIENTIFIC RESEARCH

---

**HYPERSONIC FLOW OVER A SLENDER CONE WITH GAS INJECTION**

---

by

Hartley H. King

Submitted in partial satisfaction  
of the requirements for the  
degree of Doctor of Philosophy  
in Mechanical Engineering

Reproduction in whole or in part is permitted  
for any purpose of the United States Government

**FACULTY INVESTIGATORS:**

L. TALBOT, ASSOCIATE PROFESSOR OF AERONAUTICAL SCIENCES  
S. A. SCHAAF, PROFESSOR OF ENGINEERING SCIENCES  
G. J. MASLACH, PROFESSOR OF AERONAUTICAL ENGINEERING

Approved: *L. Talbot*

G.E. PURCHASE ORDER 214-J91534  
and CONTRACT N-onr-222(45)  
REPORT NO. HE-150-205  
SERIES NO. 196-1  
NOVEMBER 5, 1962

JOINTLY SPONSORED BY  
THE GENERAL ELECTRIC COMPANY  
THE OFFICE OF NAVAL RESEARCH AND  
THE OFFICE OF SCIENTIFIC RESEARCH

---

**HYPERSONIC FLOW OVER A SLENDER CONE WITH GAS INJECTION**

---

by

Hartley H. King

Submitted in partial satisfaction  
of the requirements for the  
degree of Doctor of Philosophy  
in Mechanical Engineering

Reproduction in whole or in part is permitted  
for any purpose of the United States Government

**FACULTY INVESTIGATORS:**

L. TALBOT, ASSOCIATE PROFESSOR OF AERONAUTICAL SCIENCES  
S. A. SCHAAF, PROFESSOR OF ENGINEERING SCIENCES  
G. J. MASLACH, PROFESSOR OF AERONAUTICAL ENGINEERING

Approved: *L. Talbot*

## TABLE OF CONTENTS

	<u>Page</u>
ABSTRACT	1
LIST OF FIGURES	iv
LIST OF SYMBOLS	vi
1.0 SUMMARY OF RESULTS AND DISCUSSION	1
1.1 Introduction	1
1.2 Experimental Program	1
1.3 Models	2
1.4 Reduction of the Data	4
1.5 Experimental Pressure Results	5
1.6 Experimental Drag Results	7
1.7 Theoretical Analysis	9
1.8 Comparison of Pressure Data with Theory	10
1.9 Comparison of Experimental and Theoretical Drag Data	12
1.10 Conclusions	15
2.0 EXPERIMENTAL PROCEDURE AND DATA REDUCTION	16
2.1 Operation of the Wind Tunnel	16
2.2 Mounting of the Models	17
2.3 Pressure Distribution Measurements	17
2.4 Pressure Data Reduction	20
2.5 Drag Force Measurements	21
2.6 Skin Friction Drag	23
2.7 Pressure Drag	23
2.8 Base Drag	24

	<u>Page</u>
2.9 Injection Drag	25
2.10 Injection Pressure vs. Flow Rate	29
2.11 Local Mass Flux Distribution	30
2.12 Injection Flow Metering	31
3.0 BOUNDARY LAYER ANALYSIS	33
3.1 Objective and Assumptions	33
3.2 Inviscid Flow	34
3.3 Displacement Thickness	35
3.4 Injection Mass Flow Rate	38
3.5 Solution Method	39
3.6 Transverse Curvature Effect	41
REFERENCES	46
APPENDIX	49
FIGURES	68

## LIST OF FIGURES

1. Low Density Wind Tunnel
2. Wind Tunnel and Experimental Instrumentation
3. Drag Force Apparatus
4. Pressure Distribution Apparatus
5. Test Models
6. Model Dimensions
7. Injection Flow and Pressure Systems
8. Mounting of the Force Model
9. Afterbody and Sting-Shield Geometry
10. Uncorrected Experimental Pressure Distribution for Zero Injection
11. Induced Surface Pressure at Tap No. 1
12. Induced Surface Pressure at Tap No. 2
13. Induced Surface Pressure at Tap No. 3
14. Induced Surface Pressure at Tap No. 4
15. Induced Surface Pressure at Tap No. 5
16. Induced Surface Pressure at Tap No. 6
17. Cross-Plots of Surface Pressure Data (Mach 3.93)
18. Cross-Plots of Surface Pressure Data (Mach 5.64)
19. Gross Drag Coefficient Experimental Data
20. Base Pressure Data Taken During the Force Data Runs
21. Paired Experimental Total Drag Data
22. Drag Contributions Based on Experimental Data (Mach 3.93)
23. Drag Contributions Based on Experimental Data (Mach 5.64)
24. Comparison of Measured Self-Induced Pressures with Values Predicted by the Present Theory (Mach 3.93)

25. Comparison of Measured Self-Induced Pressures with Values Predicted by the Present Theory (Mach 5.64)
26. Relation Between Injection Parameter  $f_w$  and the Total Injection Rate (from Present Theory)
27. Theoretical Influence of Viscous Interaction on the Injection Law for Constant  $f_w$  Parameter
28. Displacement Boundary Layer Thickness from the Present Theory
29. Effect of Viscous Interaction and Transverse Curvature on Total Drag According to the Present Theory, and Comparison with Experimental Data (Mach 3.93)
30. Effect of Viscous Interaction and Transverse Curvature on Total Drag According to the Present Theory, and Comparison with Experimental Data (Mach 5.64)
31. Effect of Viscous Interaction on Local Skin Friction According to the Present Theory
32. Impact Pressure Survey for the Mach 3.93 Nozzle
33. Impact Pressure Survey for the Mach 5.64 Nozzle
34. Test Model Temperatures Measured at the Cone Base
35. Porous Model Flow Characteristics
36. Determination of the Axial Injection Distribution
37. Data for the Determination of Local Mass Flux
38. Approximate Local Mass Flux Distribution Based on Data Presented in Figure 37

## LIST OF SYMBOLS

### English Letter Symbols

A	area or transverse curvature parameter (Eq. 3.15)
C	Chapman-Rubesin factor (Eq. 3.4)
$C_D$	drag coefficient
D	drag force
$f_w$	non-dimensional injection rate parameter (Eq. 3.7)
$f_w''$	non-dimensional velocity gradient at the wall
$K_w$	helium concentration multiplier (Baron's <sup>5</sup> $\lambda$ function)
L	axial length of the cone models (3.50 inches)
$L_1$	characteristic diameter of the porous passages
$s$	slant length of the cone
M	Mach number or molecular weight
$\dot{M}$	total mass injection rate
$\dot{m}$	local injection mass flux, equal to $\rho_w v_w$
P	pressure
R	gas constant
Re	Reynolds number
$r_w$	local cone surface radius (equal to $x \sin \alpha$ )
T	temperature
t	model wall thickness
u	velocity, x direction velocity in the boundary layer
v	y direction velocity in the boundary layer
x	distance along cone ray from apex
y	distance normal to cone surface
Z	axial distance along the cone (equal to $x \cos \alpha$ )

### Greek Letter Symbols

$\alpha$	cone apex half-angle ( $5^\circ$ for the present tests)
$\beta$	tangent cone theory angle (Eq. 3.1)
$\gamma$	specific heats ratio for air
$\delta^*$	boundary layer displacement thickness
$\lambda$	mean free path length
$\mu$	viscosity
$\rho$	density
$\sigma$	recovery factor
$\omega$	mass concentration of helium

### Subscripts

aw	adiabatic wall
b	base
c	inviscid conical flow value
e	external
f	skin friction
g	gross (defined in Section 2.5)
i	internal
inj	injection
M	without viscous interaction or transverse curvature
p	pressure
s	stagnation
TVC	with transverse curvature
VI	with viscous interaction
w	wall
$\delta$	at the outer edge of the boundary layer

## 1.0 SUMMARY OF RESULTS AND DISCUSSION

### 1.1 Introduction

Aerodynamic behavior in the hypersonic low density regime is governed by a complicated interaction between the boundary layer and the outer flow over the body.<sup>1-4</sup> Gas injection (or ablating surface material) can increase greatly the displacement thickness of the boundary layer,<sup>5,6</sup> and thus affect profoundly this entire viscous interaction phenomenon. An interesting and important aspect of mass transfer, therefore, is its effect on the aerodynamic behavior of a slender body in low Reynolds number flow.

The main object of the present study was the experimental investigation of the effect of gas injection on the drag and pressure distribution on a 5° half-angle porous cone. Both helium and air injection were employed at two Mach-Reynolds number combinations attainable in the Berkeley Low Density Wind Tunnel. The first part of the report presents a general discussion of the experiment, the experimental data obtained, and the comparison of these data with theory. Section 2 is a detailed discussion of the experimental procedure and the methods of data reduction, while Section 3 presents the approximate boundary layer analysis which is useful for interpreting the experimental data. A discussion of the accuracy of the various experimental results and tabulations of data appear in the Appendix.

### 1.2 Experimental Program

The experiments were conducted in the No. 4 Low Density Wind Tunnel of the University of California Low Pressures Project (Figures 1

and 2). This is a free-jet, continuous flow facility which expands room temperature air through an axi-symmetric nozzle to a test chamber pressure of about 85 microns of mercury. The flow characteristics of the two nozzles used in the present experiment have been described in previous reports,<sup>7,8</sup> and additional data are presented herein. The injection gas was introduced into the model interior through a hollow tail sting located inside a conical afterbody (Figures 3 and 4). The experimental program consisted of the following:

I. Two free-stream air flow conditions

- a.  $M_\infty = 3.93$ ,  $Re/in = 1765$ ,  $T_g = 540^\circ R$ ,  $P_\infty = 85$  microns Hg.
- b.  $M_\infty = 5.64$ ,  $Re/in = 6200$ ,  $T_g = 539^\circ R$ ,  $P_\infty = 85$  microns Hg.

II. Primary measurements

- a. Surface static pressures at six axial stations on the cone surface
- b. Gross drag force on the cone

III. Secondary measurements

- a. Base pressure (between the cone model and afterbody)
- b. Model surface temperature
- c. Axial distribution of injection mass flux
- d. Flow characteristics of the porous surfaces of the models
- e. Impact pressure surveys of the wind tunnel test section.

### 1.3 Models

All models used in the experiments were  $5^\circ$  cones of 3.5 inch length, and are shown in Figures 5 and 6. The porous models were of uniform wall thickness and because of fabrication requirements had small

solid tip and base regions. The two porous-wall pressure models (called the "1,3,5" and "2,4,6" models) each had three in-line taps made by attaching 0.040 I.D. x 0.007 inch wall stainless steel tubing to the surface with epoxy resin. A third model without taps (called the "force" model) was used for the drag force measurements. The porous models were fabricated commercially from sintered powdered Monel metal particles of less than 0.0005 inch diameter.

Apparently the small size of the porous models caused some difficulty in their manufacture, since their quality could only be described as "fair". The biggest difficulty seemed to be the installation of the pressure taps. Although the taps were locally smooth to touch, the stainless steel tubing caused some wrinkling of the thin (0.023 inch) porous wall around the taps, and this apparently caused a systematic error in the pressure measurements on the porous models (discussed in detail later). In addition, the wall inclination appeared to deviate slightly (but symmetrically) from the specified  $5^\circ$  angle where the solid tip was joined to the porous wall. Further back the surface was inclined  $5 \pm 0.03$  degrees.

Because of the relatively poor quality of the two porous pressure models around the tap areas, an additional solid brass model of better surface and tap quality was constructed in order to check the zero-injection pressure distribution data. This is called the "solid pressure model" and was geometrically similar to the porous pressure models and had the same pressure tap construction. Since zero-injection pressure data were obtained from this model in a manner identical to that used for the porous pressure models, the differences in readings (which were as

high as 15% of the absolute pressure, depending on tap location) were attributed to surface roughness and tap geometry errors on the porous models.

An additional series of solid brass models (called the "cone probes") were also used to check the zero-injection pressure distribution and to see if a pressure orifice size effect existed. Each of these models had four 0.016 inch taps located at 90° intervals around the circumference at a location corresponding to one of the porous model pressure taps. All of the non-porous models were constructed on the Berkeley campus.

#### 1.4 Reduction of the Data

The gross drag  $D_g$  of the force model was measured by a null type one-component beam balance,<sup>9</sup> with the injection gas entering through the sting and cone base (Figures 3 and 8). The drag  $D_f$  due to skin friction was obtained indirectly from the relation

$$D_f = D_g - D_p - D_b - D_{inj} \quad (1.1)$$

Here  $D_p$  is the drag due to the slant-face static pressure, and  $D_b$  is the drag due to base pressure, which is a spurious contribution arising from the particular experimental set-up.  $D_p$  was obtained by integrating the experimental pressure distribution curve, and  $D_b$  was determined by measuring the pressure near the cone base inside the hollow afterbody. The injection drag  $D_{inj}$  arises from the momentum transfer associated with the surface effusion of the injected gas, and is a small correction which was evaluated theoretically. The term

"total drag" is used in discussing the drag results and is defined as the sum of the skin friction, pressure, and injection drag for the slant face of the cone (obtained as  $D_g - D_b$  from the experimental data). All data in this report were obtained at zero angle of attack.

The experimental injection rate ranged from zero to about 0.12 lb/hr for helium and about 0.35 lb/hr for air. A non-dimensional injection rate parameter suggested by Swenson<sup>10</sup> is the ratio of injection mass flow to the total air mass swept out by the model cross-section to the flow. In the present experiments this ratio ranged from zero to about 1/5 for helium injection and 1/2 for air injection. However, this parameter is not too useful for physical interpretations of the flow.

Besides their use in the calculation of skin friction drag, the model surface pressure distribution data are themselves of interest. To correct for the previously mentioned tap geometry and hole size effect, the measurements with gas injection were divided by the average zero-injection value for each tap for a given wind tunnel run. This ratio was then multiplied by the corresponding average value of the cone probe pressure data, which was assumed to be the best available zero-injection pressure value for that particular wind tunnel flow condition and tap location. All of the pressure data presented in this report have been corrected by this procedure, which is described in detail in Section 2.

### 1.5 Experimental Pressure Results

Figure 10 shows the raw zero-injection pressure distribution data for the three types of models used in the tests. The average value of three or more wind tunnel measurements is shown, together with bars

which indicate the scatter of the data. One sees that the porous model measurements were up to about 20% higher than the cone probe data, depending on the orifice location, with data from the solid model lying between. The difference between the solid model and porous model data is attributed to the inferior quality of the porous model orifices, as described previously. The difference between the solid model and cone probe data is probably due mainly to the much larger pressure taps on the solid model, since this difference agrees in magnitude with the hole size effect data of Talbot.<sup>2</sup> The curve labeled "standard" is a fairing through the cone probe data, and is taken as the "best" values for the zero-injection pressure distribution. Thus the differences between the porous model zero-injection data and the "standard" curve shown in Figure 10 represent the magnitude of the correction applied to all measurements made with the porous pressure models. The data for this figure are presented in Table I in the Appendix.

The effect of gas injection on the corrected surface pressure at each orifice location is shown in Figures 11 to 16, and the data are presented in Tables II and III. Cross-plots of these data are shown in Figures 17 and 18. The ordinate represents the magnitude of the boundary layer induced pressure increment referred to the theoretical inviscid solution value.<sup>11,12</sup> One sees from these curves that the helium injection increased the self-induced pressure more rapidly than air injection, and that the level of the curves is slightly higher for the higher Mach number flow condition. The data for tap No. 6, nearest the cone base, show a pressure decrease with injection which is probably attributable to the upstream influence of the solid afterbody and the gap at  $Z = 3.5$  inches.

It should be recalled that these data were obtained from two separate models (the 1,3,5 and 2,4,6 models), so that inevitably there are slight discrepancies between the two sets of measurements. This probably accounts for the somewhat unsmooth curves of Figures 17 and 18 for the higher injection rates. A crude measurement of the injection mass distribution (see Figure 38) indicated that the porosity of the two models was roughly the same, except for the area around Tap No. 1 ( $Z = 1.25$  inches), which was less permeable. However, it was found that even though the wall thickness was uniform, the local injection mass flux was up to perhaps 75% higher near the nose than near the base. This may be the reason for the pronounced peak in the curves of Figures 17 and 18 near  $Z = 2.0$  inches.

In order to evaluate the skin friction drag (Equation 1.1), it was necessary to integrate the experimental pressure distribution curves. This is the reason for the dotted curves of Figures 17 and 18, which are more or less arbitrary extrapolations of the data to cover the whole cone surface.

#### 1.6 Experimental Drag Results

Only the "gross" drag was measured directly in the experiment, and the data are presented in Figure 19 and Table IV. It will be recalled, however, that the pressure existing inside the hollow afterbody caused a spurious force contribution which must be added to the gross drag in order to obtain the "total" drag. The base pressure data are shown in Figure 20.

In order to handle the drag results in a convenient manner, "best fit" curves were faired through the gross drag and base pressure

data. Because it also was necessary to obtain the slant-face pressure drag from integrals of the cross-plots of Figures 17 and 18, the various drag contributions have been computed from the faired curves at roughly 15 evenly spaced injection values and appear in Table V in the Appendix. For this reason actual data points do not appear on Figures 21, 22, and 23 showing experimental drag results.

Figure 21 shows the experimental "total" drag results, which were obtained by correcting the data of Figure 19 for the effects of base pressure. (The magnitude of this correction was roughly 10%.) One sees that the injection caused a significant decrease in total drag over the range of injection rates of the experiment. The most interesting feature of these data, however, is that the air injection was more efficient for reducing the total drag than was helium. This contradicts simple boundary layer theory, which predicts that the helium curve should lie below the air injection curve.<sup>13</sup> The bars on the curves indicate the possible uncertainty due to experimental and data reduction errors, as discussed in the Appendix.

The relative magnitudes of the various experimental drag contributions are shown in Figures 22 and 23. Here it may be seen that skin friction drag contributes the largest portion of the total drag. The injection drag is relatively insignificant, although helium injection contributes a greater amount, due to higher efflux velocity, than air at the same mass injection rate. The pressure drag is relatively small at zero injection (about 15% of the total drag), but becomes significant with increasing injection--more so with helium than with air. This is primarily the reason for the larger separation of the air and helium curves of

Figure 21 than the corresponding separation of the air and helium skin friction curves of Figures 22 and 23. However, since the helium skin friction curve is still higher than that for air injection, it cannot be the pressure-plus-injection drag alone that accounts for the greater total drag with helium injection shown in Figure 21.

### 1.7 Theoretical Analysis

In Section 3 an approximate theory is presented which is useful for the interpretation of the experimental data. The basic feature of the analysis is the empirical inclusion of the viscous interaction (VI) effect by adding the boundary layer displacement thickness to the cone.<sup>1-3</sup> The (also empirical) tangent cone theory<sup>3</sup> is employed to compute the flow properties along the edge of this new effective body, and these quantities are then used for the outer edge boundary condition in the boundary layer analysis. Of course since the outer flow affects the boundary layer growth and vice-versa, the tangent cone and boundary layer solutions must be considered simultaneously.

To keep matters as simple as possible, the theoretical flat-plate boundary layer calculations of Baron<sup>5</sup> (helium injection) and Low<sup>6</sup> (air injection) were employed with the aid of the Mangler transformation to axi-symmetric flow. These analyses neglected the pressure gradient term in the boundary layer equations and assumed that the local injection mass flux varied as  $x^{-1/2}$ . The displacement thickness  $\delta^*$  and its slope  $d\delta^*/dx$  were computed at each station  $x$  using the "local similarity" concept,<sup>3</sup> where the previous history of the boundary layer flow is ignored. The results of this series of calculations are labeled VI (viscous interaction) in the appropriate figures.

Because the ratio of displacement thickness to the local cone radius computed from the above theory attained values of the order one to three, it was suspected that transverse curvature (TVC) effects were also likely to be important.<sup>14-16</sup> These effects arise because the order-of-magnitude reduction of the Navier-Stokes equations to the boundary layer equations is different for low Reynolds number flow over a slender body than for the corresponding flow over a flat plate. It is known that the additional TVC terms in the boundary layer equations for slender body flow can produce important changes in the displacement thickness and skin friction over those values computed on the basis of the flat plate equations with Mangler transformation.<sup>14-16</sup>

A transverse curvature (TVC) correction to the previously calculated viscous interaction (VI) results was made, based on the theoretical calculations of Yasuhara.<sup>15</sup> In essence, Yasuhara solved the same boundary layer problems with and without the transverse curvature terms, so that the magnitude of the TVC effect is evident from his results. It should be pointed out, however, that Yasuhara's analysis is only an approximation to the present experimental conditions. In addition, he studied only the zero-injection case, so that the application of his corrections to the present results with injection is extremely speculative. Further details regarding the TVC correction procedure may be found in Section 3.6.

### 1.8 Comparison of Pressure Data with Theory

Figures 24 and 25 show the comparison of the (cross-plotted) pressure data with the results of the present theory for selected values of total mass injection. The parameter  $f_w$  is a dimensionless injection

rate parameter from the analyses of Baron<sup>5</sup> and Low,<sup>6</sup> and this was used as the independent mass injection variable in the present theory. Figure 26 shows the relation between  $f_w$  and the total mass injection rate  $\dot{M}$  for the present experimental conditions, and it may be seen that the theory is available only for about the lower 1/3 of the experimental mass injection values.

One notices from Figures 24 and 25 that the present theory overestimates the boundary layer induced pressure by a factor of about two. The transverse curvature correction is in the proper direction, but its magnitude is too small to bring the theory and experiment into much closer agreement.

It is perhaps not surprising that the theory and experiment disagree. First the theory assumes that the mass injection  $\rho_w v_w$  varies approximately as  $x^{-1/2}$  (although not exactly, as shown in Figure 27 and discussed in Section 3.4). The actual measured injection variation is shown in Figure 38, where the curve for the  $x^{-1/2}$  law is shown for comparison. With an  $x^{-1/2}$  law the injection increases indefinitely as the cone apex is approached, and this accounts for the high self-induced pressure increment  $(P - P_c)/P_c$  predicted by the theory near the nose. The drop-off in experimental pressure near the rear of the cone is probably due to the upstream influence of the solid afterbody and the gap at  $Z = 3.5$  inches.

Other possible sources for the discrepancies between the experimental and theoretical pressure distributions are the use of the tangent cone theory for the inviscid flow, the assumption of local similarity, and the neglect of the pressure gradient terms in the boundary layer

theory. Clearly with  $\delta^*/r_w$  values between one and roughly three (Figure 28), the physical flow must be like that over a blunt body, and the tangent cone theory is therefore suspect. The use of the no-injection transverse curvature results for TVC corrections with injection is probably considerably in error, since one might expect the thicker boundary layers with injection to be proportionally more subject to transverse curvature effects. Finally, it should be noted that the correction procedure used for the experimental pressure data may actually be somewhat in error at the higher injection rates. The effects of these above considerations on the agreement between experiment and theory are very difficult to estimate, and no attempt is made here.

#### 1.9 Comparison of Experimental and Theoretical Drag Data

Figures 29 and 30 show a comparison of the experimental (faired) total drag data with the results of the present theory for the two experimental flow conditions. The curves labeled "No VI or TVC" are based on the analyses of Baron<sup>5</sup> and Low<sup>6</sup> for skin friction drag, but use the inviscid Taylor-Maccoll flow quantities for boundary layer edge values and pressure drag. Thus these curves give the estimated drag based on simple boundary layer theory. The curves labeled "VI" are the results of the present calculations including the viscous interaction effect, as described previously in Section 1.7, and in detail in Section 3. Finally, the curves labeled "VI + TVC" include the estimated transverse curvature correction. In discussing these results it is well to remember that about 75% or more of the total drag is due to skin friction.

It may be seen from Figures 29 and 30 that the inclusion of the viscous interaction and transverse curvature effects produces a considerable

improvement over the usual high Reynolds number boundary layer theory. In fact, for zero-injection the experimental and VI + TVC values for total drag disagree by less than 5% for both flow conditions. Such agreement is undoubtedly fortuitous, considering the empirical nature of the present theory. For example, no-injection weak interaction theory predicts that the local skin friction coefficient  $C_f$  should increase slightly over the no-interaction value  $C_{f_M}$  due to the influence of the self-induced favorable pressure gradient.<sup>3</sup> Maslach and Talbot<sup>4</sup> have estimated that the magnitude of this effect is approximately

$$\frac{C_{f_{VI}}}{C_{f_M}} \approx \sqrt{\frac{P_{VI}}{P_c}} = \sqrt{1 + \left( \frac{P - P_c}{P_c} \right)_{VI}} \quad (1.2)$$

However, the present theory which neglects the pressure gradient actually predicts a slight decrease in local skin friction, as shown in Figure 31. This error, which would make the theoretical zero-injection values even higher than those shown, is probably more or less canceled by an equivalent theoretical overestimate of the pressure drag.

One sees from Figures 29 and 30 that the present theory becomes rapidly worse with increasing injection. This is thought to be due primarily to: (1) the relatively large favorable pressure gradients existing on the latter half of the model, (2) the inadequacy of the skin friction TVC correction when applied to the injection case. Baron and Scott<sup>17</sup> have considered the effect of favorable pressure gradients for a flat plate for helium and air injection. Their numerical results were for the case  $M_\infty \rightarrow 0$ , so are not directly applicable to the present

experiments. However, they do show that skin friction may be doubled or tripled by moderate favorable pressure gradients, both with and without injection. Even more interesting, their results show that for zero pressure gradient the helium skin friction vs. injection curve is below the air curve, while for a sufficiently large favorable pressure gradient the positions of the two curves reverse. (This reversal is thought to be linked to the "velocity overshoot" phenomenon, which is greater with the lower density helium boundary layer than with air.<sup>17</sup>) Now with injection Figures 17 and 18 show that a favorable pressure gradient, which increases with injection, occurs on the rear half of the model (which contains 3/4 of the area). Since the pressure gradients are of the order of those studied by Baron and Scott,<sup>17</sup> it is tempting in the present case to attribute to the neglect of pressure gradients in the theory the overly sharp theoretical drop-off of total drag and the reversal of the helium and air curves.

Besides the above, it is known also that even small injection rates alter considerably the boundary layer profiles from the no-injection case.<sup>5,6</sup> Thus it is not reasonable (as was done) to apply the zero-injection TVC correction to skin friction for the mass injection case. Finally, since mass injection increases the boundary layer thickness quite markedly, one might expect the magnitude of the TVC correction to increase with injection (rather than decrease slightly as the present results indicate). If so, this would bring the theory into closer agreement with the data, and together with the necessary pressure gradient corrections might even account for the higher total drag with helium than with air injection.

### 1.10 Conclusions

For the two flow conditions of the tests both helium and air injection produced significant reductions in the total drag of the 5° cone. The seemingly anomalous feature of the drag data was, however, that the incremental drag reduction with air injection was up to about twice that with helium. An approximate boundary layer theory was developed which reasonably agreed with the zero-injection drag results. With increasing injection rates the present theory became progressively worse, probably due to the neglect of pressure gradient effects and because an adequate transverse curvature correction was unavailable.

The experiments showed that both helium and air injection increased the boundary layer induced surface pressure increment up to five times the no-injection value. The theory presented agreed with the trend of the data with injection, but overestimated the self-induced pressure increment by a factor of about two.

The experimental fact that helium injection was less effective than air for total drag reduction suggests the possibility that injected or ablated materials of high molecular weight may be more effective than light gases for reducing the drag of slender bodies in the low Reynolds number flight regime. This does not necessarily conflict with heat protection requirements, since an injected gas of high molecular weight (with many internal degrees of freedom which could be excited) might also serve as an effective coolant.<sup>18</sup>

## 2.0 EXPERIMENTAL PROCEDURE AND DATA REDUCTION

### 2.1 Operation of the Wind Tunnel

All tests were performed in the No. 4 Low Density Wind Tunnel at the Aeronautical Sciences Laboratory at the University of California Richmond Field Station. This facility uses axi-symmetric nozzles to obtain Mach number variation, and the performance characteristics of the nozzles used in this experiment and the operation of the wind tunnel are described in References 7 and 8. Pressures are measured with mercury or butyl phthalate oil manometers having least counts equal to 0.001 inch.<sup>19,20</sup>

It had been previously established<sup>7,8</sup> that when the nozzle exit and test chamber pressures were matched, an isentropic core of approximately 2.5 inches diameter existed in both nozzles used in the test program. The pressure matching was accomplished either by adjusting the impedance of the flow system downstream of the test chamber, or by bleeding additional air into the test chamber.<sup>7,8</sup>

The existence of isentropic flow allowed the test section flow conditions to be determined from the isentropic flow tables<sup>21</sup> using readings of impact and stagnation pressure. The stagnation temperature was measured by a mercury-in-glass thermometer. The Reynolds number was calculated using the isentropic flow tables and the Bromley-Wilke<sup>22</sup> viscosity data.

Impact pressures were measured using a 0.300 inch diameter hemisphere-cylinder probe with a 0.050 inch tap at the stagnation point. It was unnecessary to employ any correction to the probe readings for

viscous effects.<sup>23</sup> Because of the fixed mounting of the models (Figures 3 and 4), it was necessary to take impact pressure readings about 3/4 inch off the center line of the flow. The readings thus obtained agreed within 2% of the values obtained from impact surveys of the flow without the model present (Figures 32 and 33). The value of impact pressure selected for use in data reduction corresponded roughly to the centerline value at the mid-point of the model.

## 2.2 Mounting of the Models

All models except the cone pressure probes were mounted in the "standard configuration" shown in Figures 3, 4, and 8. The probes were attached to the tunnel rotating probe mount (shown in Figures 3 and 4 with the impact probe attached). In all cases the model apex was located 1/2 inch downstream of the nozzle exit plane. The angle of attack was set to zero by using a plastic template (shown on the test platform in Figure 4), which could be slipped over the model. By using this template and the parallel edges of a steel scale placed between the template face and the nozzle exit plane, the model axis could be aligned within about 0.1 degree with the center line of the nozzle (as measured by a cathetometer). The gap width between model base and afterbody was set at  $0.013 \pm 0.003$  inch.

## 2.3 Pressure Distribution Measurements

The surface static pressure distribution with gas injection was determined from measurements using two porous cone models having three pressure taps per model (Figures 7 and 8). These are designated the 1,3,5 and 2,4,6 models, where tap #1 is nearest the cone apex and tap

#6 is nearest the cone base. The taps were 0.040 inch I.D. x 0.007 inch wall stainless steel tubing attached to the porous surface with epoxy resin.

The pressure lines from the three taps in each model passed through the cone base and sting shield to port locations on a Datex pressure scanner (See Figure 7). The hole in the rotating head of the scanner was drilled out to 0.052 inch diameter to obtain better time response of the pressure system. From the scanner the selected pressure signal passed through a short length of tubing to a Decker pressure transducer\* and then to a Heathkit vacuum tube voltmeter having a least count equivalent to four microns of mercury. The total time to reach steady state after a pressure change was roughly 15 seconds (agreeing very well with design estimates based on Reference 24). Readings were always taken, however, one minute after a change from the tunnel chamber pressure. Conditions were steady and repeatable enough so that it was possible to read pressures to 1/4 of the least count, or one micron of mercury.

The Decker pressure transducer was calibrated with the wind tunnel precision oil manometer,<sup>19,20</sup> which had a least count of approximately 2 microns of mercury. An additional tap on the pressure scanner

---

\*The Decker transducer is a stretched metal diaphragm gage which senses the differential pressure across the diaphragm. The reference side of the gage was connected to the wind tunnel reference pressure manifold in which the pressure was less than 0.1 micron Hg. Hence within the accuracy of these tests, the Decker gage measured the absolute pressure.

was employed so that the transducer and the oil manometer could be connected to the same closed manifold for calibration (Figure 9). By using this system one could calibrate the transducer quickly and accurately during a run without turning off the main flow or injection flow. Because of the slight non-systematic zero-point drift of the instrumentation, however, two calibration data points were taken before each series of three pressure measurements (about every six minutes). This calibration data and the pre- and post-run calibration data were sufficient to attain accuracy equivalent to that obtainable with the oil manometer, but with much faster time response.

Measurements were taken also with the "solid" model and the "cone probes" in order to obtain additional information on the zero-injection pressure distribution. The solid model had the same dimensions and pressure tap construction as the porous models and was tested in the same manner. (The 1,3,5 and 2,4,6 taps were aligned 180° apart.) The purpose of these measurements was to see if any differences in the zero-injection pressures occurred when a model of better surface quantity was used. The six cone pressure probes each had four 0.016 inch diameter pressure orifices spaced at 90° intervals around the circumference. Measurements from this series of tests were used to determine if a hole size effect existed, and also to compare results with the data of Talbot.<sup>2</sup> The Decker pressure unit was used also for these tests and gave accuracy and time response equivalent to the other tests.

## 2.4 Pressure Data Reduction

Cone surface pressure data in this report are expressed in the form  $(P - P_c)/P_c$ ; that is, the non-dimensional increment of pressure in excess of the theoretical inviscid cone pressure  $P_c$ . The inviscid pressure is a function of  $M_\infty$  and the cone half-angle  $\alpha$ , and is obtainable by interpolation in the tables of Kopal<sup>11</sup> or Sims.<sup>12</sup> This interpolation has been carried out for the present experimental conditions, and the results appear in Table B on Page 37.

The zero injection pressure distribution data for the three series of models used in the experiment were in rather poor agreement. Figure 10 shows that pressures on the porous models for zero injection measured as much as 15% to 20% above that for the corresponding position of the cone probes, with pressures for the solid cone model lying between the two sets of data. The difference between the cone probes and solid model is probably due mainly to a pressure tap hole size effect, since the magnitudes of the pressure increments agree with the data of Talbot,<sup>2</sup> who studied this effect. The additional pressure increment of the porous models over that for the solid model is probably due to the much poorer quality of the pressure taps on the porous models, and possibly to surface roughness. Although the porous model taps were locally flush with the surface, the attached steel tubing had a tendency to slightly wrinkle the thin (0.023 inch) porous wall around the tap. For these reasons it is felt that the pressure data taken with the porous pressure models do not truly represent the values of surface pressure on the force model, which had no pressure taps.

It is assumed in this report that the cone probe pressure data represent the best values for the zero-injection case. It is also assumed that the higher pressures on the porous models are due to a systematic hole size and tap geometry error which is a constant percentage of the sensed pressure. Thus, for a given pressure tap, the pressures measured on the porous models were corrected by the formula

$$P_{\text{corr}} = \left( \frac{P_{\text{actual}}}{P_{\text{no-injection}}} \right) P_{\text{standard}} \quad (2.1)$$

The "standard" pressure is based on a faired curve through the cone probe pressure data as shown in Figure 10. The zero injection pressure used in the above formula was the average value for that particular wind tunnel run. Approximate values of  $P_{\text{std}}/P_{\text{no-inj}}$  are presented in Table A below, and show the magnitudes of the corrections applied to the porous model pressure data.

Tap Number	1	2	3	4	5	6
$M_{\infty} = 3.93$	0.895	0.945	0.935	0.92	0.85	0.85
$M_{\infty} = 5.64$	0.885	0.93	0.95	0.90	0.85	0.835

Table A: Average Zero Injection Values of  $(P_{\text{std}}/P_{\text{no-inj}})$

## 2.5 Drag Force Measurements

A third porous model without pressure taps (the "force" model) was used for the total drag measurements. The one-component balance<sup>9</sup> used in the tests is shown in Figure 3, and is a standard item of experimental equipment at the Berkeley Low Density facility. The operation of the

balance was identical to that described in previous reports (e.g., Reference 4), except for the addition of a thermocouple wire and flexible rubber hose between the balance beam and surrounding casing. From the repeatability of measurements and calibrations it was determined that the modifications for gas injection had no measurable effect on the operation of the balance.

The operation of the balance may be described as follows: The model is mounted on the sting, which in turn is attached to a beam suspended on crossed flexure pivots (Figure 8). The beam torque due to model force is counteracted by a spring whose extension may be changed to "null" the position of the beam--the null position being sensed electrically by a Shaevitz linear differential transformer. The spring extension is controlled by a micrometer screw and may be determined to the nearest 0.001 inch.

The force measuring procedure used was to obtain a "wind off" or tare spring extension reading without injection, and then turn on the tunnel flow and take a "wind on" reading with or without injection. The difference between these two readings thus measured the "gross" aerodynamic force on the model. Since the momentum reaction of the injection gas differed for the "wind on" and "wind off" runs, it was not possible to measure the injection drag contribution separately.\*

---

\*The gas flow through the porous wall was in the "molecular effusion" range of densities. The magnitude and direction of the injection velocity (and hence the injection momentum reaction) are therefore influenced by conditions on the external surface of the model.<sup>25</sup>

From a knowledge of balance geometry (Figure 8) and the change in spring extension as described above, one may compute the gross drag coefficient as follows

$$C_{D_{gross}} = \frac{D_{gross}}{(\frac{1}{2} \rho_{\infty} u_{\infty}^2) A_{base}} \quad (2.2)$$

where the dynamic pressure  $(\frac{1}{2} \rho_{\infty} u_{\infty}^2)$  is obtained from the isentropic flow tables.

## 2.6 Skin Friction Drag

Since skin friction was not measured directly in the experiment, it must be obtained indirectly by calculation as follows:

$$C_{D_{frict}} = C_{D_{gross}} - (C_{D_{press}} + C_{D_{base}} + C_{D_{inj}}) \quad (2.3)$$

All drag coefficients are based on the cone base area. The remainder of the discussion of force measurements will be devoted to the determination of the quantities in parentheses in the equation above. Figures 22 and 23 and Table V give the values of each term in the above equation.

## 2.7 Pressure Drag

Pressure drag in this report is defined as the streamwise component of force due to the slant-face pressure in excess of free stream pressure. Thus the pressure drag coefficient is evaluated according to the formula

$$C_{D_P} = \frac{D_P}{(\frac{1}{2} \rho_{\infty} u_{\infty}^2) A_{base}} = \frac{2\pi(\tan \alpha)^2}{(\frac{1}{2} \rho_{\infty} u_{\infty}^2) A_{base}} \int_0^L (P - P_{\infty}) Z dZ \quad (2.4)$$

In this case, as elsewhere in this report, the surface pressure  $P$  is taken to be the "corrected" value as described in Section 2.4.

In order to evaluate  $C_{D_p}$  from the data, the above equation was put into the form

$$C_{D_p} = \frac{2\pi(\tan \alpha)^2 P_c}{\left(\frac{1}{2} \rho_\infty u_\infty^2\right) A_{base}} \int_0^L \left( \frac{P}{P_c} - \frac{P_\infty}{P_c} \right) Z dZ \quad (2.5)$$

The cross-plots of pressure data shown in Figures 17 and 18 were then used to carry out the above integral by a graphical-analytical procedure. The cone axial length  $L$  was divided into seven equal increments,  $Z$  was measured to the center of each increment, and  $P/P_c$  was taken to be the average value for the step. The accuracy of the determination of  $C_{D_p}$  and its effect on  $C_{D_f}$  are discussed in the Appendix.

## 2.8 Base Drag

A "base drag" occurred in this experiment because of the particular method of mounting the models in the wind tunnel and has no significance beyond that of an experimental correction. Because the pressure existing inside the hollow afterbody was different from  $P_\infty$ , a net force occurred on the model. The full base area was assumed to be effective, so that the base drag coefficient is defined as

$$C_{D_b} = - \frac{(P_{base} - P_\infty) A_{base}}{\left(\frac{1}{2} \rho_\infty u_\infty^2\right) A_{base}} \quad (2.6)$$

The negative sign is inserted because pressure on the base actually produces a thrust on the model. Base pressure data taken during the

force runs are shown in Figure 20, and the geometry of the afterbody and location of the pressure tap are shown in Figures 8 and 9.

## 2.9 Injection Drag

The passage of injected gas from the model walls into the boundary layer produces a drag force increment which is small, but not negligible. If we assume the validity of the no-slip boundary condition,\* then the injection velocity must be normal to the cone surface. Let  $\dot{m} = \rho_w v_w$  be the local mass flux. Then the injection drag component may be computed from the flux of momentum across the porous surface as follows:

$$D_{inj} = \int_{A_{slant}} \frac{\dot{m}^2}{\rho_w} \sin \alpha \, dA \quad (2.7)$$

---

\*According to the simple theory,<sup>26</sup> the slip velocity is  $u_w \approx \lambda (\partial u / \partial y)_w$ . A representative maximum value of the air mean free path at the model surface for the test conditions is  $\lambda \approx 0.0007$  ft (based on Maxwell's definition<sup>25</sup>). Zero injection boundary layer theory<sup>27</sup> predicts that  $(\partial u / \partial y)_w \approx (1.3 \times 10^5) \sqrt{L/Z}$  per second at  $M_\infty = 5.64$ , so that at  $Z/L = 0.5$ , we might have  $u_w \approx 65$  ft/sec. At low injection rates, therefore, slip might alter the injection gas entry angle quite markedly. With increasing injection the velocity gradient is progressively decreased and approaches zero<sup>5,6</sup> at roughly one-half of the maximum injection rates used in the experiment. Further, the injection velocity becomes significantly greater than 65 ft/sec at high injection rates. Thus it can be reasonably argued that where  $C_{D_{inj}}$  is relatively important, the injection gas enters the boundary layer approximately normal to the wall.

Since the magnitude of the injection drag turns out to be at most 10% of the total drag, a simple but fairly crude calculation is adequate. Thus we assume that  $\dot{m} \approx \dot{M}/A_{\text{slant}}$  (uniform injection) and take  $\rho_w$  to be roughly constant over the whole cone surface. Employing the perfect gas law, then, we carry out the above integral and write

$$C_{D_{\text{inj}}} = \frac{D_{\text{inj}}}{\left(\frac{1}{2} \rho_{\infty} u_{\infty}^2\right) A_{\text{base}}} = \left[ \frac{(\cos \alpha)^4}{\pi^2 L^4 (\sin \alpha)^2 \left(\frac{1}{2} \rho_{\infty} u_{\infty}^2\right)} \right] \frac{\dot{M}^2 R_w T_w}{P_w} \quad (2.8)$$

Here  $P_w$ ,  $T_w$ , and  $R_w$  are suitable average values for the surface pressure, temperature, and specific gas constant. One should notice that  $C_{D_{\text{inj}}}$  is roughly proportional to  $\dot{M}^2$  and hence becomes relatively important only at the higher injection rates.

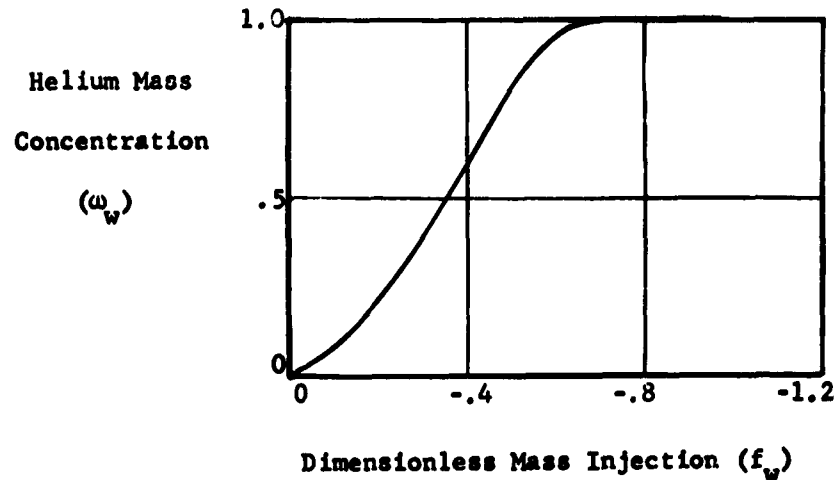
In the present experiment data are available to determine  $P_w$  and  $T_w$ , while  $R_w$  is a known constant for air. However  $R_w$  is a function of mixture concentration and must be estimated for the helium injection case. It is shown below, however, that the surface concentration of helium becomes very nearly unity at the higher experimental injection rates where  $C_{D_{\text{inj}}}$  is expected to exert influence on the force data. In this case  $R_w$  approaches the value of the gas constant for pure helium.

The estimate of  $R_w$  for the helium case proceeds as follows. The gas constant for air-helium mixtures may be written

$$R = R_{\text{air}} [1 - (M_{\text{air}}/M_{\text{He}} - 1) \omega] = R_{\text{air}} [1 - 6.25 \omega] \quad (2.9)$$

where  $\omega$  is the mass fraction of helium. The surface concentration  $\omega_w$

may be estimated from the air-helium similar boundary layer analysis of Baron,<sup>5</sup> who presents a graph of the theoretical  $\omega_w$  vs. dimensionless mass injection rate (Sketch 1 below). The quantity  $f_w$  is defined in Equation (3.7). We use the Mangler<sup>27</sup> transformation and assume here that



Sketch 1: Helium Concentration at the Wall (after Baron<sup>5</sup>)

the outer edge boundary conditions for Baron's analysis correspond to the inviscid flow theoretical solution.<sup>11,12</sup> If the total injection rate  $\dot{M}$  is equated to the corresponding value for Baron's  $x^{-1/2}$  injection law, we can integrate Equation (3.7) over the cone surface to obtain for the helium injection case\*

$$-f_w = \left[ \frac{\sqrt{3}}{2\pi L(\tan \alpha)} \sqrt{\frac{\cos \alpha}{\rho_\delta \mu_\delta u_\delta CL}} \right] \dot{M} = [B] \dot{M} \quad (2.10)$$

---

\*If viscous interaction were considered, the coefficient  $B$  and wall concentration  $\omega_w$  might be modified as much as 10% for  $f_w < 0.5$ . Since  $C_{D_{inj}}$  is practically zero for this rate of injection, this simpler calculation suffices.

The values of  $B$  derived from the analysis described above are presented below:

$$M_{\infty} = 3.93: \quad B = 10.35 \text{ hr/lb}$$

$$M_{\infty} = 5.64: \quad B = 9.28 \text{ hr/lb}$$

The values of  $\dot{M}$  where  $\omega_w$  becomes approximately equal to unity correspond roughly to one-half of the maximum experimental injection rates and are given below:

$$M_{\infty} = 3.93: \quad \dot{M} = 0.060 \text{ lb/hr} \quad (\text{for } f_w = -0.6)$$

$$M_{\infty} = 5.64: \quad \dot{M} = 0.067 \text{ lb/hr} \quad (\text{for } f_w = -0.6)$$

It is probably true, therefore, that the higher injection rates correspond to the situation where the oncoming stream boundary layer has been "blown off" the wall and replaced by a boundary layer composed only of the injected gas.<sup>5</sup>

The computation of  $C_{D_{inj}}$  according to Equation (2.8) employed the above relations for  $R_w$  for the helium case, with  $R_w$  being equal to  $R_{air}$  for air injection.  $T_w$ , the wall temperature, was taken to be constant at 0.96 times stagnation temperature, as the model temperature data shown in Figure 34 are not conclusive enough to warrant further refinement. The average surface pressure  $P_w$  was determined in the course of the integration of the pressure distribution data of Figures 17 and 18.

## 2.10 Injection Pressure vs. Flow Rate

In order to measure the model internal pressure vs. injection flow rate, a special pressure line was installed which was nested inside the injection line and projected about 1/2 inch inside the porous cone. The model was placed inside the wind tunnel test chamber several feet to one side of the main flow stream. The test chamber pressure (i.e., model external pressure) could then be held constant by bleed air adjustments while internal pressure vs. flow data were taken (Figure 35). The external pressures used in these tests correspond roughly to the maximum and minimum values occurring in the pressure distribution tests.

Scott<sup>28</sup> has derived the following equation for the mass flux of low density gas through a (flat) porous wall

$$\dot{m} = \rho_w v_w = \frac{P_i^2 L_1^2}{32\mu R T t} \left( 1 - \frac{P_e^2}{P_i^2} \right) \left[ 1 + \left( \frac{2-f}{f} \right) \frac{4\sqrt{2} \lambda_a}{L_1} \right] \quad (2.11)$$

where for simplicity we may take  $f = 1$  (diffuse reflection) and use for the average mean free path<sup>26</sup>

$$\lambda_a = \sqrt{\frac{\pi R T}{2}} \frac{2\mu}{(P_i + P_e)} \quad (2.12)$$

Here  $P_i$  and  $P_e$  are the internal and external pressures, and  $L_1$  is the characteristic pore diameter. For a given model at constant temperature the above equation indicates that flow rate depends very weakly on external pressure when  $P_i \gtrsim 5P_e$ . From the flow vs. pressure data shown in Figure 35, it may be seen that this condition was satisfied for most of the injection flow rate range of the experiment. For near-zero flow

rates the data still do not indicate much (if any) alteration in flow rate with external pressure change. This is probably because the external pressure range of 140 to 200 microns surface pressure was not a wide enough variation to produce much of an effect. From this we may conclude that the injection mass flux distribution in the experiment was essentially unaltered by changes in external surface pressure.

### 2.11 Local Mass Flux Distribution

An attempt was made to determine the variation of local injection mass flux with axial position. The apparatus used is shown in Figure 36, and the procedure may be described briefly as follows: The differential change in total mass flux  $d\dot{M}$  is related to the local (circumferentially averaged) mass flux  $\dot{m}$  by

$$d\dot{M} = \dot{m} (2\pi Z \tan \alpha / \cos \alpha) dZ, \quad \dot{m} = \rho_w v_w \quad (2.13)$$

We let  $\dot{M}_{\max}$  denote the total flow rate through the model at atmospheric external pressure and with a given pressure drop across the wall. Then

$$\frac{\dot{m}}{(\dot{M}_{\max}/A_{\text{slant}})} = \frac{L^2}{2Z} \left( \frac{d\dot{M}/\dot{M}_{\max}}{dZ} \right) \quad (\text{equals unity for uniform injection}) \quad (2.14)$$

Various axial lengths  $Z$  of the model were masked off with pieces of rubber tubing (Figure 36). A curve of  $\dot{M}/\dot{M}_{\max}$  vs.  $Z$  for a constant pressure drop across the model was then constructed (Figure 37). By graphically differentiating the resulting data the derivative in Equation (2.14), and hence the local flux distribution, was calculated. The procedure is admittedly crude, but serves to indicate the departure from uniform injection, as shown in Figure 38.

## 2.12 Injection Flow Metering

The injection flow system is shown in detail in Figure 7. The more accurate metering was obtained by calibrating 6 inch glass capillary tubes of four different diameters by measuring the gas flow rate as a function of pressure drop.\* It was found that the flow rate vs. pressure drop curve for both helium and air followed the Poiseuille formula<sup>27</sup> fairly well except at the highest flow rates used.

Corrections to the metering calibration for laboratory pressure and temperature variations were applied as follows: Flow in the capillary tube was assumed to follow the Poiseuille formula, and viscosity was assumed proportional to the 0.75 power of temperature for both helium and air. The density correction was obtained from the perfect gas law, so that

$$\dot{M}_{\text{true}} = \dot{M}_{\text{std}} \left( \frac{530}{T} \right)^{1.75} \left( \frac{P}{29.92} \right) \quad (2.15)$$

where "standard" conditions were taken as  $P = 29.92$  in Hg,  $T = 530$  °R at the upstream end of the capillary tube. It should be noted that the actual test conditions never differed by more than about 2% from the conditions of the meter calibration, so that the actual magnitude of the correction was less than a few percent.

For a back-up system Fischer-Porter "Flowrator" meters were also used to meter the injection flow. From the Fischer-Porter data accompanying the flowmeters the following correction formula for temperature and pressure variations at the inlet to the meter was obtained:

---

\* The calibration was carried out in the Standards Laboratory in Hesse Hall on the University of California campus.

$$\dot{M}_{\text{true}} = M_{\text{std}} \left( \frac{530}{T} \frac{P}{29.92} \right)^{1/2} \quad (2.16)$$

It should be noted, however, that Equation (2.16) is probably more accurate for large "Flowrator" meters where viscous effects are less important. Since the injection flow rates were quite low in the experiment and viscous effects probably were important, the above correction formula must be viewed with some suspicion, as the assumptions used for its derivation are not known. Because of this uncertainty and because of the generally greater level of accuracy attainable with the capillary metering system, all of the final data except for helium above 0.09 lb/hr are based on the capillary metering system.

### 3.0 BOUNDARY LAYER ANALYSIS

#### 3.1 Objective and Assumptions

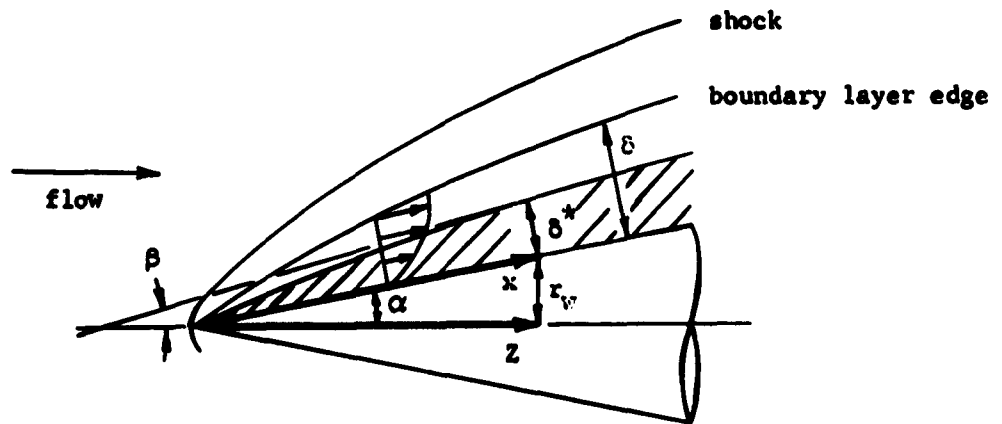
A truly realistic description of the boundary layer flow for the experiment is beyond the scope of the present report. Such an analysis, including gas injection and the complicating low Reynolds number effects thought to be important, would involve extensive analytical and numerical effort. As yet no theoretical work of this type of sufficient generality has been carried out. The present analysis is an "engineering approach" which attempts to explain the major trends in the data, and yet is simple enough to be done by hand calculations with a reasonable expenditure of effort. The analysis makes liberal use of existing boundary layer solutions for a flat plate with surface mass flux varying as  $x^{-1/2}$ , as required by "similarity" considerations.<sup>5,6</sup>

It is clear that the problem can only be made tractable by the omission from the analysis of most of the complicating boundary layer effects. Talbot, Koga, and Sherman<sup>1</sup> have shown that the induced surface pressure distribution may be estimated with reasonable accuracy for the no-injection case by considering only the viscous interaction coupled to a locally similar boundary layer. Their analysis assumed that viscosity was proportional to temperature and that compressibility effects could be accounted for by the Chapman-Rubesin factor. These assumptions are retained in the present analysis, with viscosity being assumed proportional to temperature times a function of mass concentrations for the air-helium mixture.<sup>5</sup> In the latter case Baron<sup>5</sup> has shown that the problem may be formulated so that the Chapman-Rubesin factor

is chosen for air only, in the same manner as for the single component boundary layer. In the present analysis we shall attempt to extend the method of Talbot, Koga, and Sherman to include the effects of surface mass transfer on the induced pressure, and also on the total skin friction drag.

### 3.2 Inviscid Flow

In order to solve the boundary layer problem one must know the outer edge boundary conditions from the inviscid flow solution. Since these conditions depend on the boundary layer growth, the inviscid and boundary layer flows must be considered together. Following Talbot,<sup>1,2</sup> the displacement thickness  $\delta^*$  is added to the cone at each station  $x$  as shown in Sketch 2 below. Boundary layer edge quantities  $\rho_\delta$ ,  $u_\delta$ , etc., are then assumed to be given by the tangent cone theory<sup>3</sup> applied to the effective body formed by the addition of  $\delta^*$  to the cone. Using



Sketch 2: Assumed Physical Model  
of the Flow

this procedure the specification of the boundary layer edge conditions can be made once we know  $M_\infty$  and the local tangent cone angle  $\beta$  given by

$$\beta = \alpha + \arctan \left( \frac{d\delta^*}{dx} \right) \quad (3.1)$$

The solution for  $\delta^*$  is considered in the next section.

### 3.3 Displacement Thickness

We neglect the effect of transverse curvature on the displacement thickness<sup>14,15</sup> and employ the results of Low<sup>6</sup> for air injection and Baron<sup>5</sup> for helium injection. In both cases the expression for the displacement thickness may be written

$$\delta^* = \frac{2}{\sqrt{3}} \sqrt{\frac{\mu_0 C x}{\rho_0 u_0}} \left[ \zeta + \frac{\gamma-1}{2} M_0^2 I_r + \left( \frac{T_w}{T_0} - \frac{T_{aw}}{T_0} \right) I_s \right] \quad (3.2)$$

where  $\sqrt{3}$  is the Mangler factor, and  $\zeta$ ,  $I_r$ , and  $I_s$  are constants for a given mass injection rate (assuming a locally similar boundary layer). The adiabatic wall temperature in the above is specified in terms of the recovery factor  $\sigma$  as follows

$$\frac{T_{aw}}{T_0} = 1 + \sigma \left( \frac{\gamma-1}{2} \right) M_0^2 \quad (3.3)$$

and the Chapman-Rubesin factor  $C$  for both injection gases is determined by matching the air viscosity at the wall

$$C = \frac{\mu_w}{\mu_0} \frac{T_0}{T_w} \quad \mu = \mu_{air} \quad (3.4)$$

An approximate value of  $d\delta^*/dx$  is obtained by neglecting the streamwise derivatives of boundary layer edge quantities as follows:

$$\sqrt{x} \frac{d\delta^*}{dx} = \frac{1}{\sqrt{3}} \sqrt{\frac{\mu_{\delta} C}{\rho_{\delta} u_{\delta}}} \left[ \zeta + \frac{\gamma-1}{2} M_{\delta}^2 I_r + \left( \frac{T_w}{T_{\delta}} - \frac{T_{aw}}{T_{\delta}} \right) I_s \right] + \left[ \frac{d}{dx} ( )_{\delta} \right] \sim 0 \quad (3.5)$$

This approximation is in the spirit of the local similarity assumption of the boundary layer analysis.\* When  $M_{\infty}$  and the tangent cone angle  $\beta$  are specified, we may find the edge Mach number  $M_{\delta}$  and pressure  $P_{\delta}$  by interpolation in the conical flow tables of Sims.<sup>12</sup> This interpolation has been carried out for the  $M_{\infty}$  values of the present experiment, and the results are presented in Table B below. The remaining edge quantities are determined from the formulas

$$\frac{T_s}{T_{\infty}} = \left( 1 + \frac{\gamma-1}{2} M_{\infty}^2 \right) \quad \frac{T_s}{T_{\delta}} = \left( 1 + \frac{\gamma-1}{2} M_{\delta}^2 \right) \quad (3.6)$$

$$\frac{\rho_{\delta}}{\rho_{\infty}} = \frac{P_{\delta}}{P_{\infty}} \frac{T_{\infty}}{T_{\delta}} \quad u_{\delta} = \sqrt{\gamma R_{air} T_{\delta}} M_{\delta}$$

$$\mu = \mu_{\delta}(T_{\delta}) \text{ Bromley-Wilke viscosity data}^{22}$$

The quantities  $\zeta$ ,  $I_r$ , and  $I_s$  in Equation (3.5) depend on the dimensionless mass injection parameter  $f_w$ , and are given in Table C below.

---

\*The neglected term in Equation (3.5) turned out to be about 2% to 5% of the retained term for the present range of flow conditions.

$$M_{\infty} = 3.93$$

$\beta$ - degr	0	2.5	5.0	7.5	10.0	12.5	15.0	17.5	20.0
$P_8/P_{\infty}$	1.000	1.088	1.272	1.530	1.862	2.26	2.74	3.29	3.90
$M_8$	3.93	3.86	3.75	3.615	3.47	3.32	3.165	3.005	2.845

$$M_{\infty} = 5.64$$

$\beta$ - degr	0	2.5	5.0	7.5	10.0	12.5	15.0	17.5	20.0
$P_8/P_{\infty}$	1.000	1.158	1.494	1.980	2.63	3.43	4.40	5.49	6.76
$M_8$	5.64	5.515	5.285	5.03	4.755	4.475	4.19	3.91	3.64

Table B: Values for the Tangent Cone Theory (from Sims<sup>12</sup>)

$f_w$	$\sigma$	$\zeta$	$I_r$	$I_s$	$f_w''$
0	0.848	0.860	1.109	0.969	1.328
-0.50	0.799	1.230	1.411	1.317	0.658
-0.75	0.768	1.564	1.660	1.623	0.374
-1.00	0.733	2.195	2.103	2.202	0.142

Air Injection (after Low<sup>8</sup>)

$f_w$	$\sigma$	$\zeta$	$I_r$	$I_s$	$K_w f_w''$
0	0.848	0.860	1.109	0.969	1.328
-0.20	0.745	1.933	1.704	1.961	0.767
-0.308	0.674	2.671	2.027	2.650	0.503
-0.40	0.616	3.510	2.345	3.393	0.307

Helium Injection (after Baron<sup>5</sup>)

Table C: Values Appearing in the Expressions for Displacement Thickness and Skin Friction

### 3.4 Injection Mass Flow Rate

According to the analyses of Baron<sup>5</sup> and Low,<sup>6</sup> the local mass flux is given by

$$\dot{m} = \rho_w v_w = \frac{\sqrt{3}}{2} \sqrt{\frac{\rho_\delta u_\delta \mu_\delta C}{x}} (-f_w) \quad (3.7)$$

where again  $\sqrt{3}$  is the Mangler factor. The total mass flow rate  $\dot{M}$  is determined by integration

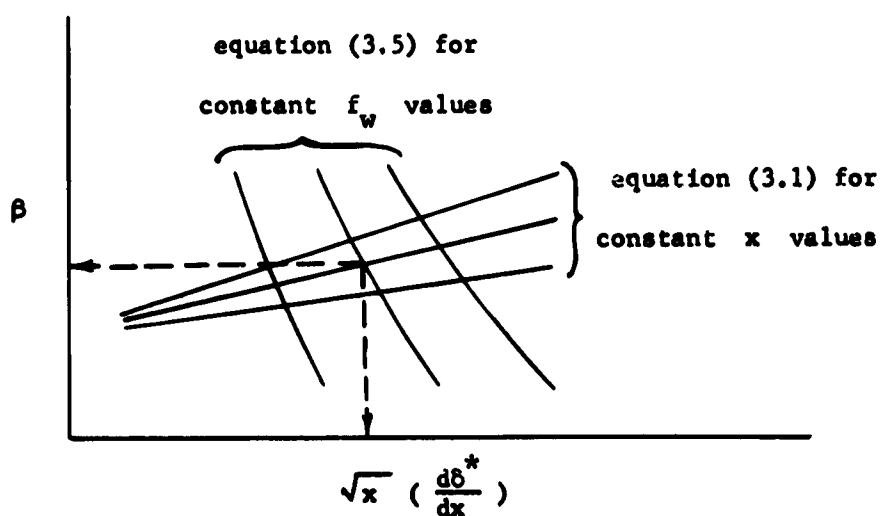
$$\dot{M} = \int_{A_{\text{slant}}} \rho_w v_w dA = \pi \sqrt{3} (\sin \alpha) \int_0^s \sqrt{\rho_\delta u_\delta \mu_\delta C x} (-f_w) dx \quad (3.8)$$

Notice that the quantities  $I_r$ ,  $I_s$ , and  $\zeta$  have been computed for only a few values of  $f_w$ , and that the edge quantities  $\rho_\delta u_\delta \mu_\delta C$  in Equation (3.7) are initially unknown. For this reason it is impractical for the present purposes to specify the local flux  $\rho_w v_w$  in advance. Instead we shall use  $f_w$  (constant) as the independent mass flux parameter and carry through the analysis of the boundary layer--inviscid flow matching. When this has been accomplished, then the total mass injection rate  $\dot{M}$  corresponding to  $f_w$  can be determined from Equation (3.8), since  $\rho_w v_w$  will then be known. Because of the variation of the edge quantities  $\rho_\delta$ ,  $u_\delta$ , etc. with  $x$  caused by viscous interaction, the injection law will no longer be the  $x^{-1/2}$  variation given by (3.7) for constant edge quantities. In fact, we lose control of the injection law altogether by this procedure and must accept whatever distribution comes out of the assumption that  $f_w$  is constant. Figure 27 shows that the injection distribution does not depart more

than about  $\pm 10\%$  from the  $x^{-1/2}$  law implicit in the theory, and this is an acceptable variation for the present purposes.

### 3.5 Solution Method

The matching of the boundary layer and inviscid solutions at each station  $x$  is conveniently done by graphical analysis. For given values of  $M_\infty$ ,  $f_w$ , and  $x$ , we plot the curves of Equations (3.1) and (3.5) as shown in Sketch 3 below. The intersections of these curves yield



Sketch 3: Graphical Solution for the Tangent Cone Angle

the proper displacement thickness slope angle  $\beta$  for the value of  $x$  under consideration. With  $\beta$  known the boundary layer edge quantities can be calculated from the tangent cone tables and Equations (3.6). By assuming a locally similar boundary layer, then, the results of Baron<sup>5</sup> and Low<sup>6</sup> become available for the computation of skin friction and total mass injection rate. Since the pressure is approximately constant

across the boundary layer, the surface pressure distribution is the same as  $P_0$ .

The remaining quantities of interest are the skin friction drag and pressure drag coefficients. From Baron and Low the skin friction coefficient is given by

$$C_f = \frac{\mu_w \left( \frac{\partial u}{\partial y} \right)_w}{\frac{1}{2} \rho_\infty u_\infty^2} = \frac{\sqrt{3}}{2} \sqrt{\frac{\mu_0 C}{\rho_\infty u_\infty^2 x}} (K_w f_w'') \quad (3.9)$$

$$K_w = 1.0 \text{ for air injection}$$

Values of  $K_w f_w''$  are given in Table C. The skin friction drag is then obtained by integration

$$C_{Df} = \frac{D_f}{\left( \frac{1}{2} \rho_\infty u_\infty^2 \right) A_{\text{base}}} = \frac{\sqrt{3} (K_w f_w'')}{s^2 (\tan \alpha) \left( \frac{1}{2} \rho_\infty u_\infty^2 \right)} \int_0^s \sqrt{\frac{\mu_0 C x}{\rho_\infty u_\infty^2}} \left( \frac{1}{2} \rho_\infty u_\infty^2 \right) dx \quad (3.10)$$

The pressure drag coefficient is obtained from an integral of the surface pressure distribution as follows

$$C_{Dp} = \frac{D_p}{\left( \frac{1}{2} \rho_\infty u_\infty^2 \right) A_{\text{base}}} = \frac{4}{\gamma M_\infty^2 s^2} \int_0^s \left( \frac{P_0}{P_\infty} - 1 \right) x dx \quad (3.11)$$

The results of the above analysis are shown by curves labeled VI (for viscous interaction solution) in Figures 24, 25, 29, and 30. In the actual analysis for convenience  $x$  was replaced by the axial distance  $Z = x \cos \alpha$ . Simpson's rule was used for the integrations with seven values of  $Z$  between 0.5 and 3.5 inches--the step from 0 to 0.5 employing a linear extrapolation from the 0.5 and 1.0 inch values.

### 3.6 Transverse Curvature Effect

Transverse curvature (TVC) effects result from the inability of the usual two-dimensional boundary layer solutions with Mangler transformation to account for the effects of the circumferential spreading of the thick boundary layer flow on a slender body of revolution. When the TVC terms are retained in the boundary layer equations, a correct analysis is greatly complicated by the necessary consideration of partial differential equations, rather than the ordinary differential equations resulting from a similar boundary layer.

The only available results of analyses including the transverse curvature effect which are applicable to the present experiment are those of Probstein and Elliott<sup>14</sup> and Yasuhara.<sup>15,16</sup> In these papers sufficient assumptions as to the character of the flow were made so that the authors could deal with ordinary differential equations. Although the resulting physical flows are not of direct interest, the mathematical results are made useful for engineering purposes by the assumption of local similarity.

No analysis of the boundary layer equations with both gas injection and transverse curvature terms has as yet been carried out. For the zero-injection case, however, Yasuhara<sup>15</sup> has solved approximately the TVC boundary layer equations for the case of zero pressure gradient, Prandtl number equal to 0.7, and  $T_w/T_s = 1.0$ . This is sufficiently close to the present experimental conditions to warrant a quantitative estimate of the TVC effect based on his calculations.

After the final TVC correction formulas based on Yasuhara's results are derived, it will be assumed that they may be applied also for the injection case. This is done in the present report only for illustrative

purposes, since there is no reason to expect that the zero-injection TVC corrections will be a good approximation for the injection case.

Now the boundary layer induced pressure depends on the displacement thickness slope  $d\delta^*/dx$ . We will use Yasuhara's results to estimate the magnitude of the change in  $d\delta^*/dx$  due to TVC, and from this the change in pressure. To fix ideas, consider the defining expression for the boundary layer displacement thickness  $\delta^*$ :

$$\int_0^{\delta^*} \rho_\delta u_\delta \, 2\pi r \, dy = \int_0^\delta (\rho_\delta u_\delta - \rho u) \, 2\pi r \, dy \quad (3.12)$$

Here  $r = r_w + y(\cos \alpha)$  is now variable in the thick boundary layer. One sees that for  $r \neq r_w$  the expression for  $\delta^*$  is fundamentally different from the thin boundary layer case. ( $r = r_w$  is assumed in Mangler's transformation.<sup>27)</sup> Yasuhara<sup>15</sup> gives the following results for the solution for  $\delta^*$  in hypersonic flow:

$$\text{with TVC:} \quad \left( \frac{\delta^*}{r_w} \right)_{\text{TVC}} \approx \sqrt{1 + Am_e} - 1 \quad (3.13)$$

$$\text{without TVC:} \quad \left( \frac{\delta^*}{r_w} \right)_M = \frac{1}{2} Am_{eM} \quad (3.14)$$

where for a slender cone in hypersonic flow

$$A = \left( 1 + \frac{\gamma-1}{2} M_\delta^2 \right) \sqrt{\frac{8 C \mu_\delta}{3 \rho_\delta u_\delta x}} \frac{1}{\alpha} \approx (\gamma-1) \sqrt{\frac{2}{3}} \frac{\bar{\chi}_\delta}{M_\delta \alpha} \quad (3.15)$$

We may approximate with sufficient accuracy for the present purpose the graphical results for  $m_e$  and  $m_{eM}$  given by Yasuhara by

$$m_e \approx 1.95 + (0.36)A \quad (3.16)$$

$$m_{eH} = 1.95$$

and replace  $M_0$  by  $M_c$  and  $\bar{\chi}_0$  by  $\bar{\chi}_c$  defined by

$$\bar{\chi}_c = M_c^3 \sqrt{\frac{C \mu_c}{\rho_c u_c x}} \quad (3.17)$$

Let us define the change in the displacement thickness slope as follows:

$$\Delta \left( \frac{d\delta^*}{dx} \right)_{TVC} = \left[ \left( \frac{d\delta^*}{dx} \right)_{TVC} - \left( \frac{d\delta^*}{dx} \right)_{VI} \right] \quad (3.18)$$

The last term is the value of  $d\delta^*/dx$  computed from the previously described viscous interaction (VI) solution. With  $r_w \approx \alpha x$  it may be shown from the preceding formulas that

$$\Delta \left( \frac{d\delta^*}{dx} \right)_{TVC} = \alpha \left[ \frac{-(1.95 + 0.72A)A}{4\sqrt{1 + A(1.95 + 0.36A)}} + \sqrt{1 + A(1.95 + 0.36A)} - 1 - \frac{1.95A}{4} \right] \quad (3.19)$$

The induced pressure correction may then be estimated by perturbing the VI solution as follows:

$$\Delta P_{TVC} \approx \frac{\partial P}{\partial \left( \frac{d\delta^*}{dx} \right)} \Delta \left( \frac{d\delta^*}{dx} \right)_{TVC} \approx \left( \frac{\partial P}{\partial \beta} \right) \frac{d\beta}{d \left( \frac{d\delta^*}{dx} \right)} \Delta \left( \frac{d\delta^*}{dx} \right)_{TVC} \quad (3.20)$$

$\uparrow$   
 tangent  
 cone  
 table

$\uparrow$   
 from  
 Eq. (3.1)

This may be put into the form

$$\left[ \frac{P-P_c}{P_c} \right]_{TVC} = \left[ \frac{P-P_c}{P_c} \right]_{VI} + \underbrace{\left( \frac{P_\infty}{P_c} \right) \left[ \frac{\partial (P/P_\infty)}{\partial \beta} \right]_{\beta=\beta_{VI}} \frac{1}{\left[ 1 + \left( \frac{d\delta^*}{dx} \right)_{VI}^2 \right]}}_{\text{TVC Correction}} \Delta \left( \frac{d\delta^*}{dx} \right)_{TVC} \quad (3.21)$$

For the TVC correction to the skin friction Yasuhara<sup>15</sup> finds that approximately

$$C_{f_{TVC}} \sim \left\{ 1 + 0.377A - 0.0089A^2 \right\} \quad \begin{cases} \text{zero pressure grad.} \\ \text{Prandtl No.} = 0.7 \\ T_w/T_s = 1.0 \end{cases} \quad (3.22)$$

The TVC effect is contained in the terms multiplied by "A" in the above, so that

$$\frac{C_{f_{TVC}} - C_{f_M}}{C_{f_M}} \approx \left\{ 0.377A - 0.0089A^2 \right\} \quad (3.23)$$

where the no-interaction skin friction coefficient is

$$C_{f_M} = \frac{\sqrt{3}}{2} \sqrt{\frac{\mu_c C}{\rho_c u_c x}} \quad (K_w f_w'') \quad (3.24)$$

For the TVC correction to total drag, then, we need only compute the change in pressure and skin friction drag coefficients. These are given by

$$\left( \Delta C_{D_P} \right)_{TVC} = \left( \frac{P_c}{P_\infty} \right) \frac{4}{\gamma M_\infty^2 L^2} \int_0^L \Delta \left[ \frac{P-P_c}{P_c} \right]_{TVC} dz \quad (3.25)$$

$$\begin{aligned}
 (\Delta C_{D_f})_{\text{TVC}} &= \frac{2}{L^2(\tan \alpha)} \left( \frac{P_c M_c^2}{P_{\infty} M_{\infty}^2} \right) \int_0^L C_{f_M} \cdot \\
 &\quad \cdot \left\{ 0.377A - 0.0089A^2 \right\} z dz \quad (3.26)
 \end{aligned}$$

where the term under the integral in (3.25) is the TVC correction term of Equation (3.21).

REFERENCES

1. L.Talbot  
T. Koga  
P.M.Sherman "Hypersonic Viscous Flow over Slender Cones," Univ. of Calif. Eng. Proj. Rept. HE-150-147, June 1957  
(Also J.Aero.Sci. 26, 11, 723, 1959).
2. L.Talbot "Viscosity Corrections to Cone Probes in Rarefied Supersonic Flow at a Nominal Mach Number of 4," Univ. of Calif. Eng. Proj. Rept. HE-150-113, June 1953  
(Also NACA TN 3219).
3. W. D. Hayes  
R.F.Probstein Hypersonic Flow Theory, Academic Press, New York, 1959.
4. G.J.Maslach  
L.Talbot "Low Density Aerodynamic Characteristics of a Cone at Angle of Attack," Univ. of Calif. Eng. Proj. Rept. HE-150-172, October 1959.
5. J.R.Baron "The Binary Boundary Layer Associated with Mass Transfer Cooling at High Speeds," M.I.T. Naval Supersonic Lab. Tech. Rept. 160, May 1956.
6. G.M.Low "The Compressible Boundary Layer with Fluid Injection," NACA TN 3404, March 1955.
7. L.L.Lynes "Design, Fabrication, and Evaluation of Axisymmetric Nozzles," Univ. of Calif. Eng. Proj. Rept. HE-150-174, September 1959.
8. G.J.Maslach  
F.S.Sherman "Design and Testing of an Axisymmetric Hypersonic Nozzle for a Low Density Wind Tunnel," Univ. of Calif. Eng. Proj. Rept. HE-150-134, February 1956 (Also WADC TR-56-341).
9. G.J.Maslach  
R.N.Latz "Force Measurements in Low Density Hypersonic Air Flows," Advances in Vacuum Science and Technology, Vol. II, Pergamon Press, New York, pp 809-812, 1960.

10. B.L.Swenson "Exploratory Study of the Reduction in Friction Drag Due to Streamwise Injection of Helium," NASA Tech. Note D-342, January 1961.
11. Z.Kopal "Tables of Supersonic Flow Around Cones," M.I.T., Cambridge, Mass., 1947.
12. J.L.Sims "Supersonic Flow Around Right Circular Cones, Tables for Zero Angle of Attack," ABMA Rep. DA-TR-11-60, March 1960 (Also ASTIA 234736).
13. J.F.Gross  
J.P.Hartnett  
D.J.Masson  
C.Gazley, Jr. "A Review of Binary Boundary Layer Characteristics," RAND Report RM-2516, June 1959 (Also ASTIA 240432).
14. R.F.Probstein  
R.F.Elliott "The Transverse Curvature Effect in Compressible Axially Symmetric Laminar Boundary-Layer Flow," J.Aero.Sci. 23, 3, March 1956.
15. M.Yasuhara "Axisymmetric Viscous Flow Past Very Slender Bodies of Revolution," J.Aero.Sci. 29, 6, June 1962.
16. M.Yasuhara "Simultaneous Effects of Pressure Gradient and Transverse Curvature on the Boundary Layer Along Slender Bodies of Revolution," Aero.Res.Inst., Univ. of Tokyo Rept. 335, August 1958.
17. J.R.Baron  
P.B.Scott "The Laminar Diffusion Boundary Layer with External Flow Field Pressure Gradients," M.I.T. Naval Supersonic Lab. Tech. Rept. 419, December 1959.
18. I.Korobkin "The Effects of the Molecular Properties of an Injected Gas on Compressible Air Laminar Boundary Layer Skin Friction and Heat Transfer," NAVWEPS Rept. 7410, U.S. Naval Ordnance Lab., White Oak, Maryland, March 1961.

19. G.J.Maslach "A Precision Differential Manometer," Rev.Sci.Instr.  
23, 7, 367, 1952.
20. G.J.Maslach "Vacuum Facilities for the Study of Supersonic Flow,"  
Chem.Eng.Progress, 48, 12, December 1952.
21. H.N.Rise "Compressible Flow Tables for Air in Increments of  
0.001 in Mach Number," Jet Propulsion Lab. Publication  
27, Calif. Inst. of Tech., August 1954.
22. L.A.Bromley "Viscosity Behavior of Gases," Industrial and Engineer-  
C.R.Wilke ing Chemistry, 43, 7, 1641, 1951.
23. F.S.Sherman "New Experiments on Impact Pressure Interpretation in  
Supersonic and Subsonic Rarefied Airstreams," Univ. of  
Calif. Eng.Proj.Rept. HE 150-78, February 1951 (Also  
Trans. of the ASME, 74, 7, October 1952).
24. J.M.Kendall "Optimized Design of Systems for Measuring Low Pressures  
in Supersonic Wind Tunnels," AGARD Rept. 174, March 1958.
25. M.N.Saha "A Treatise on Heat, 4th Ed., The Indian Press, 1958.  
B.N.Srivastava
26. S.A.Schaaf "Flow of Rarefied Gases," Fundamentals of Gas Dynamics,  
P.L.Chambre' H.W.Emmons, ed., Princeton Univ. Press, 1958.
27. S.I.Pai Viscous Flow Theory, I - Laminar Flow, D. Van Nostrand  
Company, New York, 1956.
28. C.J.Scott "Experimental Investigation of Laminar Heat Transfer  
and Transition with Foreign Gas Injection--A 16° Porous  
Cone at  $M \sim 5$ ," UMRAL Res.Rept. 174, Univ. of Minn.,  
October 1960.

## APPENDIX

### ACCURACY OF RESULTS

#### 1. Assumptions

A detailed analysis of the error sources inherent in the operation of the wind tunnel and drag force balance has been carried out by Maslach and Talbot.<sup>4</sup> The results of that study apply directly to the present experiments, except as they need be modified by the addition of gas injection through the model.

The reduction of the experimental data to their final form involves a large number of measurements, each contributing a source of error. Following Maslach and Talbot,<sup>4</sup> we assume that all errors are in phase and therefore additive, and are based on known flow irregularities and instrument least counts. This provides a simple and conservative estimate of the accuracy of most of the results. Those results requiring a more sophisticated analysis are discussed separately.

#### 2. Wind Tunnel Flow Conditions

Although the present study employed a different nozzle<sup>7</sup> for the data at  $M_\infty = 3.93$  than that used by Maslach and Talbot,<sup>4</sup> their accuracy analysis for the flow conditions is essentially unchanged. The experimental values of the flow parameters of interest is as follows:

Data at  $M_\infty = 3.93$ :

$M_\infty = 3.925 \pm 0.015$	( $\pm 0.4\%$ )
$\frac{1}{2} \rho_\infty u_\infty^2 = 0.0177 \pm 0.0004 \text{ psi}$	( $\pm 2.3\%$ )
$(Re/in)_\infty = 1765 \pm 35$	( $\pm 2.0\%$ )

$$P_{\infty} = 84.8 \pm 1 \text{ microns Hg.} \quad (\pm 1.2\%)$$

$$T_s = 540 \pm 5 \text{ }^{\circ}\text{R} \quad (\pm 0.9\%)$$

Data at  $M_{\infty} = 5.64$ :

$$M_{\infty} = 5.64 \pm 0.03 \quad (\pm 0.5\%)$$

$$\frac{1}{2} \rho_{\infty} u_{\infty}^2 = 0.0367 \pm 0.0011 \text{ psi} \quad (\pm 3.0\%)$$

$$(Re/in)_{\infty} = 6200 \pm 300 \quad (\pm 4.8\%)$$

$$P_{\infty} = 85.2 \pm 1 \text{ microns Hg.} \quad (\pm 1.2\%)$$

$$T_s = 539 \pm 5 \text{ }^{\circ}\text{R} \quad (\pm 0.9\%)$$

### 3. Pressure Data

A summation of instrument least count and calibration errors suggests that the uncertainty in pressure measurements should be roughly 2% or less. This is also suggested by the small scatter of the data (Figures 11 to 16). As noted in Section 2.4, however, the porous model pressure data were subject to a systematic error of between 5% and 20%, depending on the individual pressure tap.\* Although this was probably mostly accounted for by the correction procedure of Section 2.4, it is felt that the corrected pressure data reported herein might still be in error up to perhaps 5% of the absolute pressure at the higher injection

---

\*Additional error sources arise from possible pressure system leaks or out-gassing. The pressure system was leak-checked and to reduce out-gassing errors was maintained at pressure levels below those of the tests prior to a run. This technique, plus the repeatability and internal consistency of all the pressure data of this report, make errors due to leaks and out-gassing extremely unlikely.

rates. This could produce errors in the self-induced pressure increment  $(P - P_c)/P_c$  up to perhaps 10% at the higher injection rates of the tests and might account for the irregular shape of the pressure distribution curves of Figures 17 and 18 for the higher injection rates.

#### 4. Gross Drag Coefficient

The gross drag coefficient is directly measured (see Section 2.5) and is subject to errors in the measurement of balance spring extension, spring calibration, dynamic pressure, and model and balance geometry. Of these the uncertainty in dynamic pressure is perhaps the most important (see estimates above). Since the balance springs used were such that about 1/2 to 1 inch extension occurred in the tests, errors due to spring calibration and extension readings were probably less than 0.5%. Errors due to the measurement of lever arms and model dimensions were less than 0.2%. An additional scatter in the data of approximately 2% was also introduced, however, probably due to fluctuations in base pressure, as discussed in the next section. The table below summarizes the estimated error in gross drag coefficient for various conditions:

#### Uncertainty in $C_{D_{gross}}$

<u>Free Stream Mach Number:</u>	<u>3.93</u>	<u>5.64</u>
Near Zero Injection Rates:	± 3.4%	± 4.0%
Near Maximum Injection Rates:	± 3.9%	± 4.5%

### 5. Base Pressure and Base Drag

Base pressures were probably read to about  $\pm 3\%$  accuracy, as discussed in Appendix 3 above. The scatter of the base pressure data shown in Figure 20 and the gross force data of Figure 19 and Table IV is probably due to a slight instability in the balance null position due to changes in base pressure with gap opening between the model and afterbody. Thus the average base pressure curve (Figure 20) is probably accurate to  $\pm 5\%$ , as estimated from the scatter of the data.

The base drag (and drag coefficient) was determined by simply multiplying the total cone base area by the base pressure. This seems the most reasonable procedure in the absence of much more detailed information about the pressure distribution on the model support sting. It is estimated that the base drag coefficient error might be as high as  $\pm 10\%$  for the conditions of the experiment.

### 6. Total Drag Coefficient

The total drag coefficient is defined as the sum of pressure, skin friction, and injection gas momentum transfer drag coefficients on the slant face of the cone. It is calculated from the experimental data as gross drag minus base pressure drag:

$$C_{D_{\text{total}}} = \{C_{D_{\text{frict}}} + C_{D_{\text{press}}} + C_{D_{\text{inj}}}\} = \{C_{D_{\text{gross}}} - C_{D_{\text{base}}}\} \quad (\text{A-1})$$

By differentiating the above equation and replacing the differentials by error quantities, the relative error in  $C_{D_{\text{total}}}$  may be expressed as follows:

$$\left( \frac{\Delta C_D}{C_D} \right)_{\text{total}} = \frac{\Delta C_{D_{\text{gross}}} + \Delta C_{D_{\text{base}}}}{C_{D_{\text{total}}}} = \frac{C_{D_g} \left( \frac{\Delta C_{D_g}}{C_{D_g}} \right) + C_{D_b} \left( \frac{\Delta C_{D_b}}{C_{D_b}} \right)}{C_{D_t}} \quad (\text{A-2})$$

The plus sign for  $\Delta C_{D_{\text{base}}}$  is taken because of the assumption that the errors are in phase and therefore additive. Estimates of the possible error in the total drag coefficient are as follows:

Uncertainty in  $C_{D_{\text{total}}}$

<u>Free Stream Mach Number:</u>	<u>3.93</u>	<u>5.64</u>
Near Zero Injection Rates:	± 3.8%	± 4.4%
Near Maximum Injection Rates:	± 4.8%	± 5.2%

#### 7. Pressure Drag Coefficient

The pressure drag coefficient is calculated from the integral of the experimental surface pressure distribution according to Eq. (2.5). Because this distribution is obtained by cross-plotting and extrapolating the pressure data (Figures 17 and 18), it is difficult to estimate the probable uncertainty of the pressure drag coefficient. Probably the order of ± 10% would be a reasonable guess.

#### 8. Injection Drag Coefficient

The injection drag is a theoretically calculated quantity (see Section 2.9) and not of particular interest here, except as needed for the calculation of skin friction drag. Because of the crudeness of the injection drag analysis, one could not claim better than about ± 50% accuracy for this quantity.\*

---

\*Some measurements of the reaction force on the model produced by gas injection (in the quiescent wind tunnel) were in reasonable agreement

### 9. Skin Friction Drag Coefficient

By differentiating the skin friction drag equation (2.3) and changing the differentials to increments, we obtain

$$\frac{\Delta C_{D_f}}{C_{D_f}} = \frac{C_{D_g} \left( \frac{\Delta C_{D_g}}{C_{D_g}} \right) + C_{D_p} \left( \frac{\Delta C_{D_p}}{C_{D_p}} \right) + C_{D_b} \left( \frac{\Delta C_{D_b}}{C_{D_b}} \right) + C_{D_{inj}} \left( \frac{\Delta C_{D_{inj}}}{C_{D_{inj}}} \right)}{C_{D_f}} \quad (A-3)$$

Again only plus signs are used since the error or  $\Delta$  quantities are assumed to be in phase. The conservative estimate of the error in skin friction drag coefficient is as follows:

Uncertainty in  $C_{D_{frict}}$

<u>Free Stream Mach Number:</u>	<u>3.93</u>	<u>5.64</u>
Near Zero Injection Rates:	± 5.3%	± 6.5%
Near Maximum Injection Rates:	±18.8%	±18.0%

### 10. Injection Flow Rate

From Equation (2.15) the error equation for the injection mass flow is as follows (capillary tube meter):

---

(footnote continued from previous page)

with the order of magnitude and trends predicted by the theoretical injection drag analysis. Because of the different model external surface conditions between the "wind on" and "wind off" cases, however, it was felt that the theoretical correction procedure used would give more realistic results for the injection correction.

$$\frac{\Delta \dot{M}_{\text{true}}}{\dot{M}_{\text{true}}} = \frac{\Delta \dot{M}_{\text{std}}}{\dot{M}_{\text{std}}} + 1.75 \frac{\Delta T}{T} + \frac{\Delta P}{P} \quad (\text{A-4})$$

The "standard" mass rate could be determined within about  $\pm 1.5\%$ , as obtained from the scatter in the calibration data and the ability to read the pressure drop across the capillary tube. (Four different size capillary tubes were used so that the pressure drop was always in the range of 5 to 24 inches of water.) The absolute temperature was determined within  $3^\circ\text{R}$ , and the error in pressure reading was less than  $0.5\%$ . From this it is estimated that the injection flow rate was known within  $3\%$  or better.\*

#### 11. Model Temperature

The model temperature was measured by a copper-constantan thermocouple attached to the base (see Figure 8). The potentiometer used to measure the signal had sensitivity equivalent to  $\pm 2^\circ\text{F}$ . The scatter in model temperature (Figure 34) probably results from temperature fluctuations in the laboratory, since the stagnation temperature used for data reduction was an overall average for each run. Since the injection rate was changed about every ten minutes, it is also possible that temperatures were recorded before thermal equilibrium was established.

#### 12. Local Injection Flux Distribution

The method of local flux measurement described in Section 2.11 is quite crude and is probably only indicative of the true local flux

---

\*This does not apply to flow rates of helium above about  $0.09 \text{ lb/hr}$ , where Fischer-Porter flow meter was used. In this case the estimated injection rate error is  $\pm 5\%$ .

distribution. In addition, the method only gives the circumferentially averaged values of local mass flux. From the scatter of the data of Figure 37, one sees that the slopes required for Equation (2.14) can be estimated within only about  $\pm 10\%$  at best. Hence the curves of Figure 38 are accurate within probably 10% to 20%.

TABLE I

Uncorrected Zero Injection Pressure Data\* -- Values of  $P/P_c$

(a)  $M_\infty = 3.93$

Tap Number	1	2	3	4	5	6
Standard	1.131	1.108	1.100	1.091	1.088	1.086
Cone Probes	1.122	1.108	1.098	1.090	1.083	1.090
Solid Model	1.192	1.128	1.122	1.104	1.090	1.094
Porous Models	1.266	1.160	1.178	1.184	1.288	1.275

$P_c = 108$  microns Hg.

$P_\infty = 84.8$  microns Hg.

(b)  $M_\infty = 5.64$

Tap Number	1	2	3	4	5	6
Standard	1.187	1.155	1.137	1.112	1.098	1.090
Cone Probes	1.187	1.166	1.140	1.109	1.090	1.090
Solid Model	1.265	1.190	1.190	1.140	1.130	1.097
Porous Models	1.340	1.246	1.192	1.231	1.278	1.310

$P_c = 127$  microns Hg.

$P_\infty = 85.2$  microns Hg.

\*Values shown are averages of at least three measurements. The scatter of the data was roughly  $\pm 2\%$ , and is indicated in Figure 10.

TABLE II

1,3,5 Model Pressure Data -- Corrected\* Values of  $(P-P_c)/P_c$

(a)  $M_\infty = 3.93$  -- Air Injection

$\dot{M}$ lb/hr	Tap No. 1 Z = 1.25 in	Tap No. 3 Z = 2.0 in	Tap No. 5 Z = 2.75 in
.0230	.125	.105	.085
.0445	.145	.135	.085
.0675	.150	.170	.085
.0985	.175	.205	.100
.115	.185	.220	.105
.140	.200	.255	.115
.160	.250	.305	.145
.180	.265	.305	.145
.210	.315	.385	.160
.240	.400	.435	.175
.265	.465	.485	.195
.285	.515	.505	.205
.310	.555	.530	.210
.330	.585	.545	.215

(b)  $M_\infty = 3.93$  -- Helium Injection

$\dot{M}$ lb/hr	Tap No. 1 Z = 1.25 in	Tap No. 3 Z = 2.0 in	Tap No. 5 Z = 2.75 in
.00795	.140	.125	.110
.0151	.160	.170	.135
.0230	.170	.185	.140
.0325	.185	.225	.165
.0450	.220	.285	.180
.0610	.275	.340	.210
.0715	.320	.380	.235
.0825	.375	.430	.250
.0945	.430	.465	.280
.105	.455	.500	.285

\*See Section 2.4

TABLE II

1,3,5 Model Pressure Data -- Corrected\* Values of  $(P-P_c)/P_c$

(c)  $M_\infty = 5.64$  -- Air Injection

$\dot{M}$ lb/hr	Tap No. 1 Z = 1.25 in	Tap No. 3 Z = 2.0 in	Tap No. 5 Z = 2.75 in
.0185	.210	.165	.095
.0320	.200	.175	.095
.0640	.200	.210	.100
.0830	.215	.240	.110
.110	.230	.270	.120
.135	.265	.335	.155
.155	.300	.395	.180
.175	.320	.435	.190
.200	.365	.485	.215
.210	.370	.490	.215
.235	.455	.560	.255
.240	.440	-	-
.270	.540	.640	.275
.300	.615	.700	.300
.310	.650	.715	.305
.320	.650	.720	.300

(d)  $M_\infty = 5.64$  - Helium Injection

$\dot{M}$ lb/hr	Tap No. 1 Z = 1.25 in	Tap No. 3 Z = 2.0 in	Tap No. 5 Z = 2.75 in
.0120	.215	.210	.155
.0125	.220	.225	.155
.0165	.225	.235	.165
.0230	.245	.270	.180
.0345	.270	.340	.205
.0470	.320	.405	.255
.0560	.336	.430	.265
.0585	.360	.465	.290
.0725	.425	.545	.330
.0840	.470	.585	.355
.0930	.490	.610	.360
.0935	.470	.585	.370
.101	.490	.625	.375
.104	.540	.650	.380
.111	.540	.660	.400
.116	.580	.685	.395

\*See Section 2.4

TABLE III2,4,6 Model Pressure Data - Corrected\* Values of  $(P-P_c)/P_c$ (a)  $M_\infty = 3.93$  -- Air Injection

$\dot{M}$ lb/hr	Tap No. 2 Z = 1.75 in	Tap No. 4 Z = 2.5 in	Tap No. 6 Z = 3.0 in
.0195	.115	.100	.080
.0345	.125	.110	.070
.0525	.145	.115	.080
.0655	.150	.110	.055
.0705	.145	.100	.040
.0845	.160	.125	-
.103	.185	.135	.035
.120	.205	.160	.045
.135	.225	.150	.030
.150	.240	.135	.015
.155	.260	.160	.030
.190	.300	.185	.015
.205	.325	.175	.010
.215	.335	.195	.005
.235	.365	.210	.000
.245	.395	.205	.010
.255	.405	.220	.015
.270	.415	.225	.005
.275	.440	.245	.015
.285	.435	.215	.010
.300	.460	.235	.000
.310	.470	.235	.000
.320	.480	.245	.005
.325	.480	.235	.010
.340	.495	.245	.005

\*See Section 2.4

TABLE III

2.4,6 Model Pressure Data -- Corrected\* Values of  $(P-P_c)/P_c$

(b)  $M_\infty = 3.93$  -- Helium Injection

$\dot{M}$ lb/hr	Tap No. 2 Z = 1.75 in	Tap No. 4 Z = 2.5 in	Tap No. 6 Z = 3.0 in
.0088	.140	.125	.095
.0134	.160	.140	.105
.0164	.160	.145	.100
.0225	.185	.155	.105
.0265	.180	.160	.095
.0291	.200	.175	.105
.0345	.220	.190	.105
.0435	.250	.205	.105
.0475	.265	.195	.110
.0500	.270	.225	.110
.0525	.290	.225	.120
.0570	.305	.230	.120
.0625	.315	.240	.120
.0670	.335	.235	.115
.0690	.340	.255	.125
.0755	.360	.265	.120
.0765	.350	.245	.125
.0815	.390	.280	.135
.0935	.430	.300	.135
.095	.395	.280	.140
.099	.410	.285	.125
.108	.405	.280	.125
.111	.445	.295	.125
.115	.430	.315	.135
.122	.475	.305	-

\*See Section 2.4

TABLE III

2,4,6 Model Pressure Data -- Corrected\* Values of  $(P-P_c)/P_c$ (c)  $M_\infty = 5.64$  -- Air Injection

$\dot{M}$ lb/hr	Tap No. 2 Z = 1.75 in	Tap No. 4 Z = 2.5 in	Tap No. 6 Z = 3.0 in
.0120	.185	.125	.105
.0310	.185	.125	.075
.0430	.175	.125	.070
.0530	.205	.140	.085
.0570	.210	.125	.060
.0595	.215	.140	.065
.0740	.220	.145	.065
.0835	.235	.145	.055
.0870	.235	.145	.070
.0920	.250	.155	.065
.110	.270	.165	.055
.121	.290	.175	.055
.125	.295	.175	.050
.135	.305	.175	.050
.135	.310	.190	.055
.145	.340	.195	.070
.165	.360	.210	.055
.180	.370	.225	.050
.184	.390	.225	.055
.195	.435	.260	.075
.205	.435	.255	.050
.245	.530	.305	.085
.245	.545	.300	.080
.245	.520	.270	.060
.265	.565	.315	.085
.290	.615	.335	.080
.295	.625	.330	.085
.310	.630	.320	.075
.320	.655	.345	.070
.325	.675	.355	.085
.340	.680	.360	.075

\* See Section 2.4

TABLE III

2,4,6 Model Pressure Data -- Corrected\* Values of  $(P-P_c)/P_c$ (d)  $M_\infty = 5.64$  -- Helium Injection

$\dot{M}$ lb/hr	Tap No. 2 Z = 1.75 in	Tap No. 4 Z = 2.5 in	Tap No. 6 Z = 3.0 in
.00595	.160	.130	.085
.0015	.205	.160	.105
.0120	.215	.155	.125
.0180	.255	.125	.125
.0200	.250	.200	.115
.0240	.265	.200	.135
.0265	.300	.220	.110
.0285	.285	.230	.130
.0330	.330	.265	.145
.0350	.325	.225	.140
.0400	.365	.300	.140
.0400	.350	.240	.125
.0470	.395	.300	.185
.0495	.380	.275	.160
.0525	.410	.315	.175
.0530	.385	.315	.170
.0620	.445	.330	.165
.0620	.430	.315	.160
.0670	.460	.315	.180
.0685	.485	.335	.175
.0770	.520	.370	.190
.0790	.525	.350	.195
.0820	.540	.390	.195
.0870	.570	.405	.215
.0935	.605	.400	.210
.0970	.595	.405	.195
.107	.630	.415	.205
.108	.630	.405	.210
.117	.680	.435	.225
.119	.685	.440	.225

\* See Section 2.4

TABLE IV

Experimental Gross Drag Coefficient Data\*(a)  $M_\infty = 3.93$ 

Air Injection		Helium Injection	
$\dot{M}$ lb/hr	$C_{D_{gross}}$	$\dot{M}$ lb/hr	$C_{D_{gross}}$
0	.358	0	.359
0	.360	0	.360
0	.360	0	.360
0	.360	0	.360
0	.360	.0064	.348
0	.360	.0135	.336
.020	.323	.0165	.332
.0325	.305	.0205	.328
.036	.300	.0275	.316
.0440	.286	.031	.314
.0495	.283	.0335	.310
.0640	.263	.0405	.302
.0670	.258	.0480	.294
.0815	.244	.0525	.291
.0825	.243	.0580	.285
.0865	.235	.0650	.282
.0995	.226	.0655	.279
.101	.2265	.0735	.275
.102	.226	.0760	.273
.125	.207	.0835	.270
.130	.205	.0890	.267
.130	.2005	.0960	.265
.145	.193	.101	.262
.165	.1855	.1025	.261
.190	.1765	.109	.258
.190	.176		
.215	.171		
.215	.1705		
.240	.1675		
.255	.168		
.265	.1645		
.300	.166		
.305	.1645		
.320	.169		
.340	.167		

\* "Gross Drag" is defined in Section 2.5

TABLE IV

Experimental Gross Drag Coefficient Data\*(b)  $M_\infty = 5.64$ 

Air Injection		Helium Injection	
$\dot{M}$ lb/hr	$C_{D_{gross}}$	$\dot{M}$ lb/hr	$C_{D_{gross}}$
.0105	.2105	0	.220
.0145	.206	0	.220
.0195	.203	0	.220
.022	.201	0	.220
.030	.193	0	.220
.0365	.190	.0041	.217
.045	.182	.0103	.2125
.0545	.176	.0106	.2105
.0595	.173	.0113	.2125
.067	.1665	.0123	.2115
.0855	.1605	.0190	.207
.0895	.155	.0210	.206
.0895	.154	.0215	.206
.0965	.1515	.0225	.207
.0980	.147	.0230	.205
.0985	.149	.0285	.201
.105	.145	.0320	.201
.115	.1415	.0360	.197
.125	.137	.0405	.195
.130	.1355	.0460	.194
.145	.134	.0470	.192
.165	.125	.0550	.189
.165	.1245	.0605	.1875
.170	.1255	.0625	.1855
.175	.124	.0690	.183
.195	.119	.0730	.183
.200	.118	.0740	.181
.200	.1225	.0865	.178
.230	.115	.0865	.178
.240	.115	.1035	.1745
.240	.115		
.250	.1175		
.260	.1135		
.265	.116		
.285	.117		
.300	.1165		

\* "Gross drag" is defined in Section 2.5

TABLE V

Reduced Drag Coefficient Data(a)  $M_\infty = 3.93$  -- Air Injection

$\dot{M}$ lb/hr	$C_{D\text{ gross}}$	$C_{D\text{ base}}$	$C_{D\text{ press}}$	$C_{D\text{ inj}}$	$C_{D\text{ frict}}$	$C_{D\text{ total}}$
0	.3600	-.0255	.0374	0	.3481	.3855
.02	.3230	-.0256	.0377	.0001	.3108	.3486
.04	.2940	-.0257	.0381	.0004	.2812	.3197
.06	.2670	-.0258	.0386	.0007	.2535	.2928
.08	.2450	-.0259	.0393	.0010	.2306	.2709
.10	.2265	-.0260	.0401	.0014	.2110	.2525
.12	.2102	-.0261	.0411	.0020	.1932	.2363
.14	.1970	-.0262	.0423	.0027	.1782	.2232
.16	.1870	-.0263	.0440	.0035	.1658	.2133
.18	.1794	-.0264	.0457	.0043	.1558	.2058
.20	.1739	-.0265	.0477	.0053	.1474	.2004
.22	.1702	-.0266	.0500	.0063	.1405	.1968
.24	.1680	-.0267	.0523	.0073	.1351	.1947
.26	.1666	-.0268	.0545	.0085	.1304	.1934
.28	.1660	-.0269	.0563	.0097	.1269	.1929
.30	.1660	-.0270	.0578	.0111	.1241	.1930
.32	.1665	-.0271	.0590	.0124	.1222	.1936

(b)  $M_\infty = 3.93$  -- Helium Injection

$\dot{M}$ lb/hr	$C_{D\text{ gross}}$	$C_{D\text{ base}}$	$C_{D\text{ press}}$	$C_{D\text{ inj}}$	$C_{D\text{ frict}}$	$C_{D\text{ total}}$
0	.3600	-.0255	.0374	0	.3481	.3855
.01	.3421	-.0273	.0393	.0000	.3301	.3694
.02	.3269	-.0292	.0419	.0001	.3141	.3561
.03	.3140	-.0312	.0445	.0005	.3002	.3452
.04	.3025	-.0330	.0474	.0012	.2869	.3355
.05	.2925	-.0348	.0507	.0023	.2743	.3273
.06	.2839	-.0367	.0541	.0034	.2631	.3206
.07	.2768	-.0386	.0577	.0045	.2532	.3154
.08	.2711	-.0404	.0614	.0058	.2443	.3115
.09	.2663	-.0422	.0653	.0072	.2360	.3085
.10	.2621	-.0441	.0694	.0088	.2280	.3062
.11	.2580	-.0460	.0737	.0108	.2195	.3040

TABLE V

## Reduced Drag Coefficient Data

(c)  $M_\infty = 5.64$  -- Air Injection

$\dot{M}$ lb/hr	$C_{D_{gross}}$	$C_{D_{base}}$	$C_{D_{press}}$	$C_{D_{inj}}$	$C_{D_{frict}}$	$C_{D_{total}}$
0	.2200	-.0154	.0306	0	.2048	.2354
.02	.2028	-.0153	.0307	.0000	.1874	.2181
.04	.1863	-.0152	.0309	.0000	.1706	.2015
.06	.1720	-.0151	.0312	.0001	.1558	.1871
.08	.1596	-.0150	.0317	.0003	.1426	.1746
.10	.1490	-.0150	.0323	.0006	.1311	.1640
.12	.1402	-.0149	.0332	.0009	.1210	.1551
.14	.1332	-.0149	.0342	.0011	.1128	.1481
.16	.1272	-.0148	.0355	.0013	.1052	.1420
.18	.1226	-.0148	.0367	.0017	.0990	.1374
.20	.1195	-.0147	.0380	.0021	.0941	.1342
.22	.1176	-.0147	.0395	.0025	.0903	.1323
.24	.1165	-.0146	.0411	.0029	.0871	.1311
.26	.1160	-.0146	.0427	.0033	.0846	.1306
.28	.1160	-.0145	.0444	.0038	.0823	.1305
.30	.1161	-.0144	.0460	.0043	.0802	.1305
.32	.1165	-.0143	.0477	.0051	.0780	.1308

(d)  $M_\infty = 5.64$  -- Helium Injection

$\dot{M}$ lb/hr	$C_{D_{gross}}$	$C_{D_{base}}$	$C_{D_{press}}$	$C_{D_{inj}}$	$C_{D_{frict}}$	$C_{D_{total}}$
0	.2200	-.0154	.0306	0	.2048	.2354
.01	.2133	-.0166	.0325	.0000	.1974	.2299
.02	.2070	-.0179	.0344	.0000	.1905	.2249
.03	.2012	-.0191	.0362	.0001	.1840	.2203
.04	.1959	-.0203	.0380	.0005	.1777	.2162
.05	.1912	-.0216	.0397	.0009	.1722	.2128
.06	.1870	-.0228	.0415	.0013	.1670	.2098
.07	.1832	-.0240	.0432	.0017	.1623	.2072
.08	.1799	-.0252	.0448	.0022	.1581	.2051
.09	.1773	-.0263	.0465	.0027	.1544	.2036
.10	.1753	-.0276	.0481	.0034	.1514	.2029
.11	.1735	-.0288	.0495	.0042	.1486	.2023



FIG. 1 LOW DENSITY WIND TUNNEL

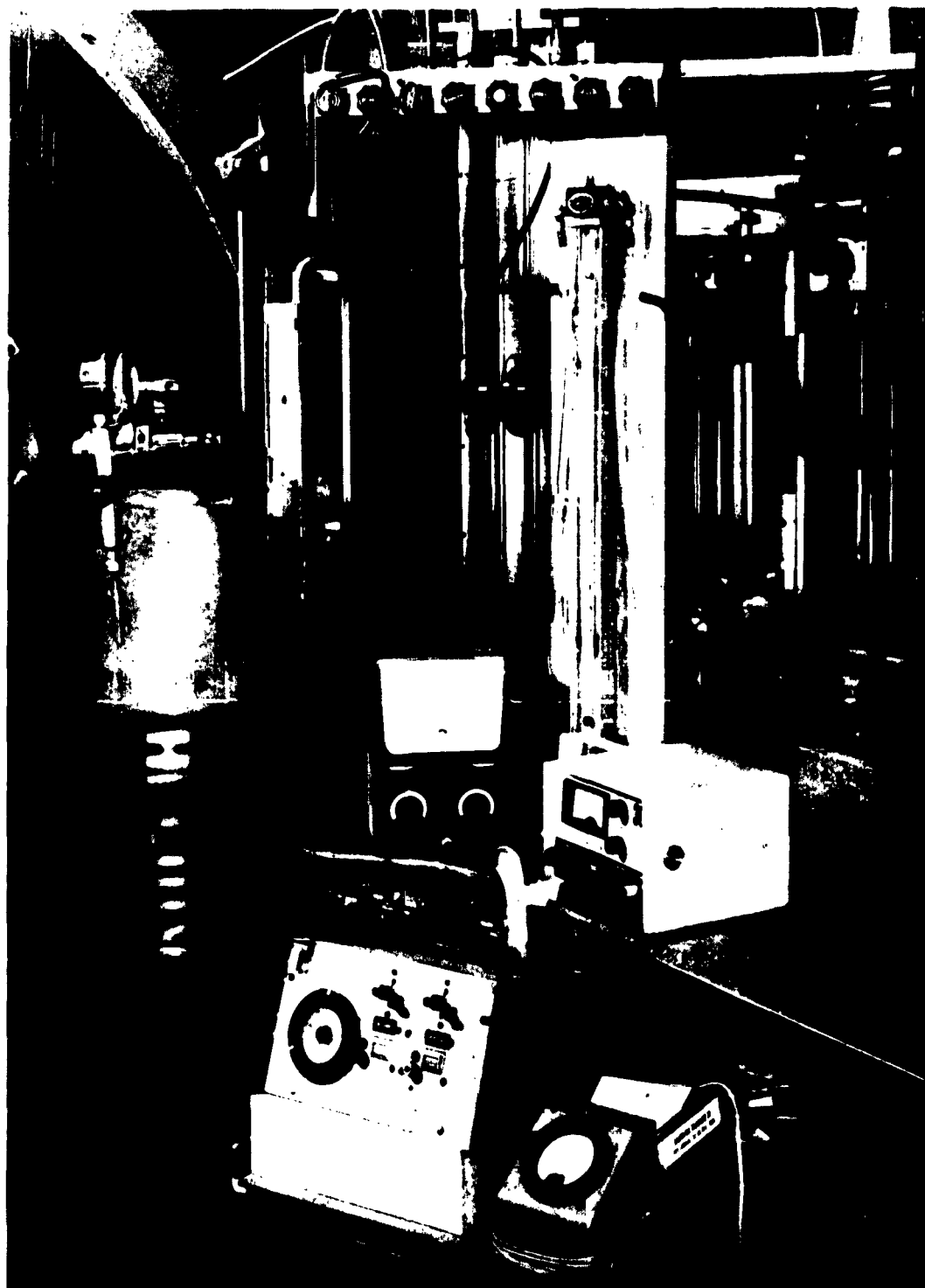


FIG. 2 WIND TUNNEL AND EXPERIMENTAL INSTRUMENTATION

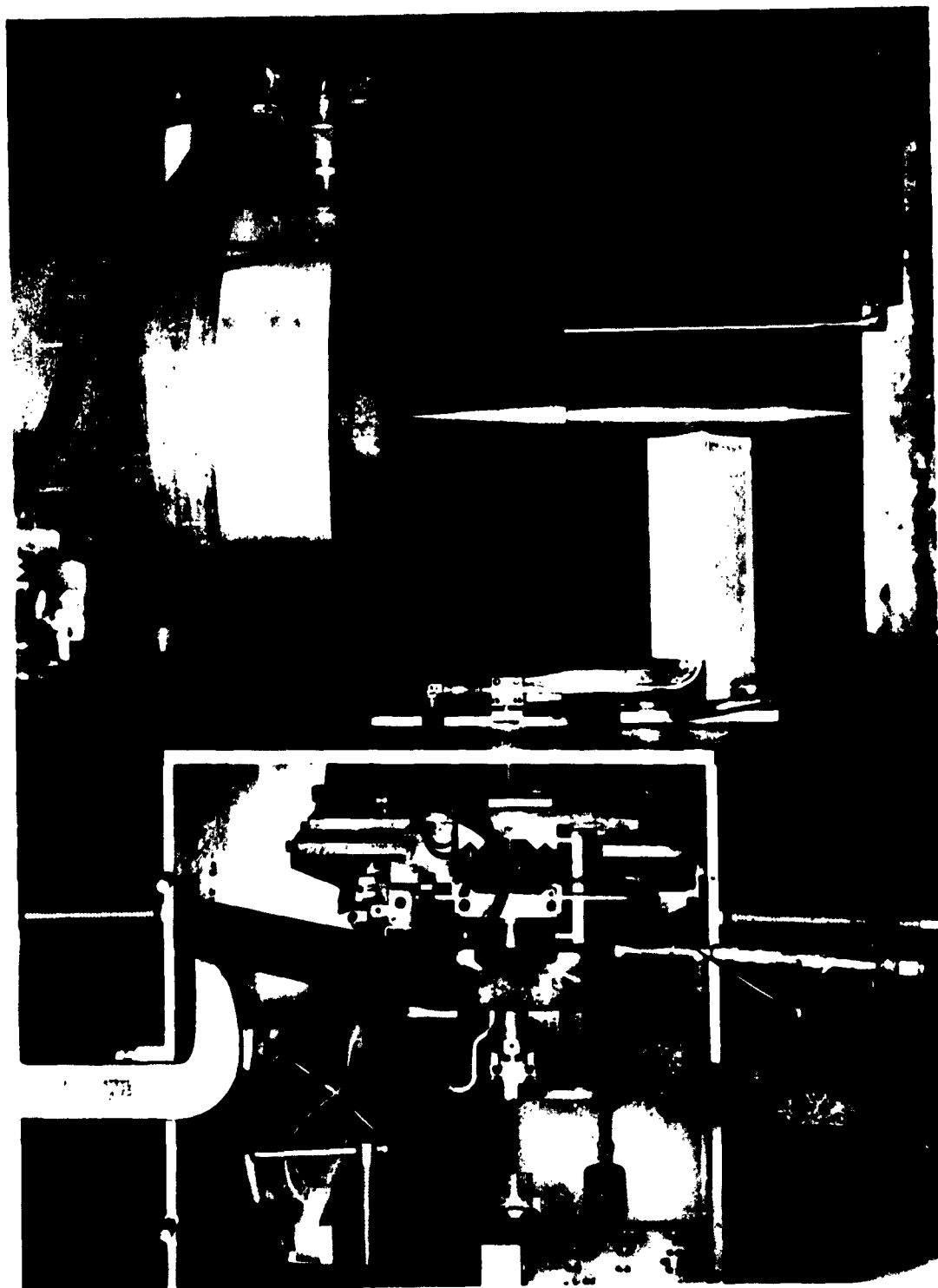


FIG. 3 DRAG FORCE APPARATUS



FIG. 4 PRESSURE DISTRIBUTION APPARATUS

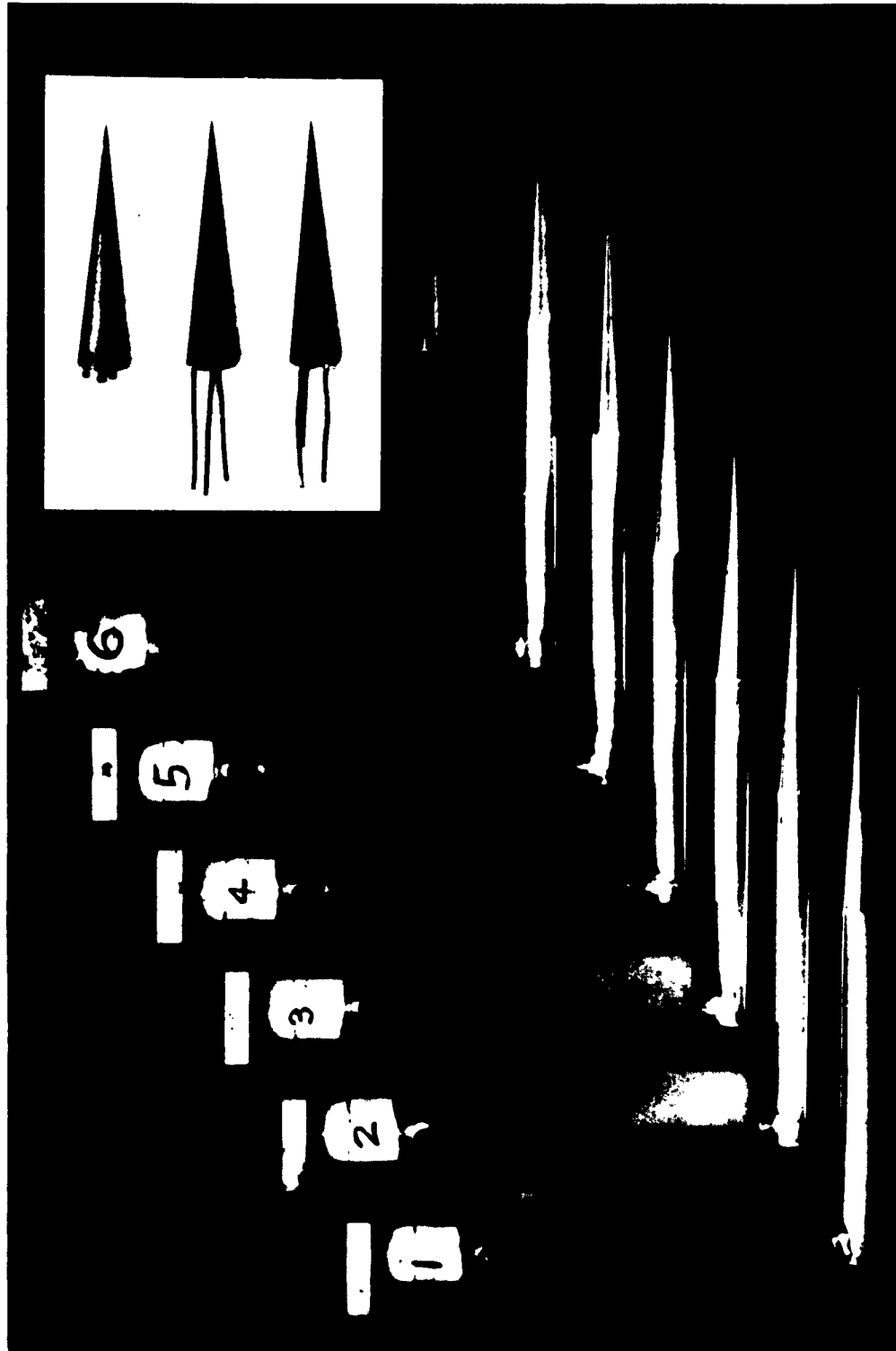
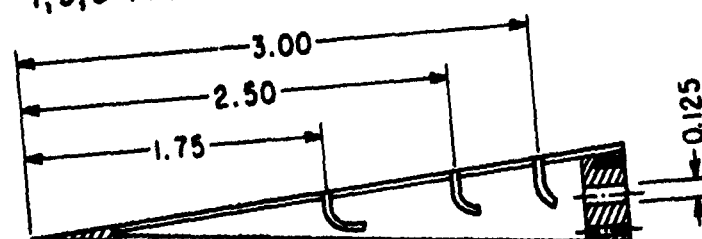
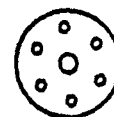
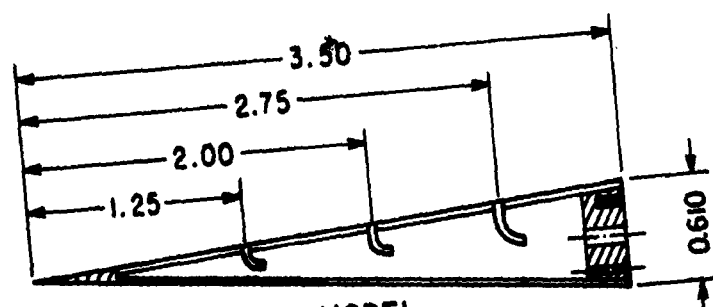
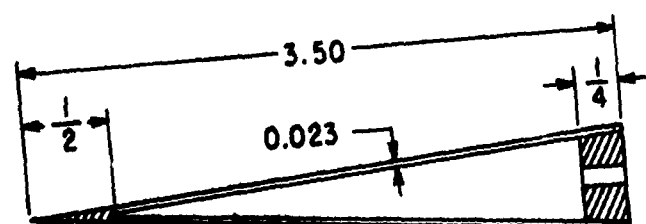


FIG. 5 TEST MODELS: (FROM BOTTOM) CONE PRESSURE PROBES, SOLID PRESSURE MODEL, 1,3,5 PRESSURE MODEL, 2,4,6 PRESSURE MODEL, FORCE MODEL.



2,4,6 PRESSURE MODEL



TAP	1	2	3
Z-IN	1.25	1.75	2.00

TAP	4	5	6
Z-IN	2.50	2.75	3.00

FORCE MODEL



SOLID PRESSURE MODEL

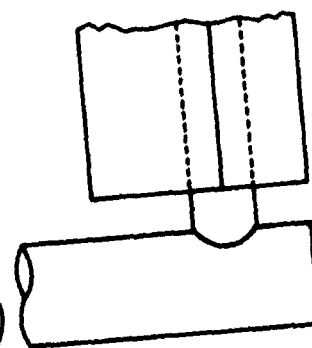
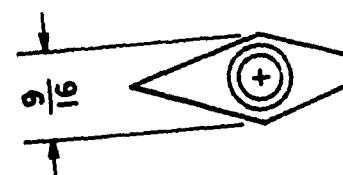
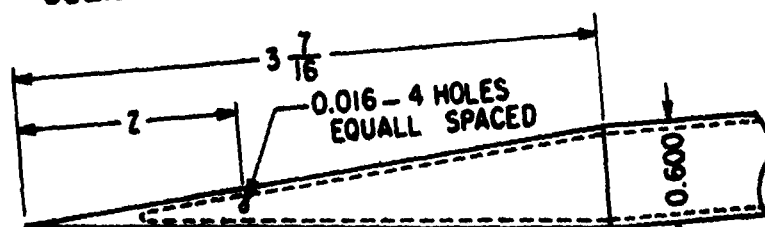


FIG. 6 MODEL DIMENSIONS

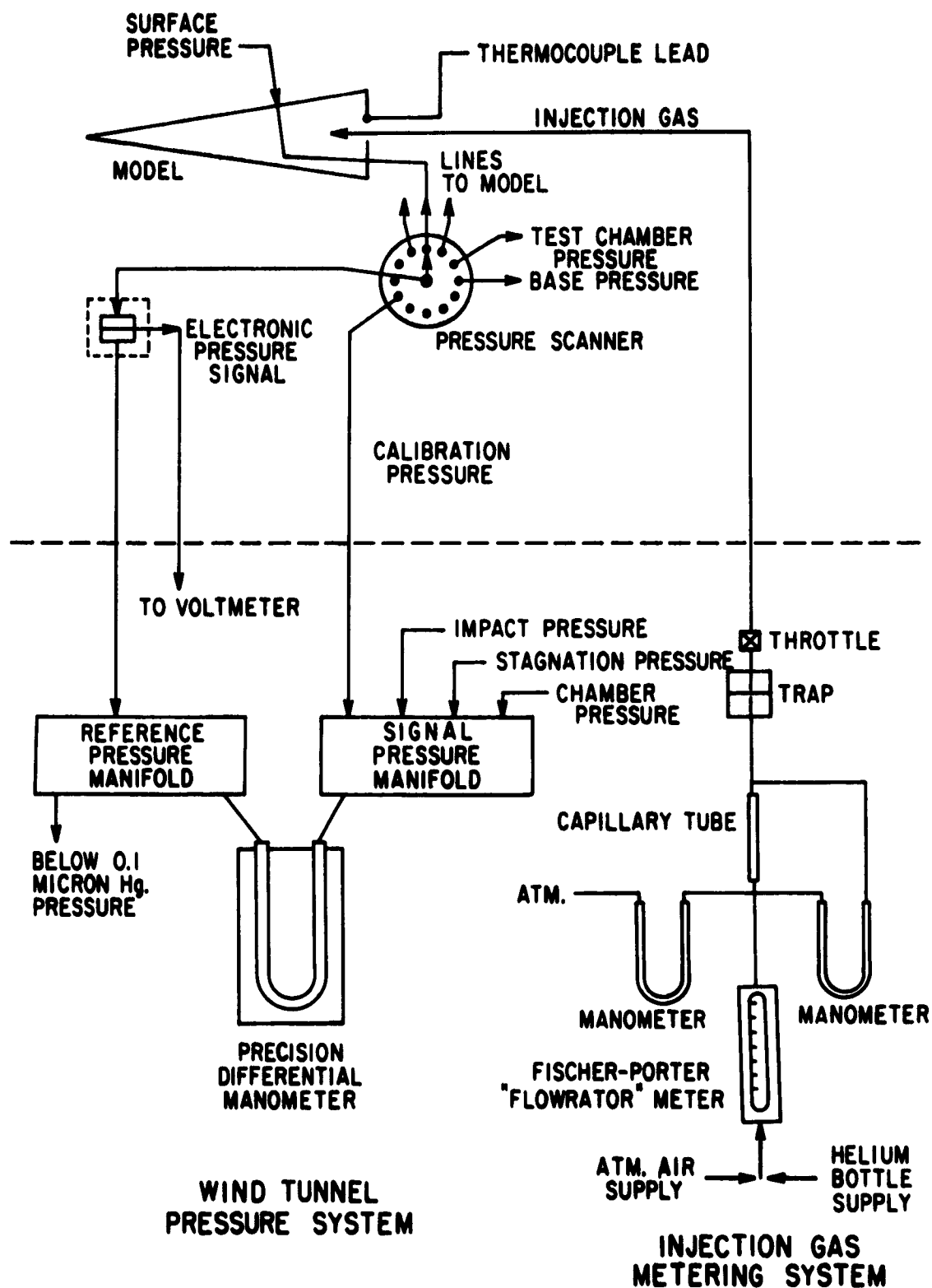


FIG. 7 INJECTION FLOW AND PRESSURE SYSTEM

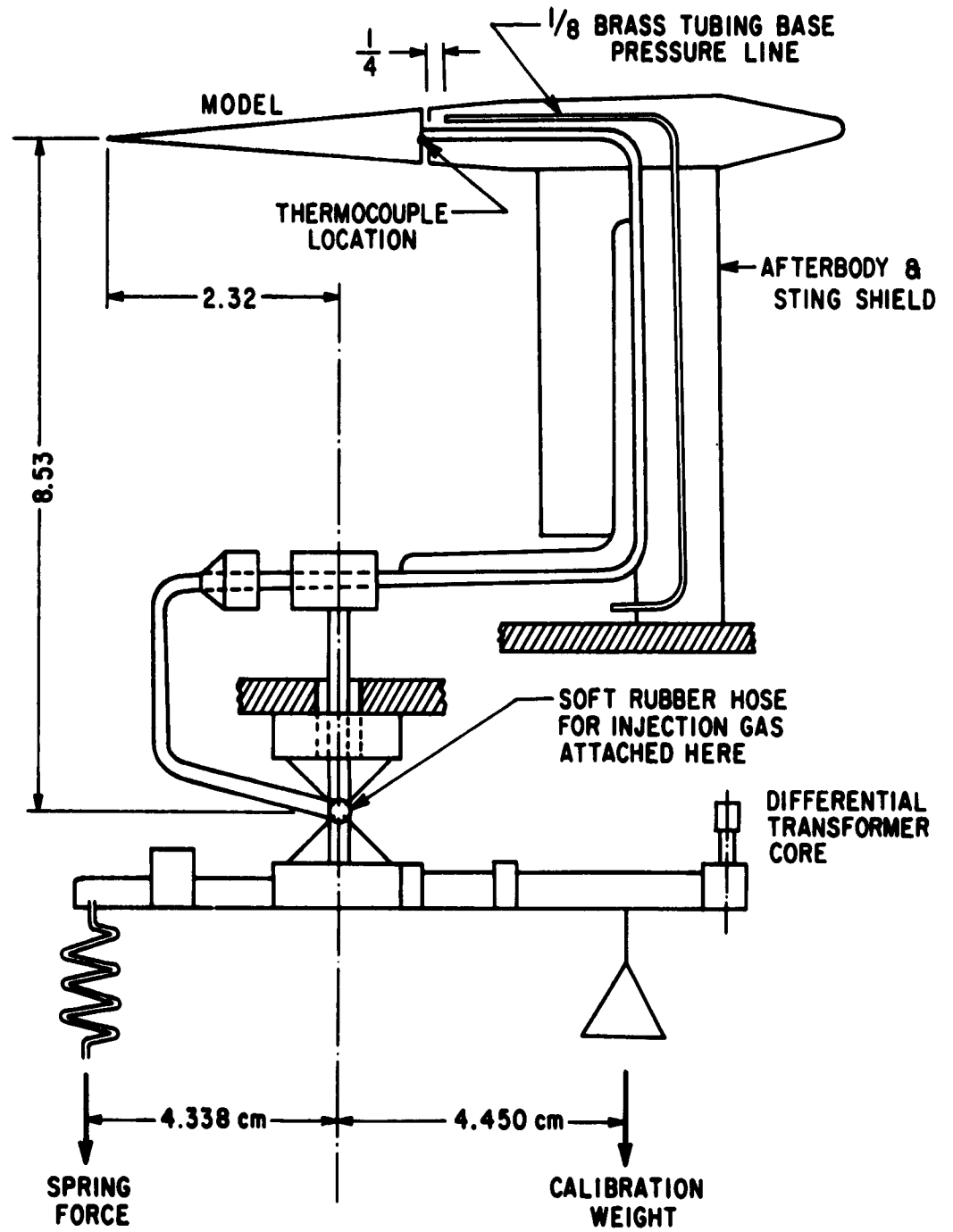


FIG. 8 MOUNTING OF THE FORCE MODEL

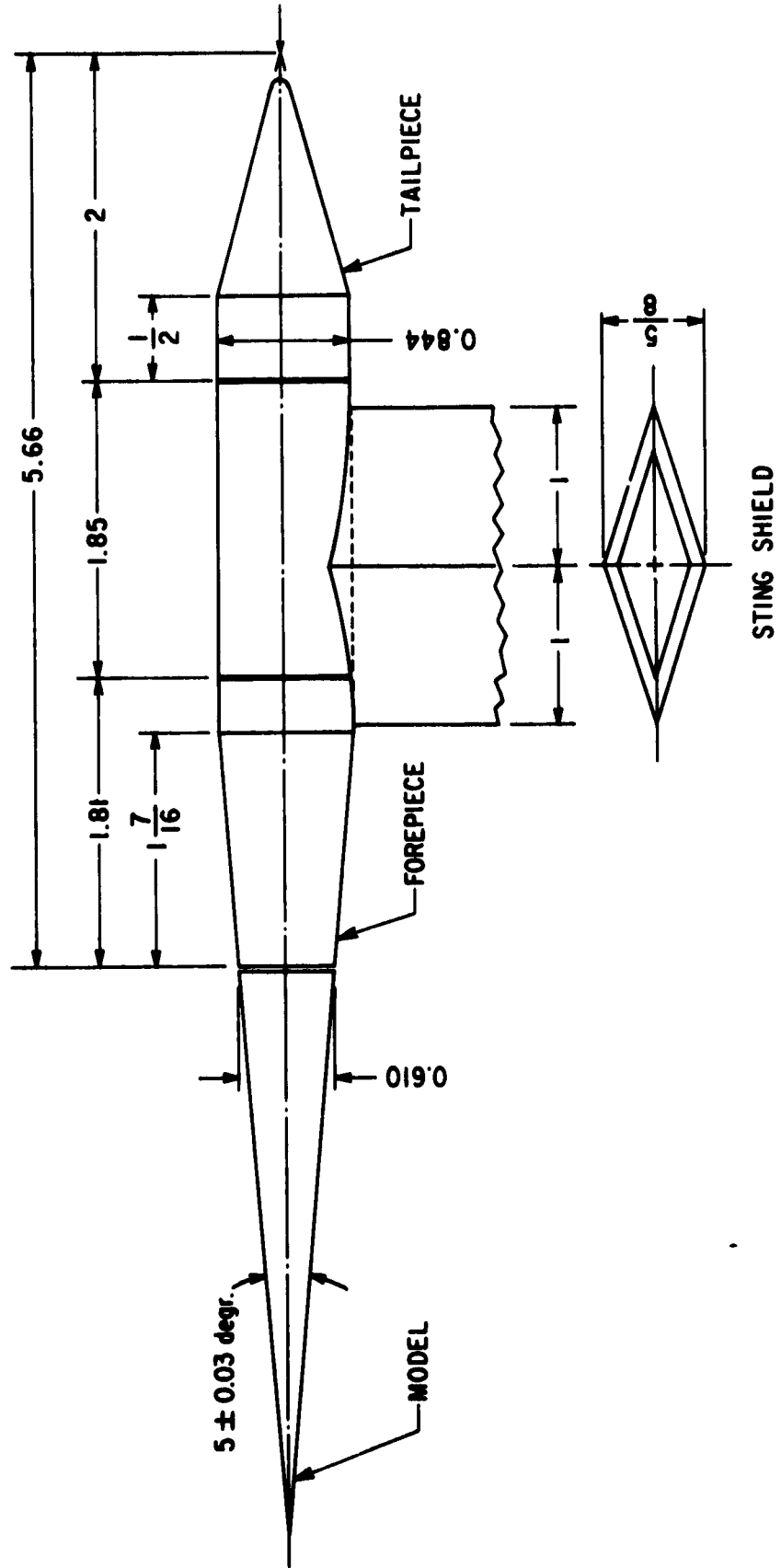


FIG. 9 AFTERBODY AND STING-SHIELD GEOMETRY

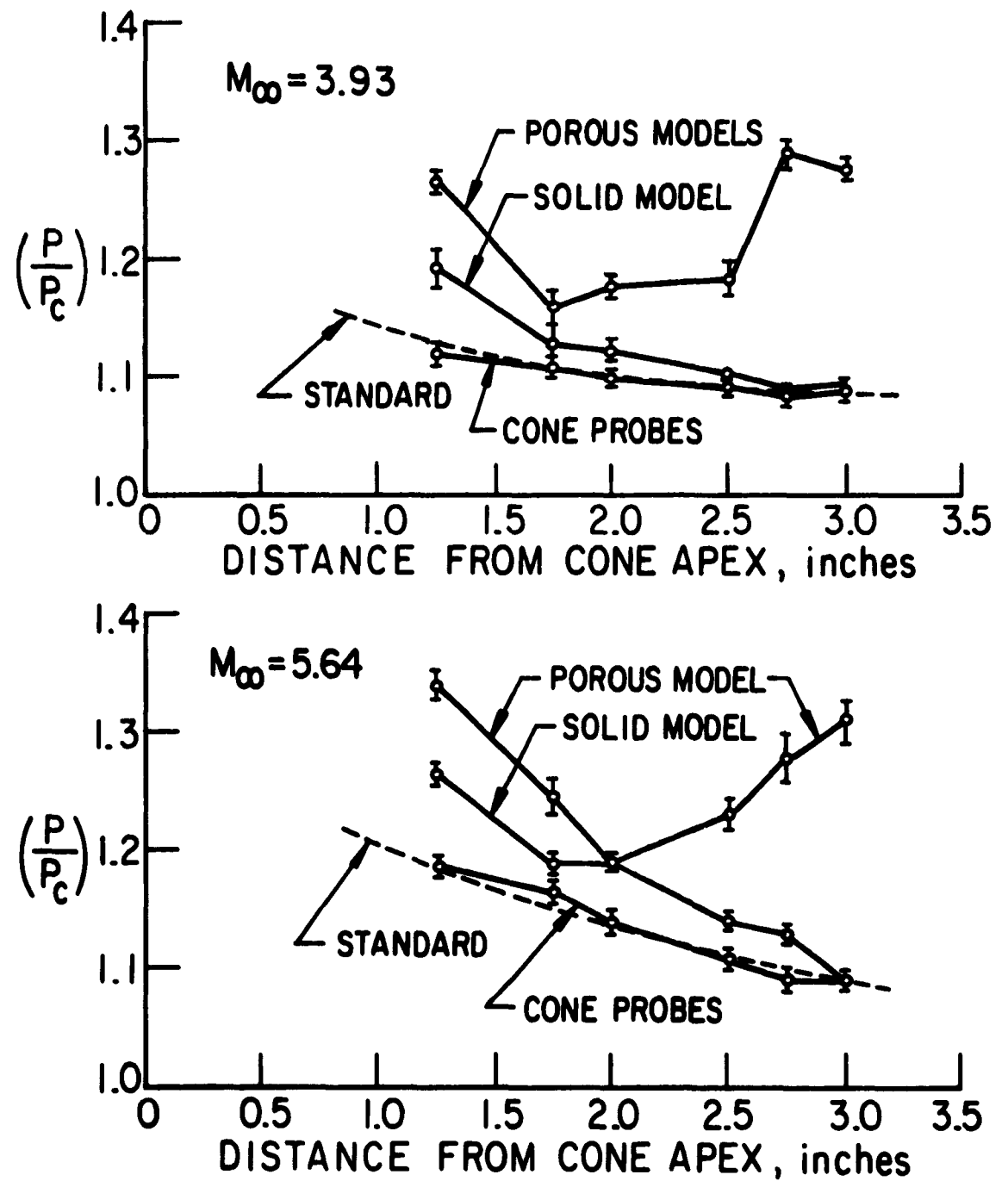


FIG. 10. UNCORRECTED EXPERIMENTAL PRESSURE DISTRIBUTION FOR ZERO INJECTION

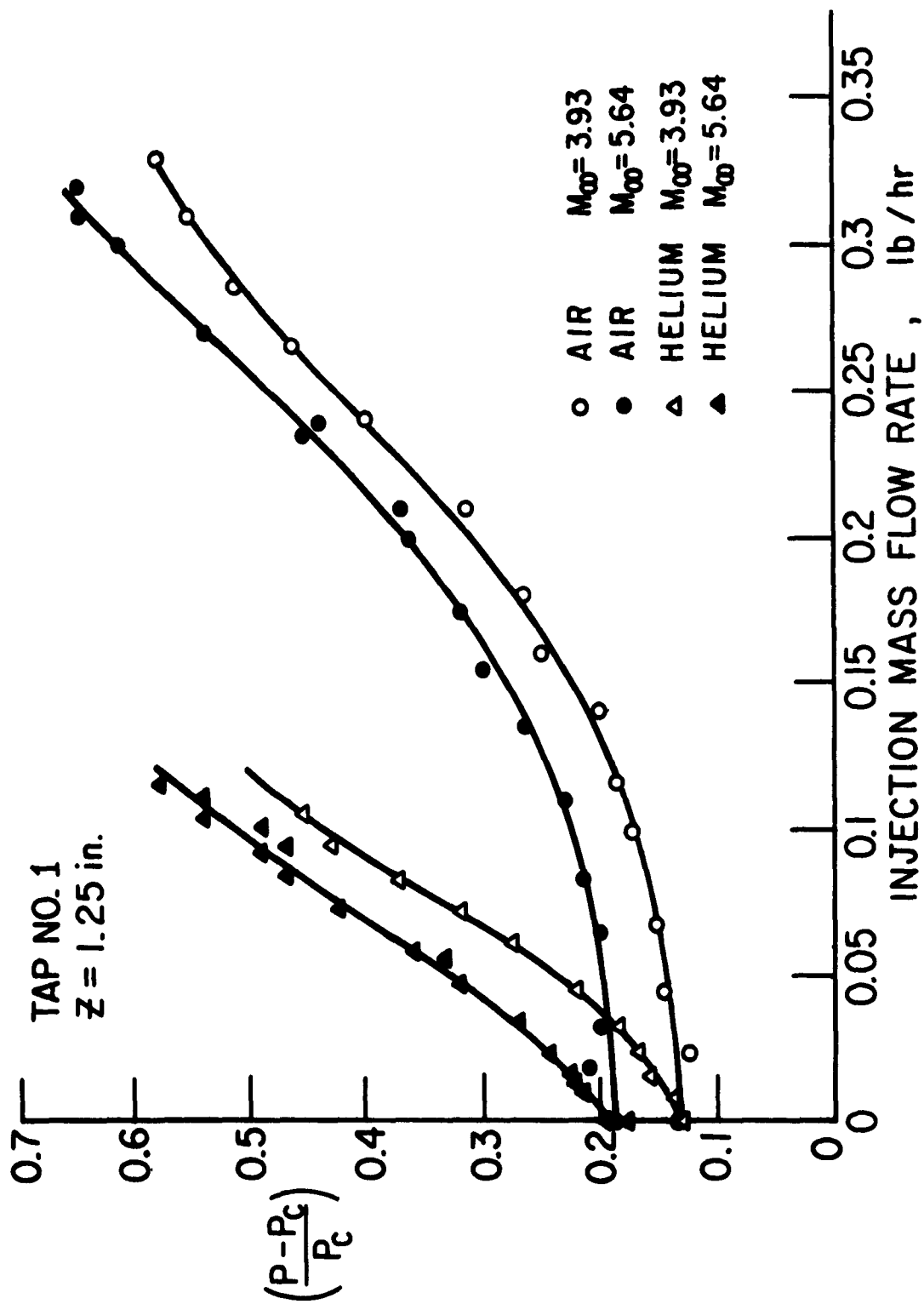


FIG. 11 INDUCED SURFACE PRESSURE AT TAP NO. 1

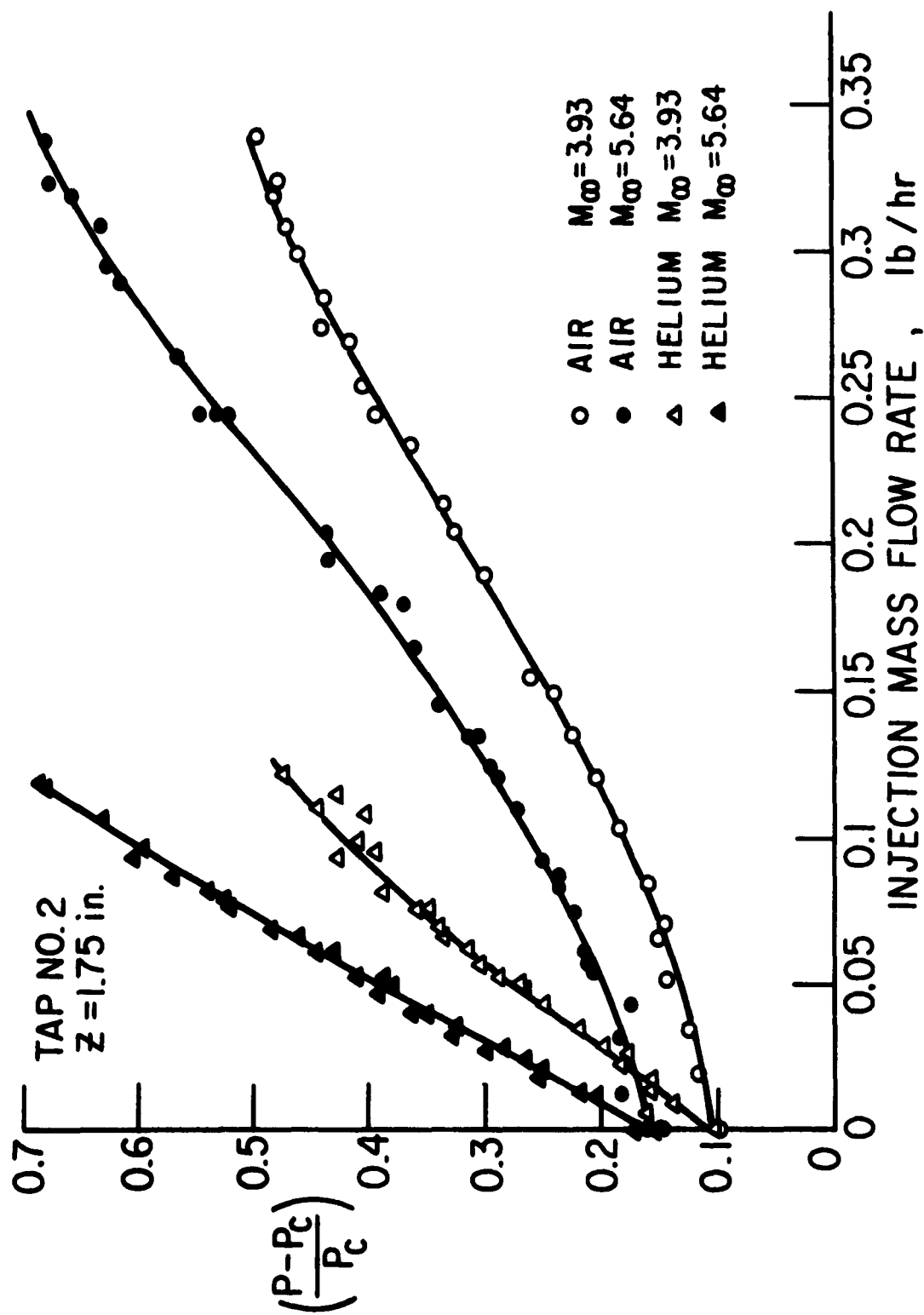


FIG. 12 INDUCED SURFACE PRESSURE AT TAP NO. 2

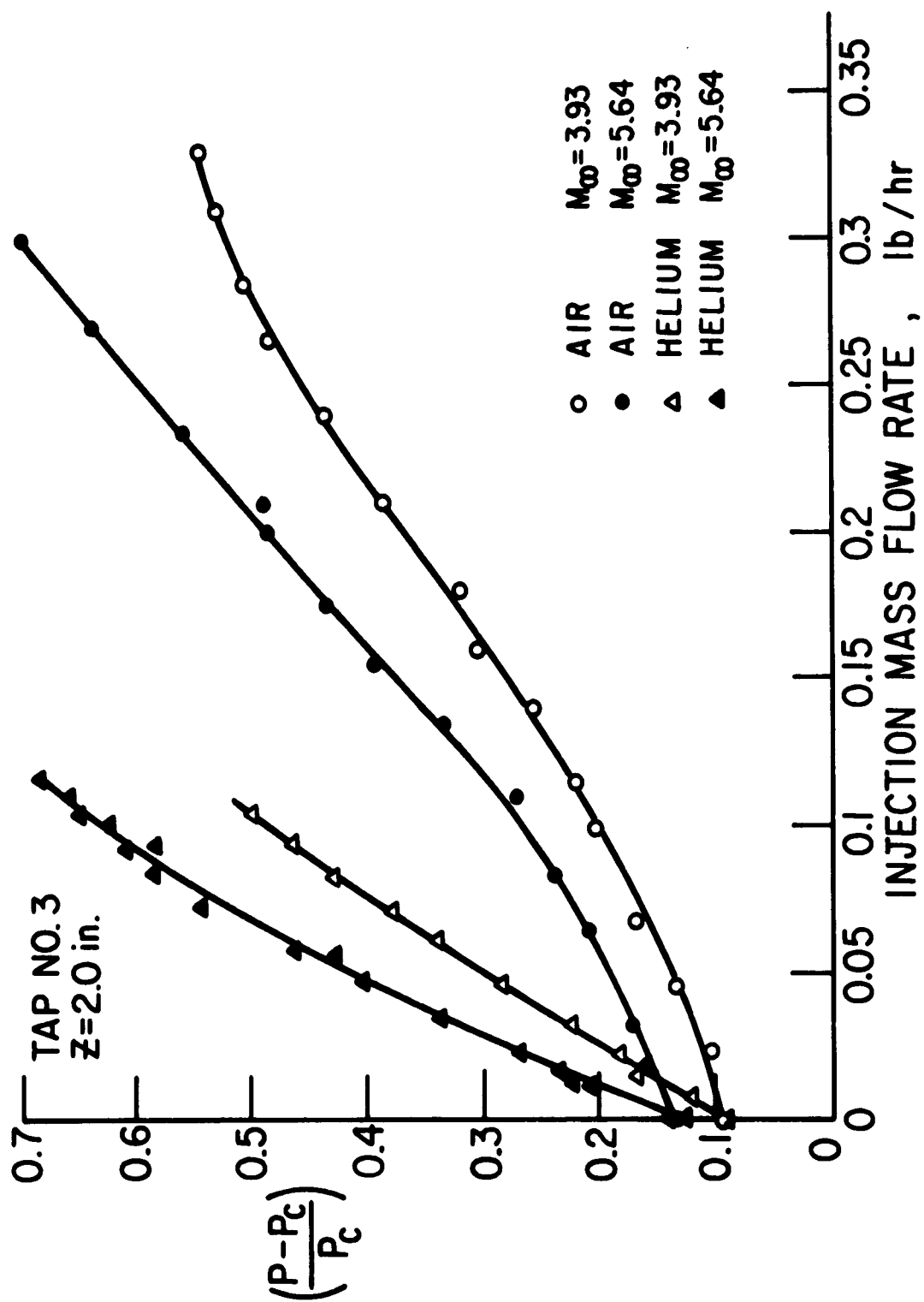


FIG. 13 INDUCED SURFACE PRESSURE AT TAP NO. 3

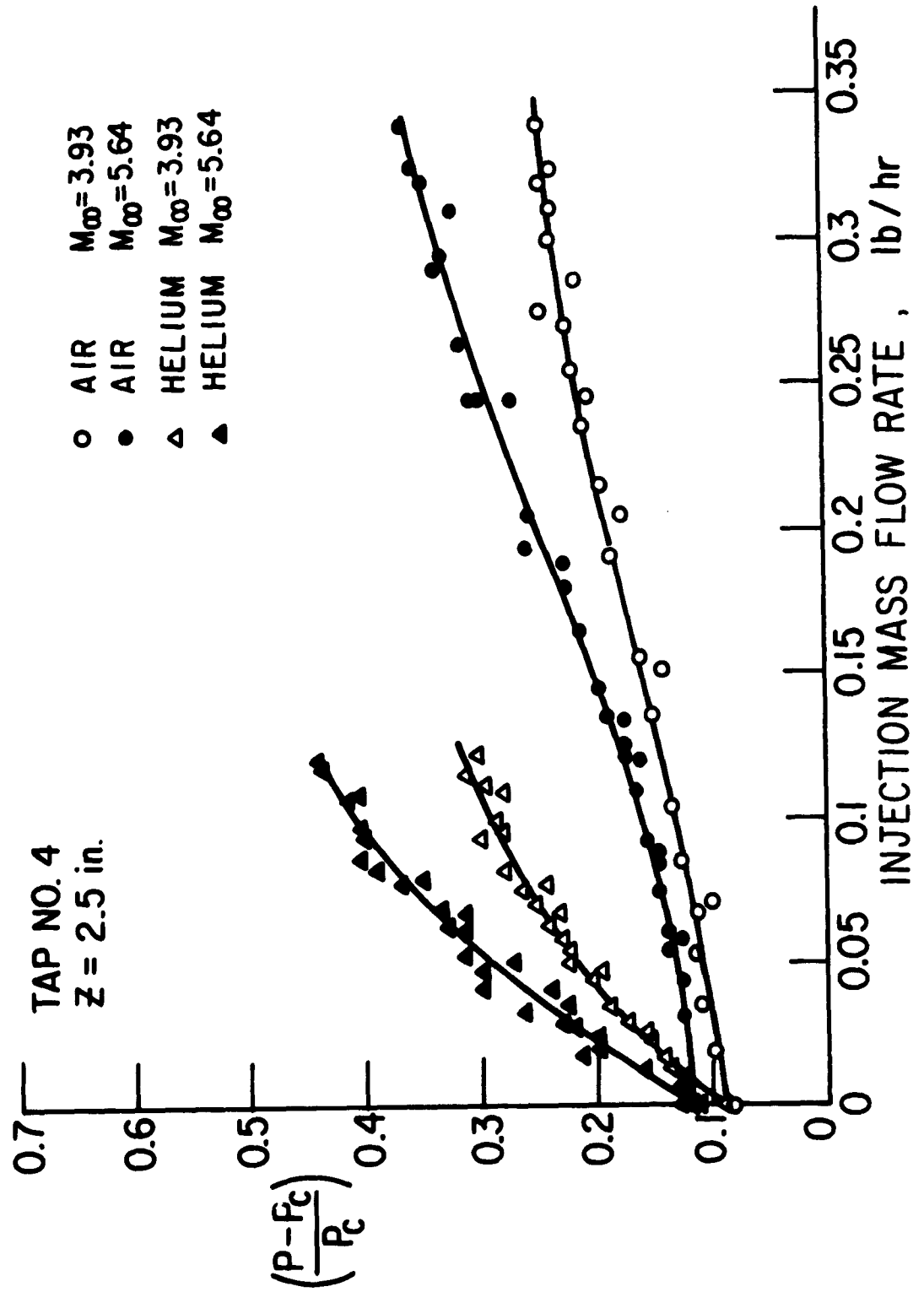


FIG. 14 INDUCED SURFACE PRESSURE AT TAP NO. 4

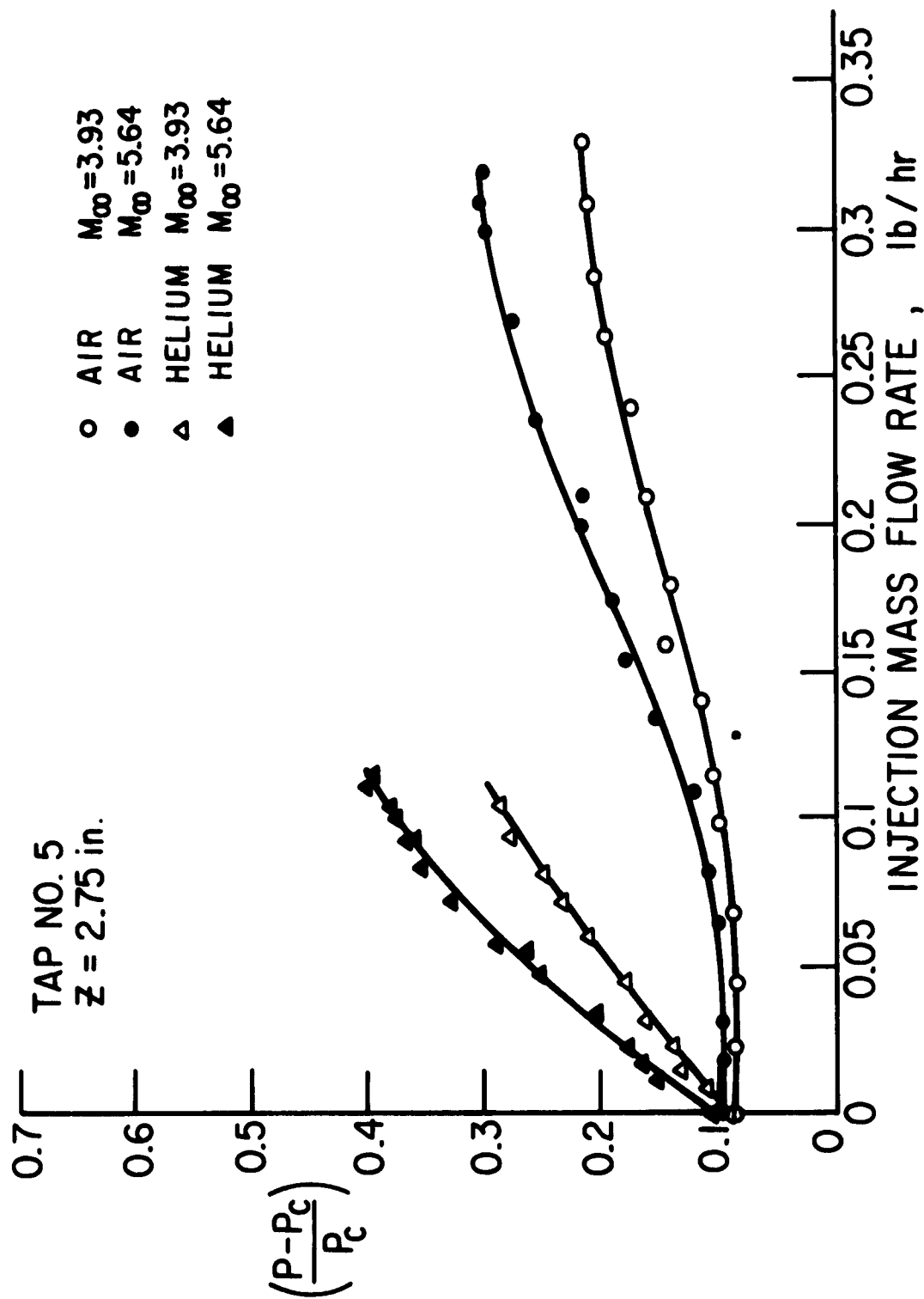


FIG. 15 INDUCED SURFACE PRESSURE AT TAP NO. 5

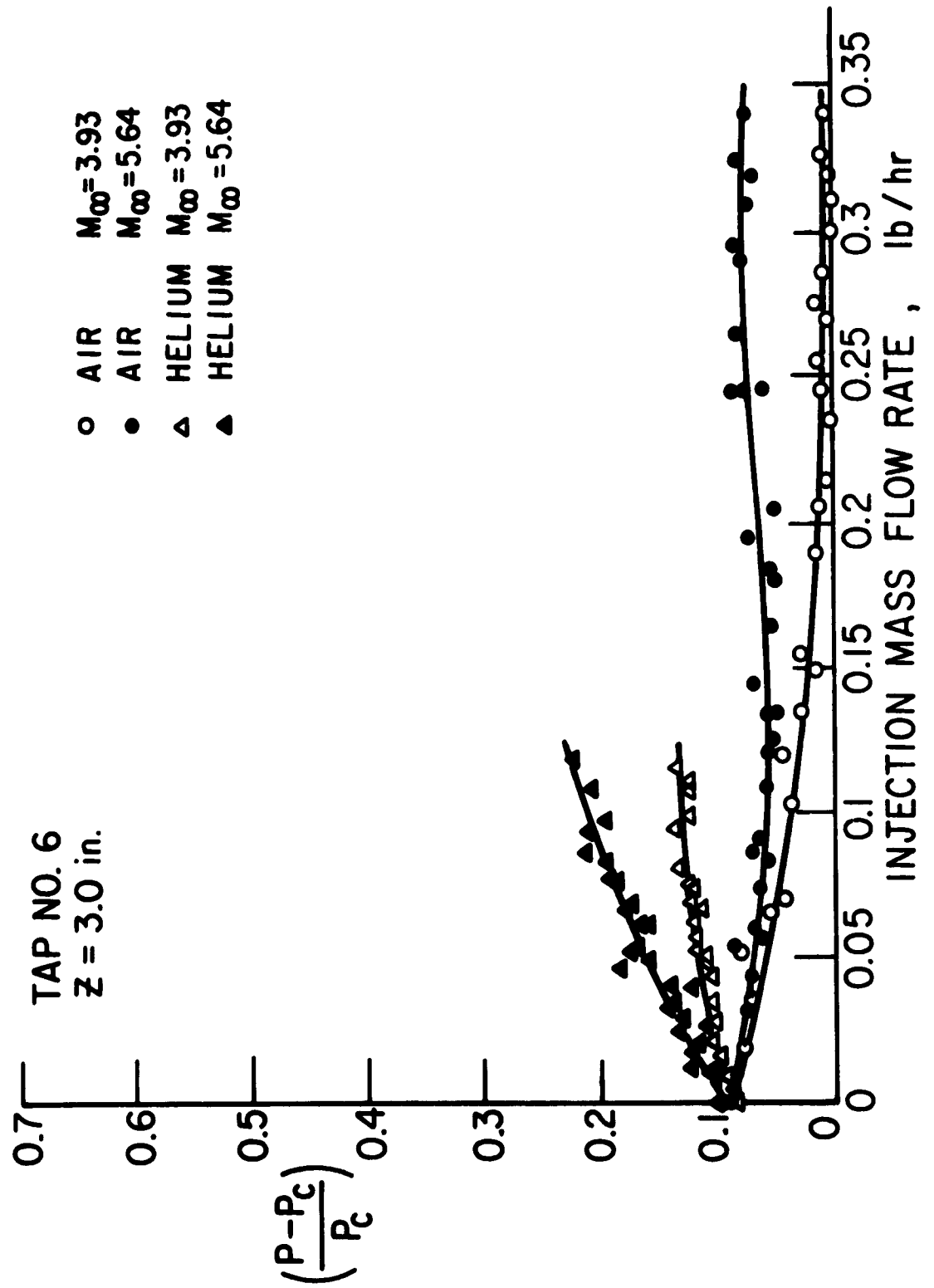


FIG. 16 INDUCED SURFACE PRESSURE AT TAP NO. 6

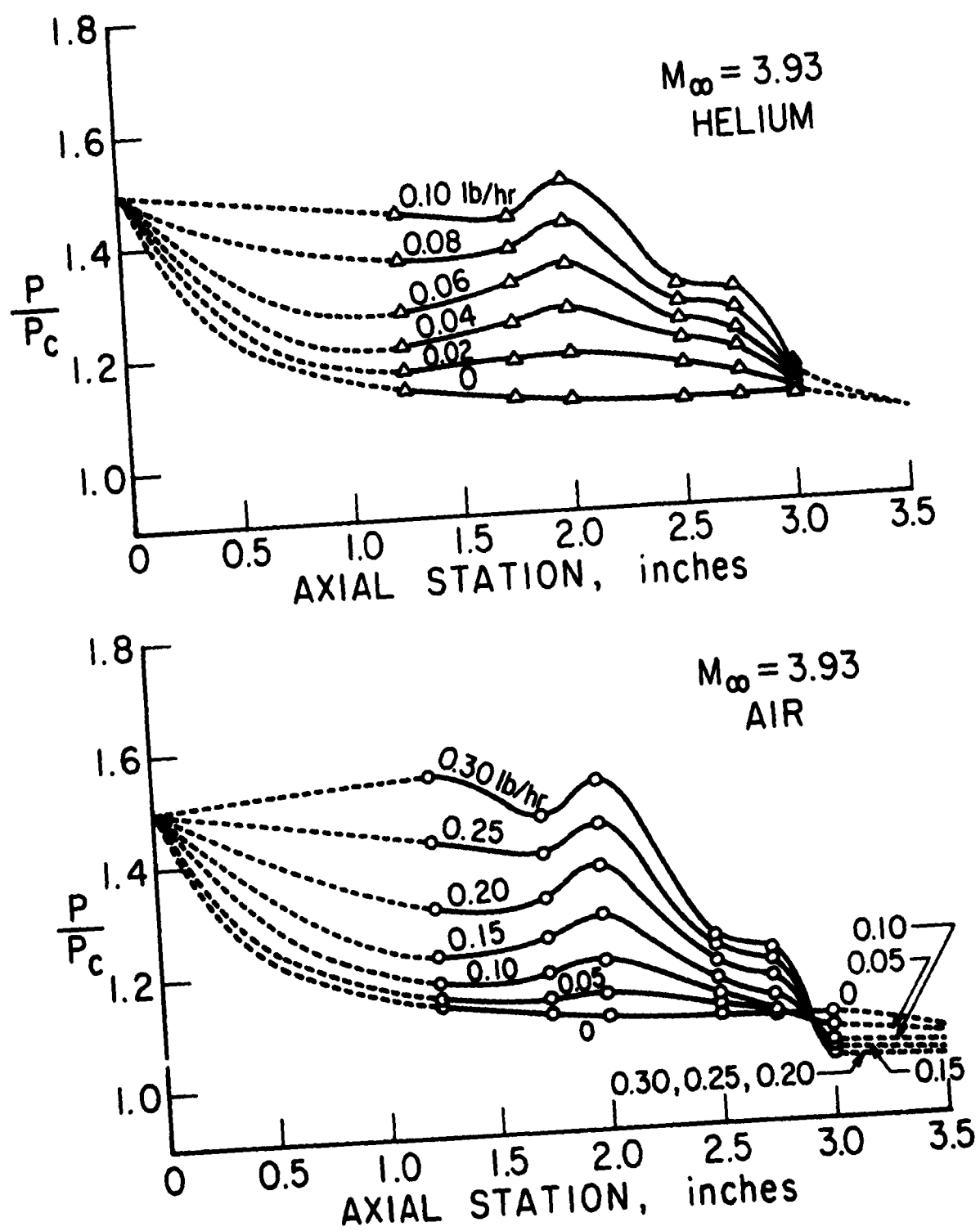


FIG. 17 CROSS-PLOTS OF SURFACE PRESSURE DATA

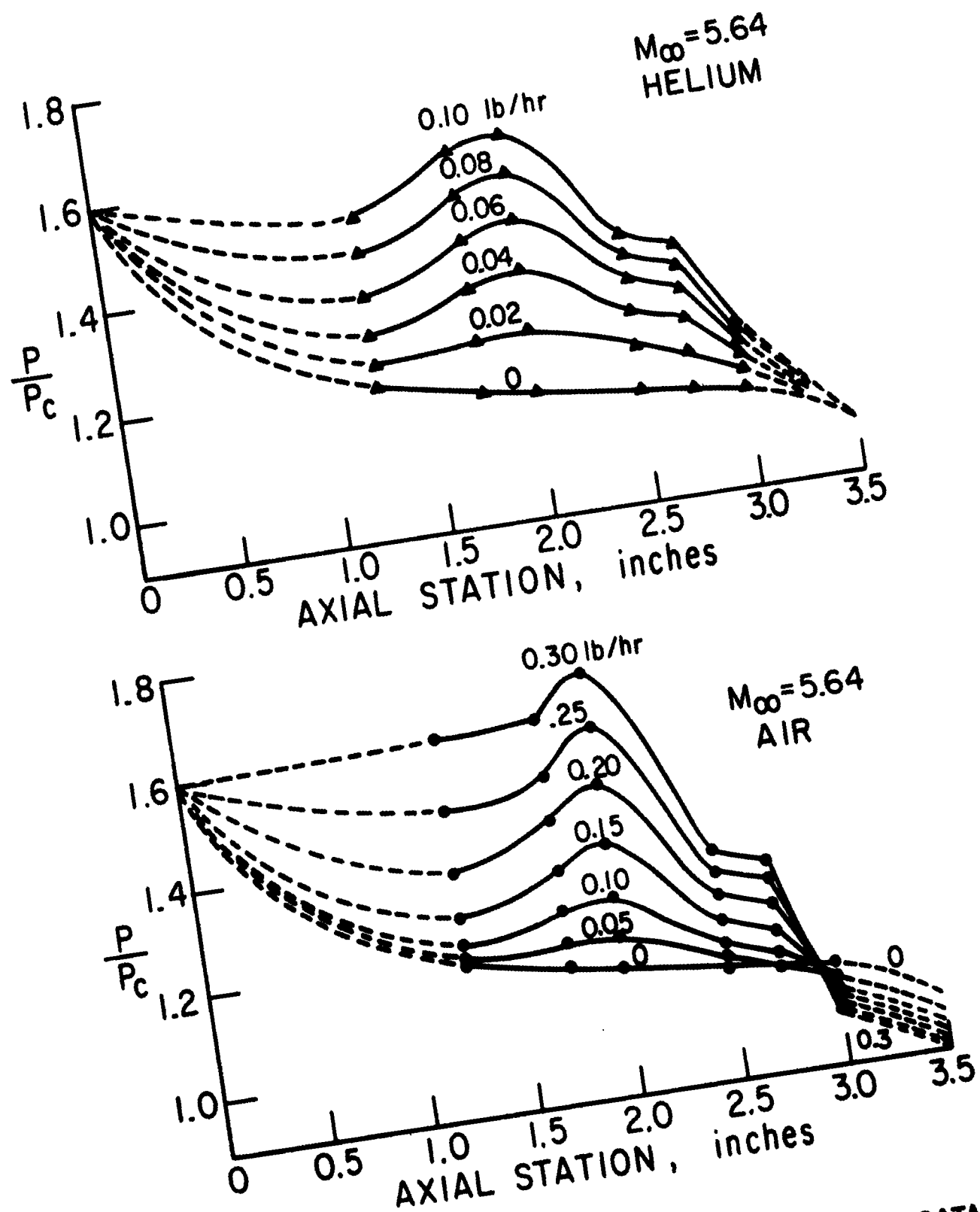


FIG. 18 CROSS-PLOTS OF SURFACE PRESSURE DATA

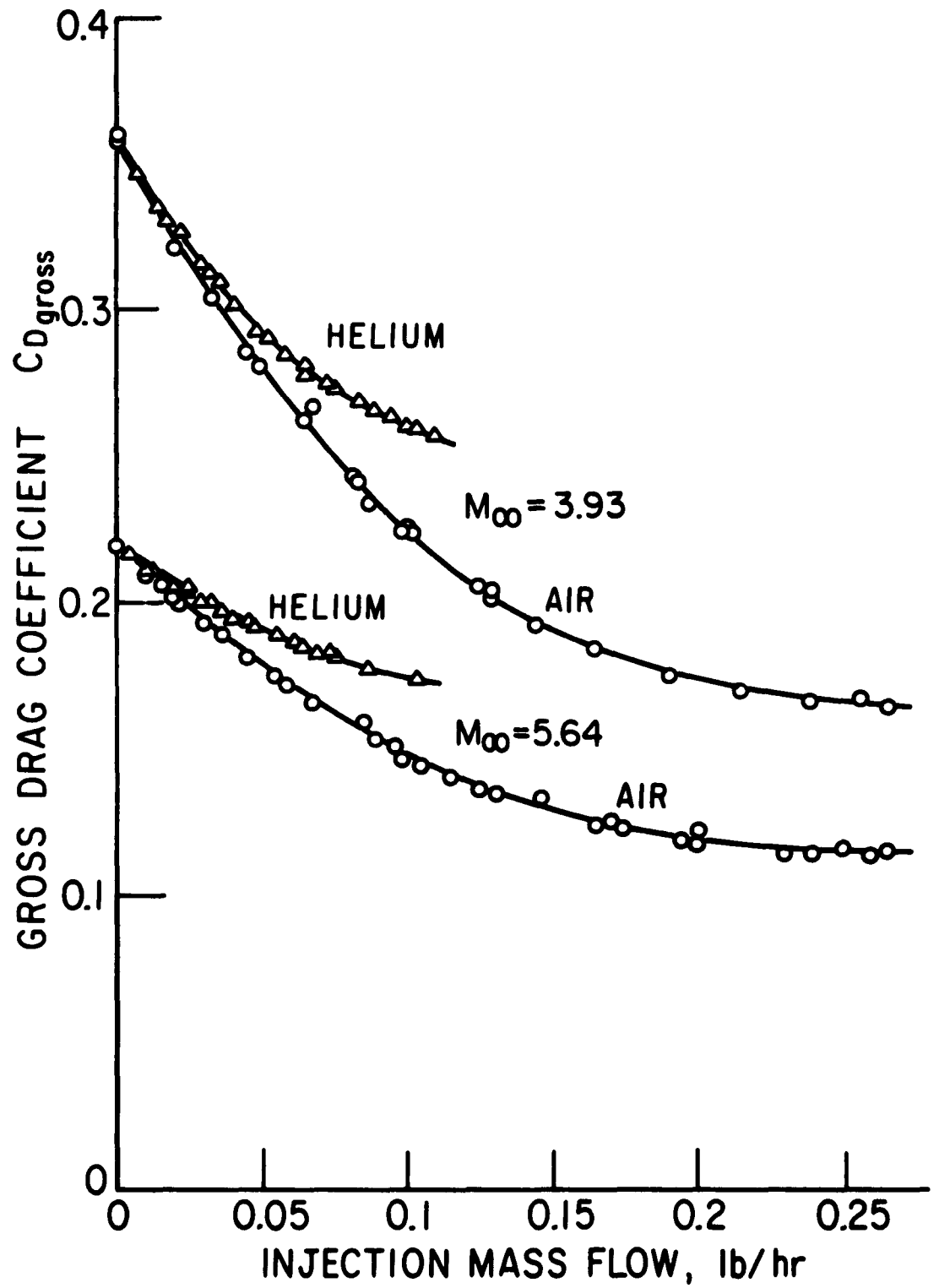


FIG.19 GROSS DRAG COEFFICIENT EXPERIMENTAL DATA

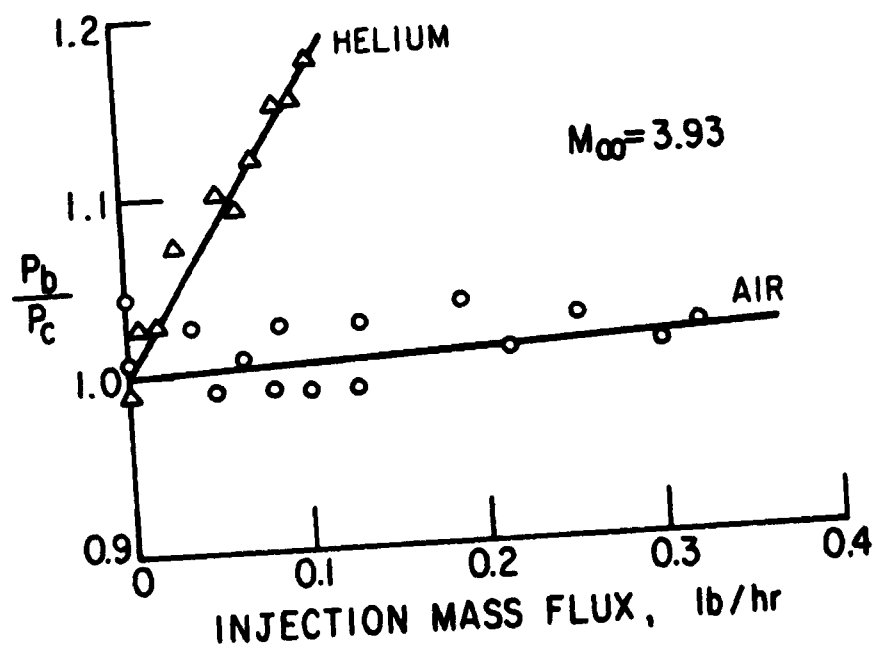
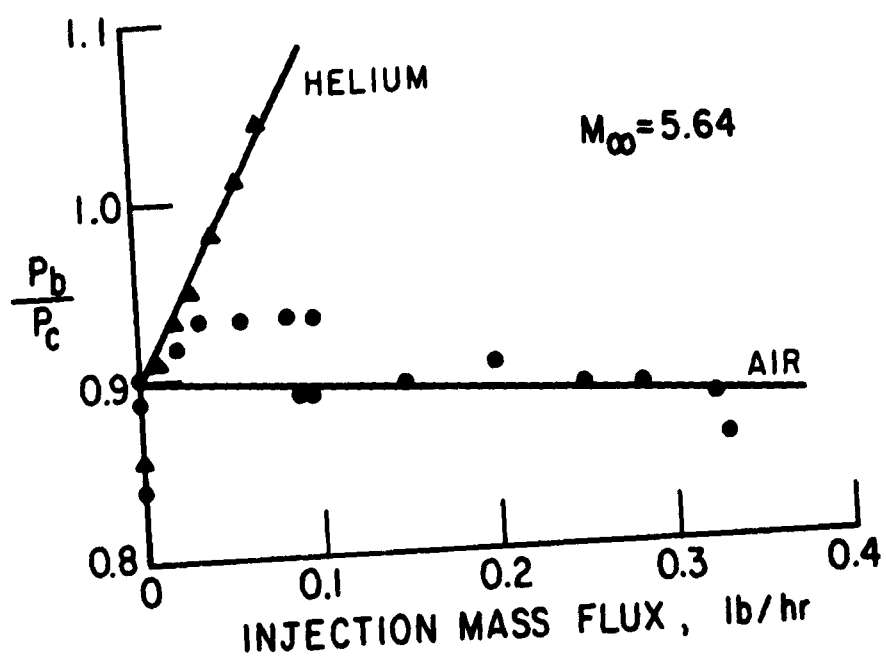


FIG. 20 BASE PRESSURE DATA TAKEN DURING THE FORCE DATA RUNS

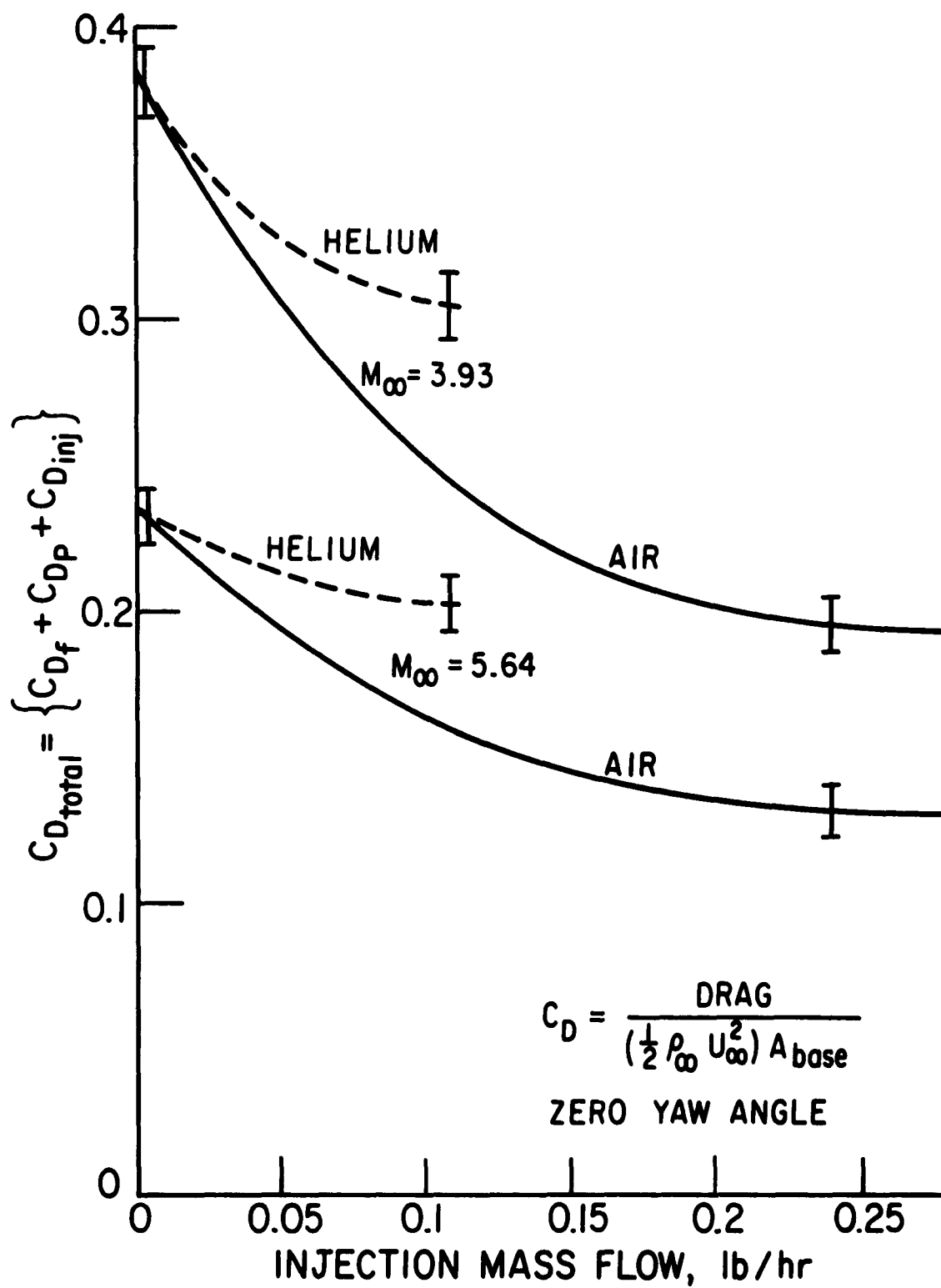


FIG. 21 FAIRED EXPERIMENTAL TOTAL DRAG DATA

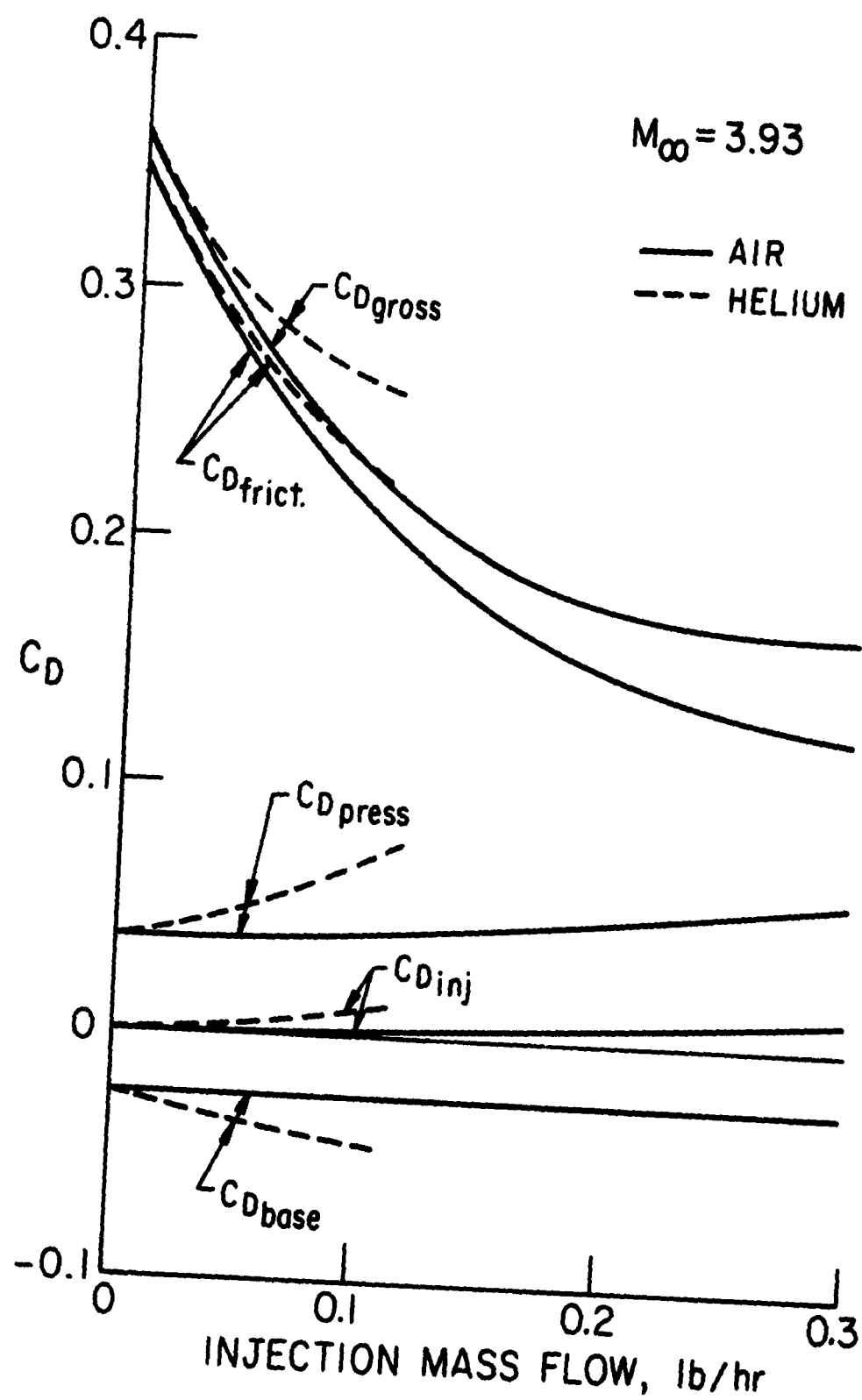


FIG. 22 DRAG CONTRIBUTIONS BASED ON EXPERIMENTAL DATA

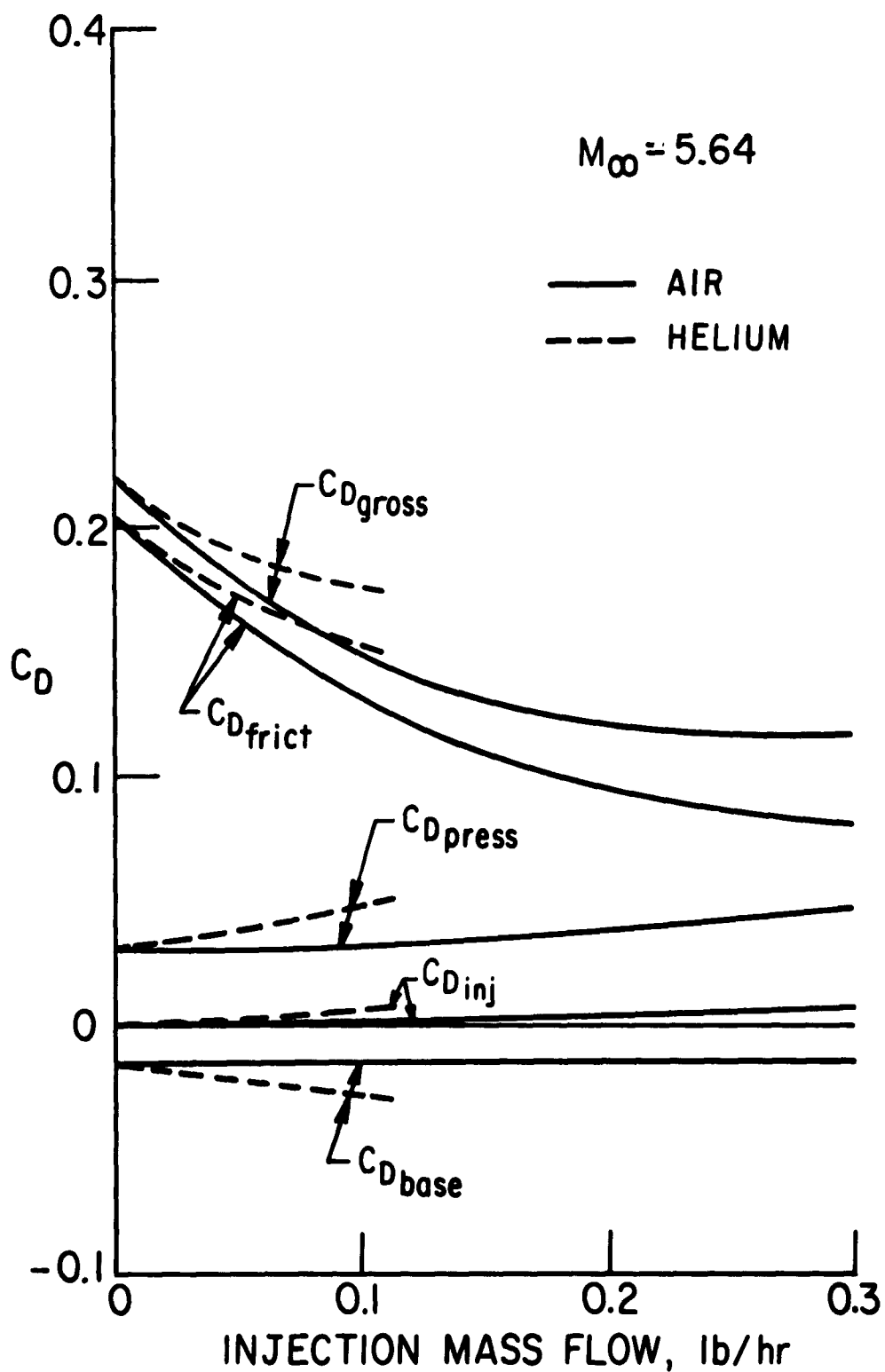


FIG. 23 DRAG CONTRIBUTIONS BASED ON EXPERIMENTAL DATA

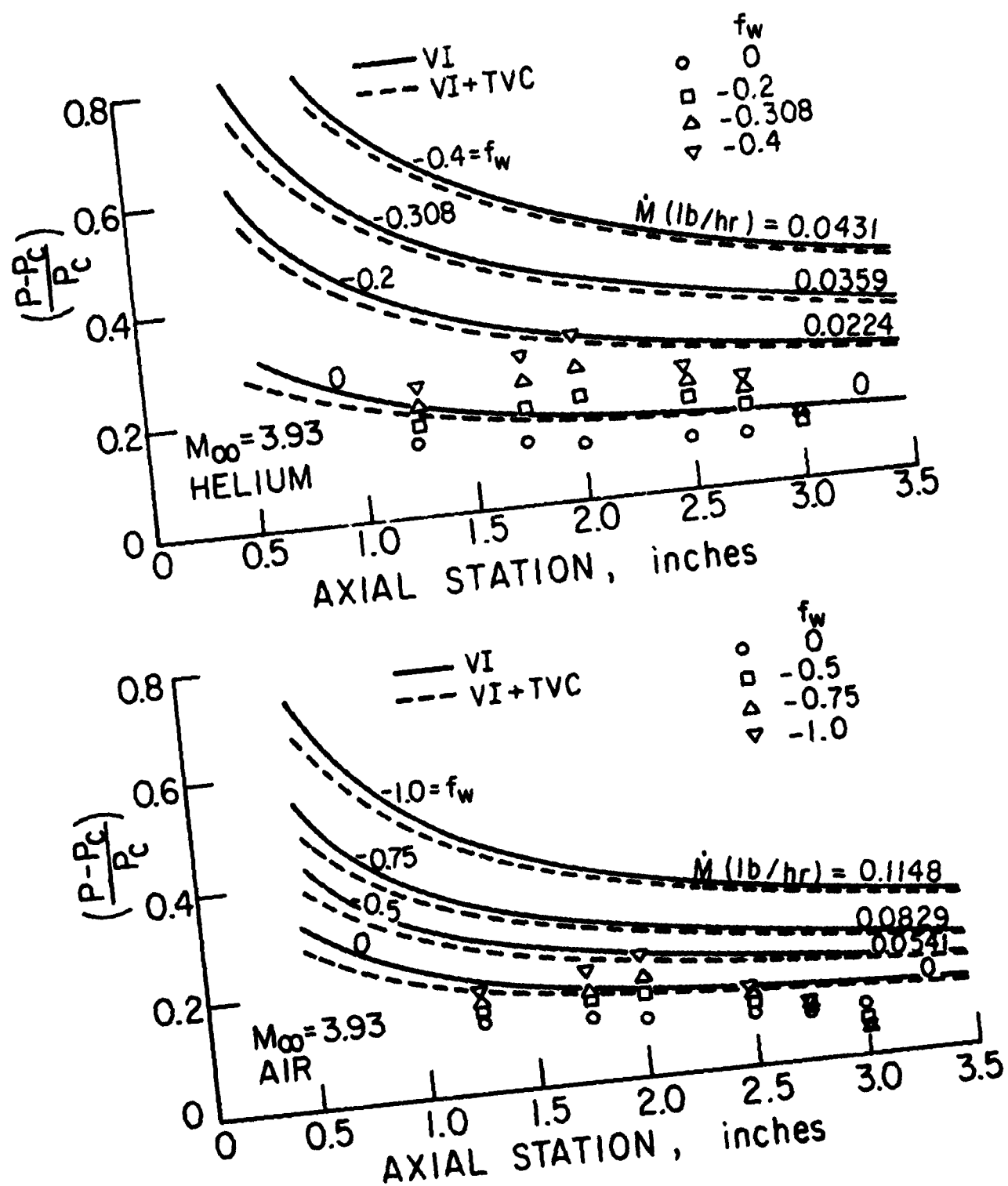


FIG. 24 COMPARISON OF MEASURED SELF-INDUCED PRESSURES WITH VALUES PREDICTED BY THE PRESENT THEORY

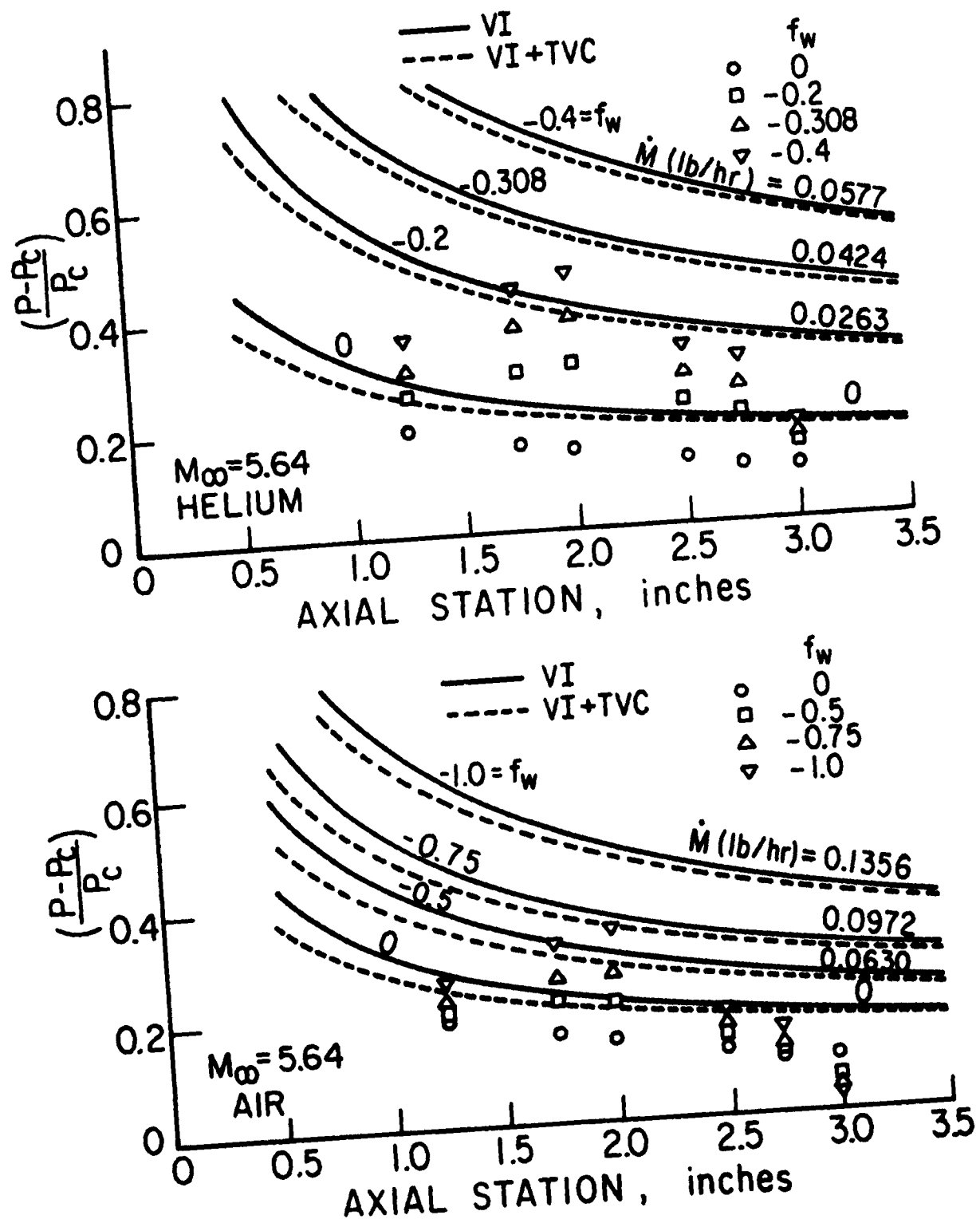


FIG. 25 COMPARISON OF MEASURED SELF-INDUCED PRESSURES WITH VALUES PREDICTED BY THE PRESENT THEORY

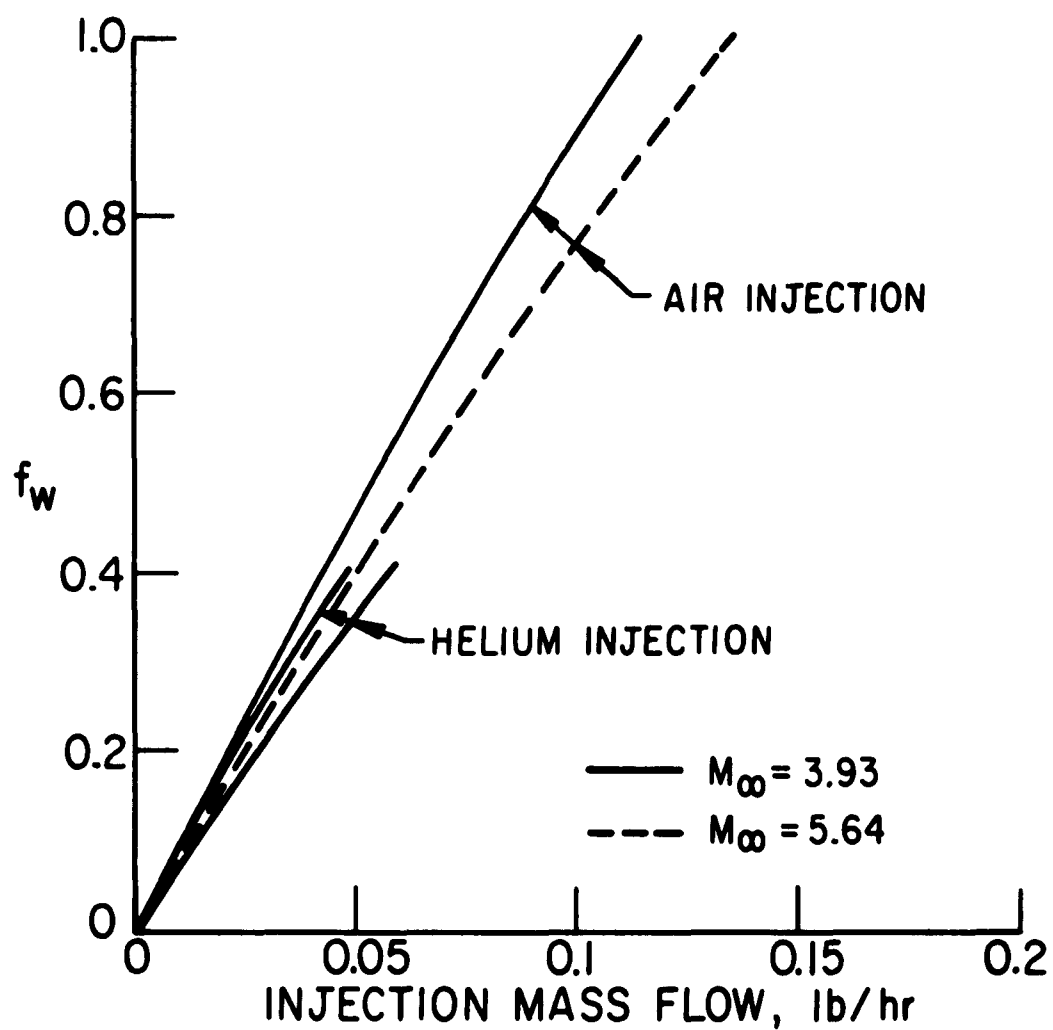


FIG. 26 RELATION BETWEEN INJECTION PARAMETER  $f_w$  AND THE TOTAL INJECTION RATE. (FROM PRESENT THEORY)

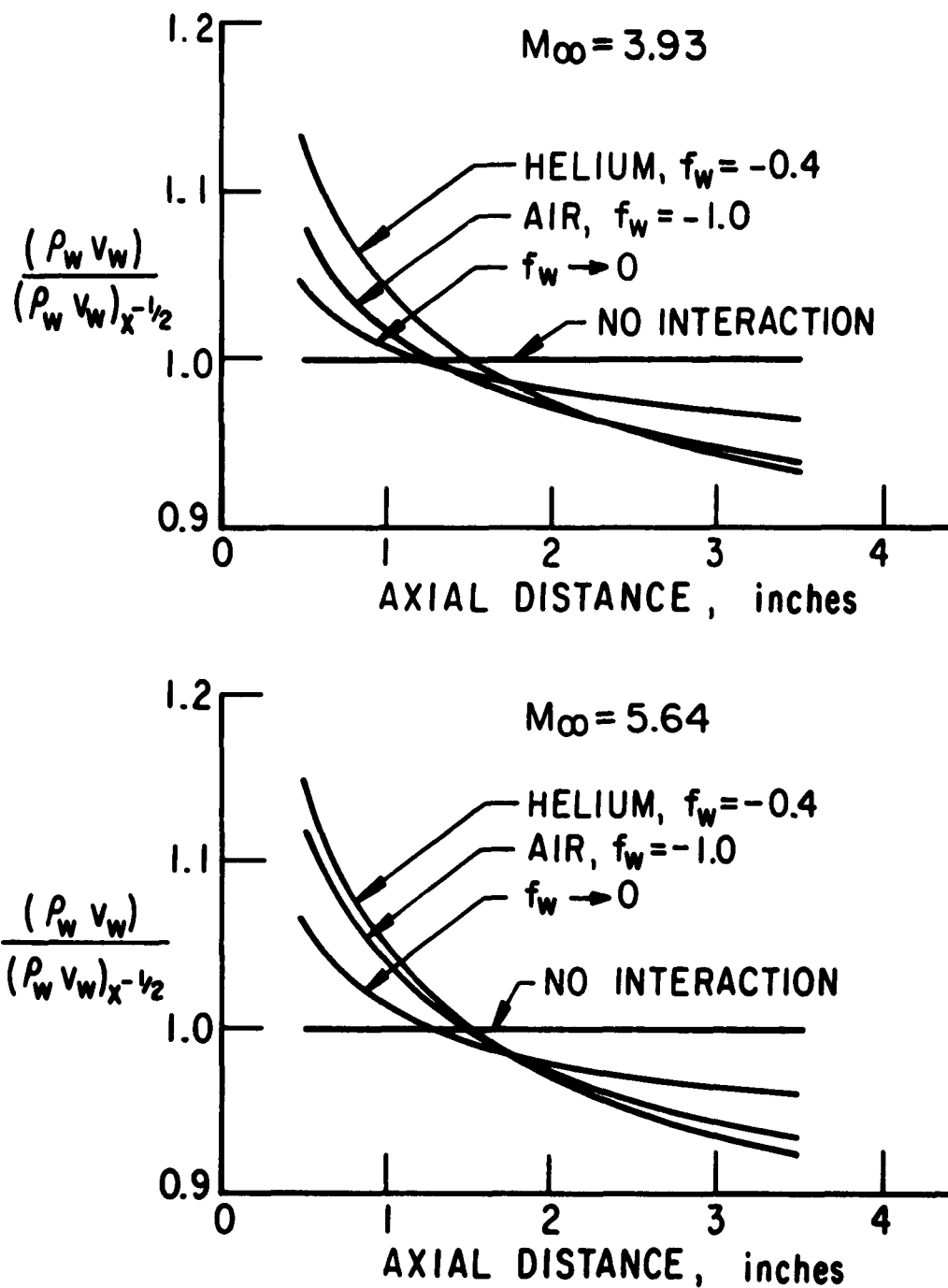


FIG. 27 THEORETICAL INFLUENCE OF VISCOUS INTERACTION ON THE INJECTION LAW FOR CONSTANT  $f_w$  PARAMETER

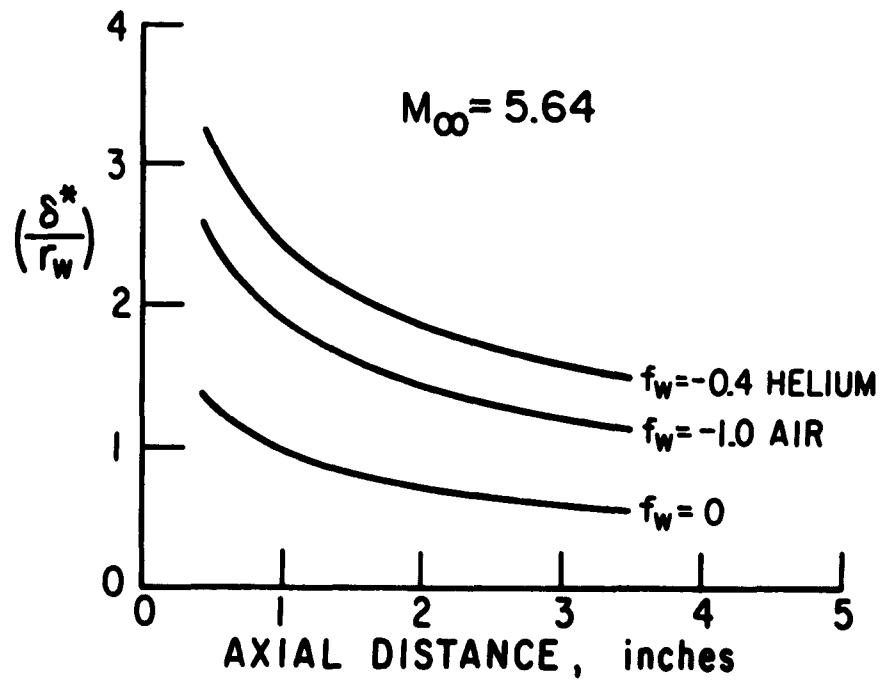
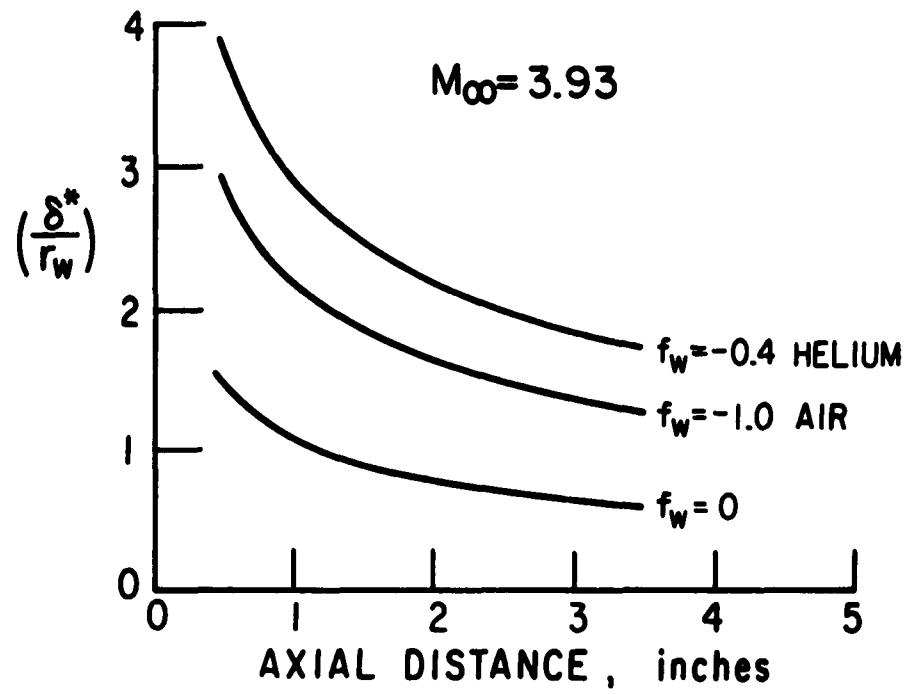


FIG. 28 DISPLACEMENT BOUNDARY LAYER THICKNESS FROM THE PRESENT THEORY

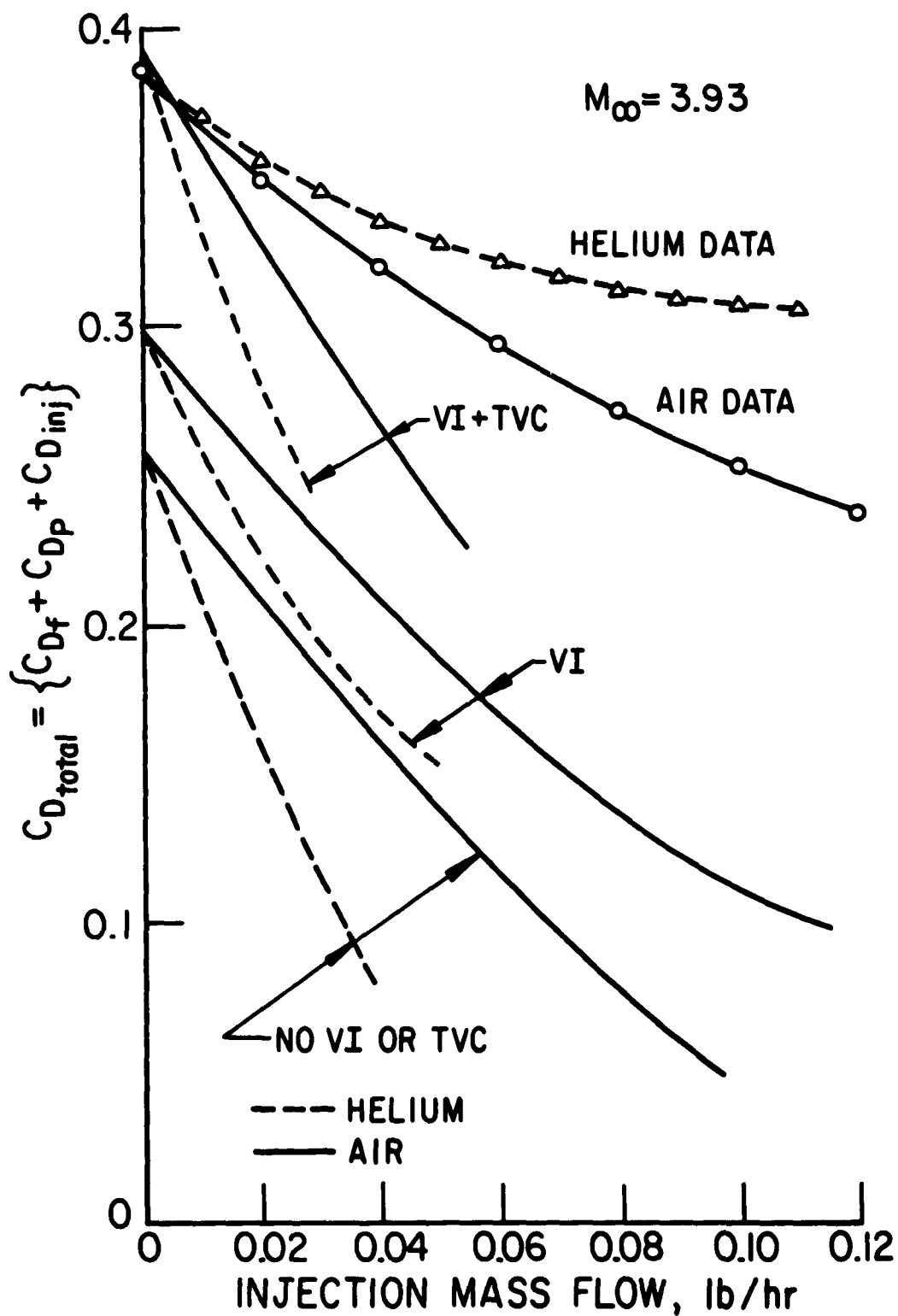


FIG. 29 EFFECT OF VISCOUS INTERACTION AND TRANSVERSE CURVATURE ON TOTAL DRAG ACCORDING TO THE PRESENT THEORY, AND COMPARISON WITH EXPERIMENTAL DATA.

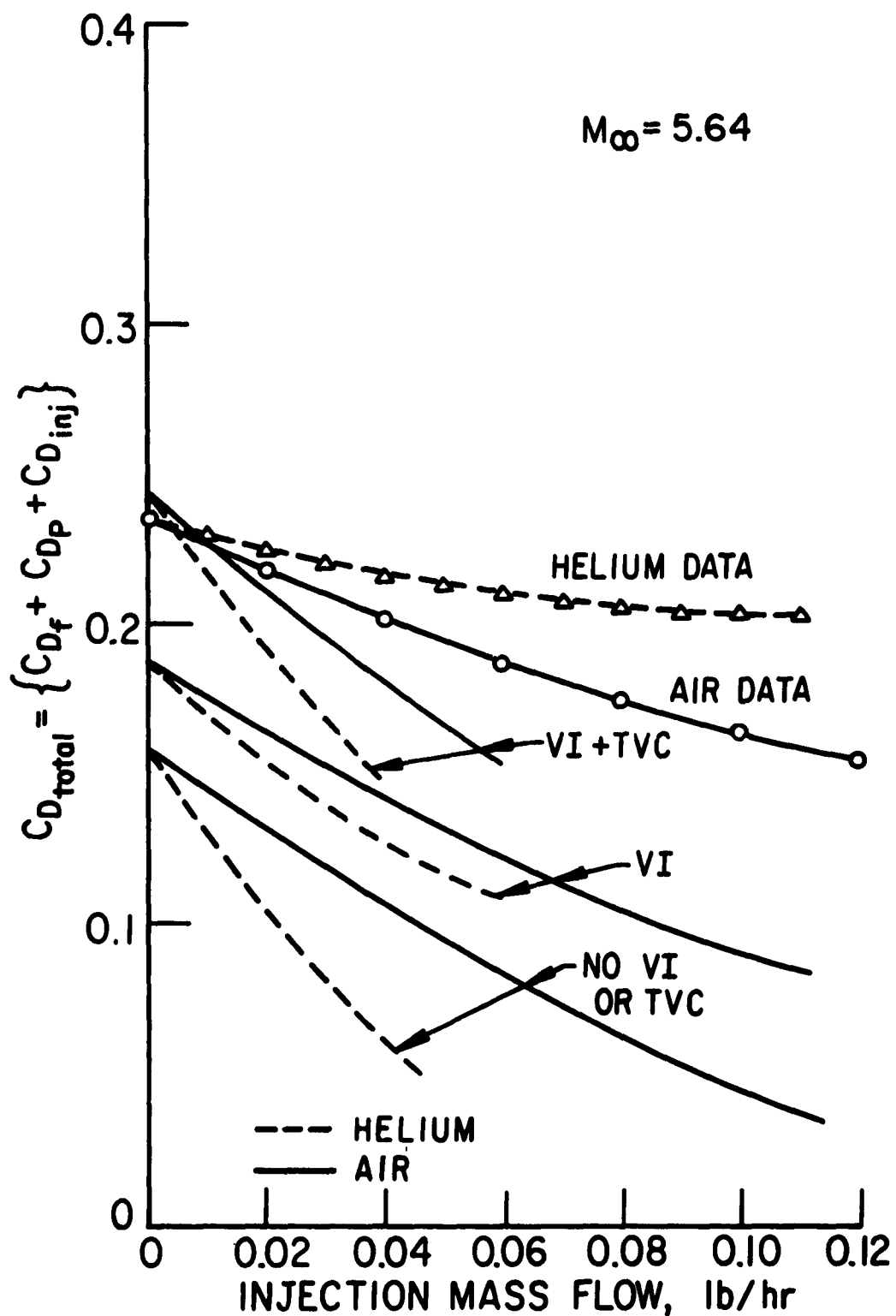


FIG. 30 EFFECT OF VISCOUS INTERACTION AND TRANSVERSE CURVATURE ON TOTAL DRAG ACCORDING TO THE PRESENT THEORY AND COMPARISON WITH EXPERIMENTAL DATA

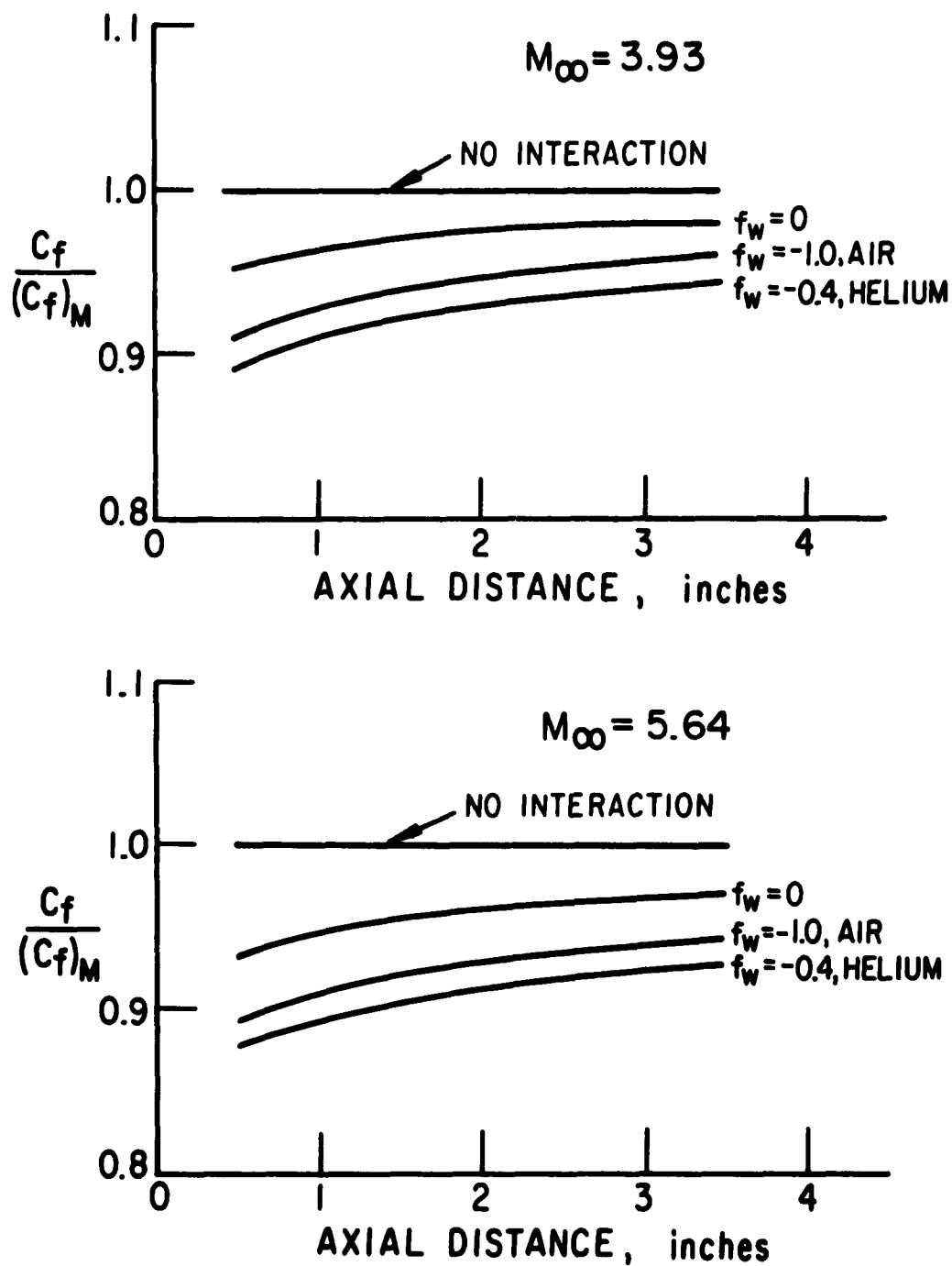


FIG. 31 EFFECT OF VISCOUS INTERACTION ON LOCAL SKIN FRICTION ACCORDING TO THE PRESENT THEORY

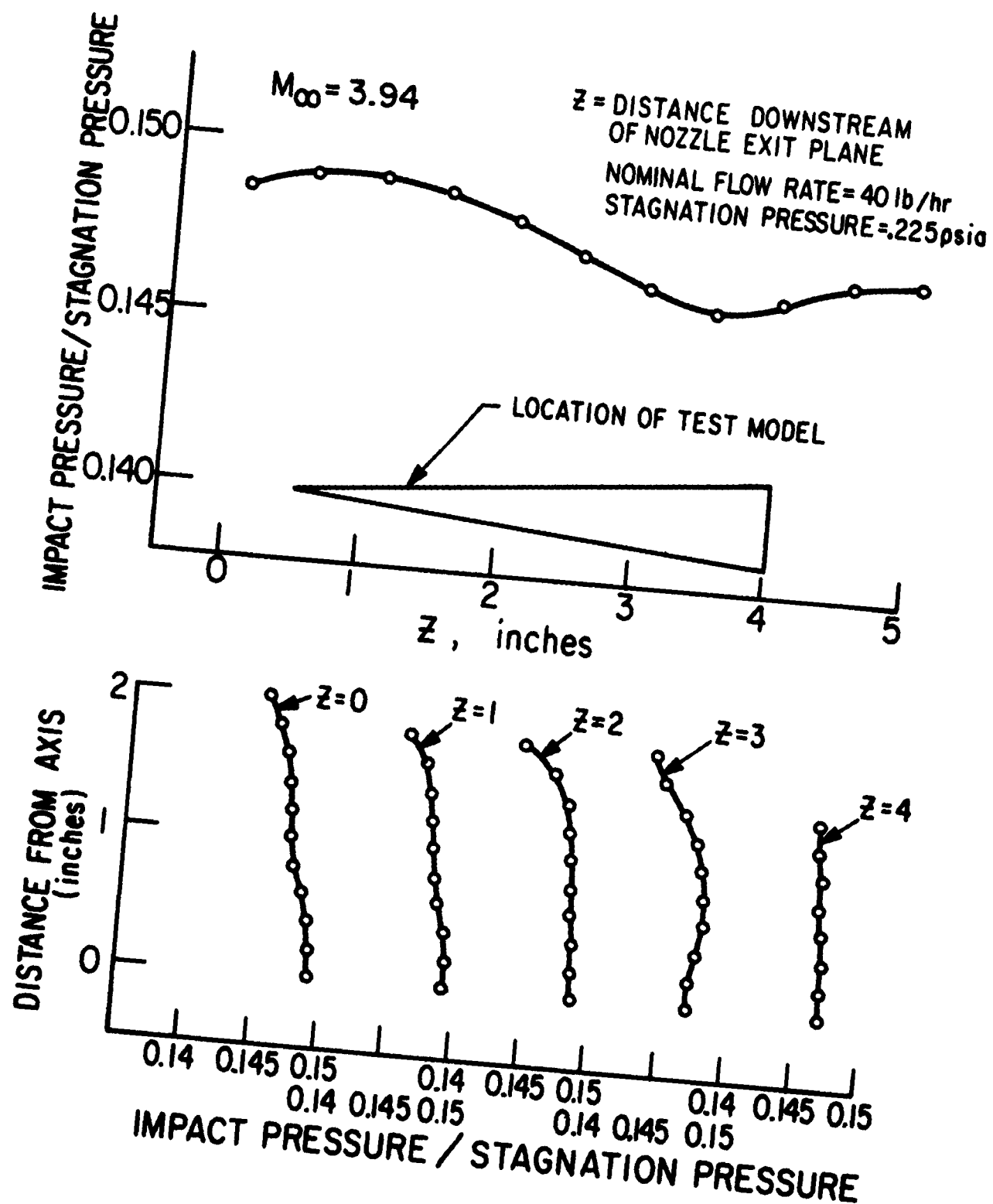


FIG. 32 IMPACT PRESSURE SURVEY FOR THE  
MACH 3.93 NOZZLE

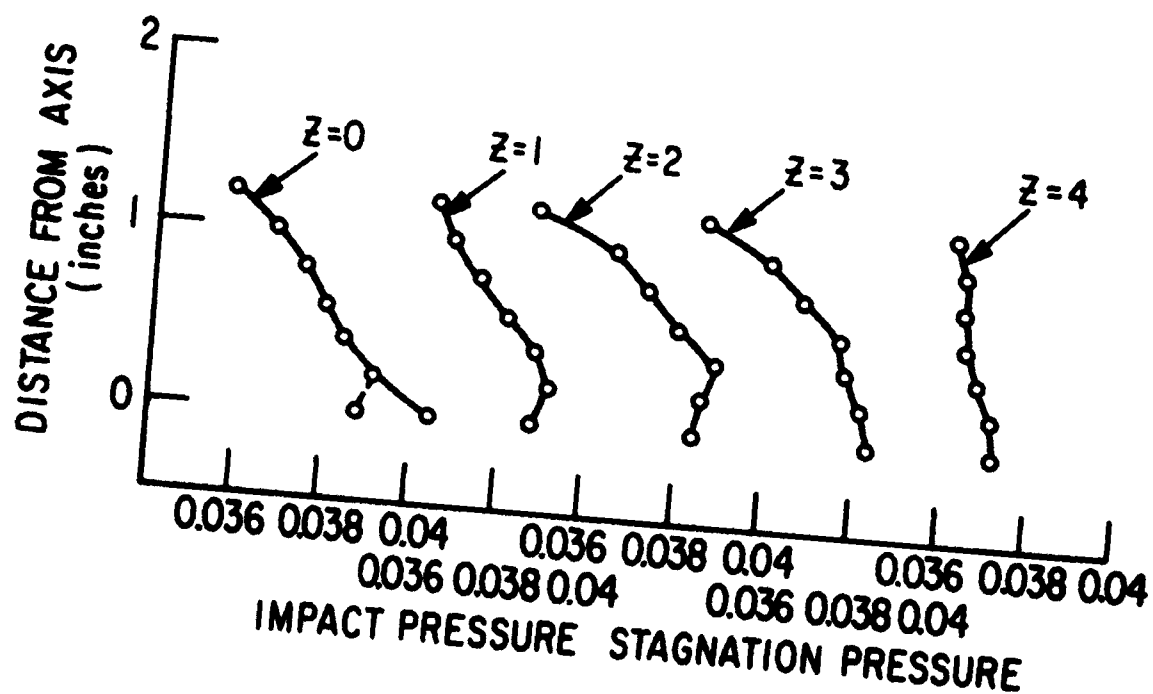
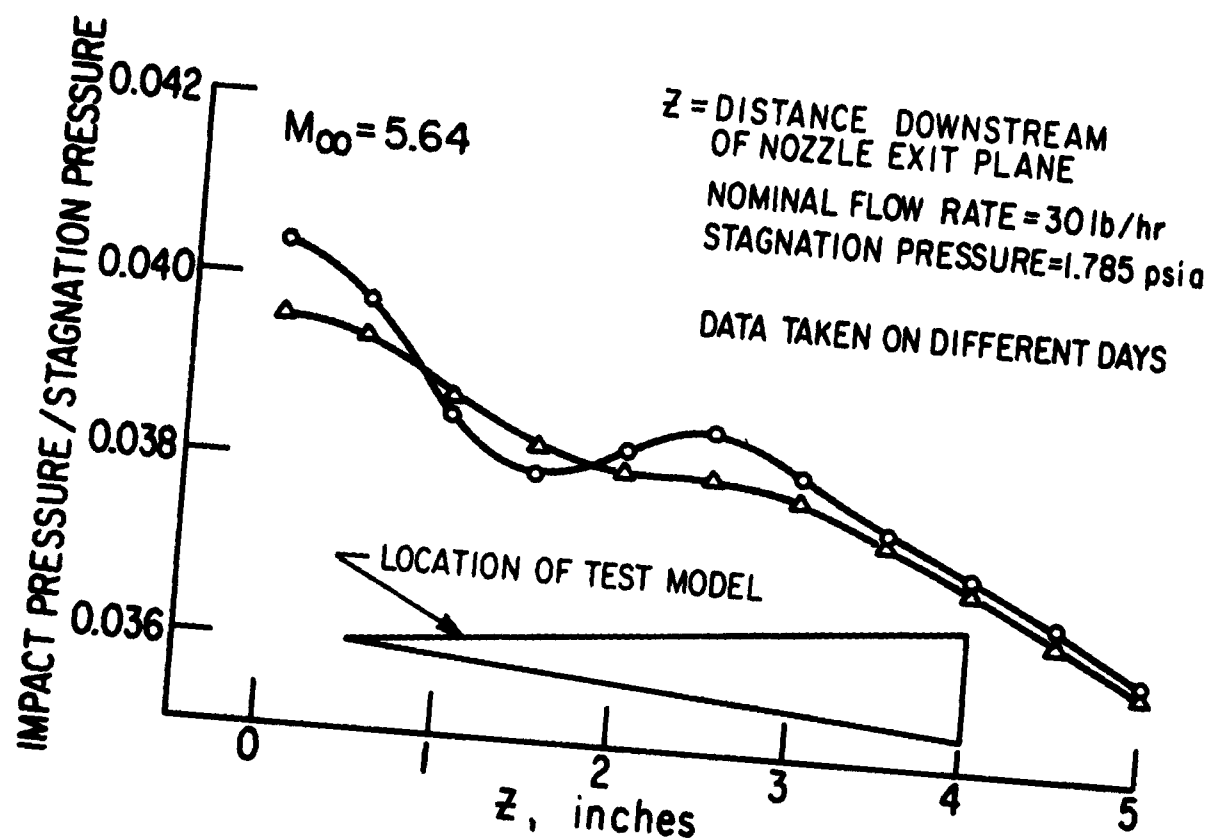


FIG. 33 IMPACT PRESSURE SURVEY FOR THE MACH 5.64 NOZZLE

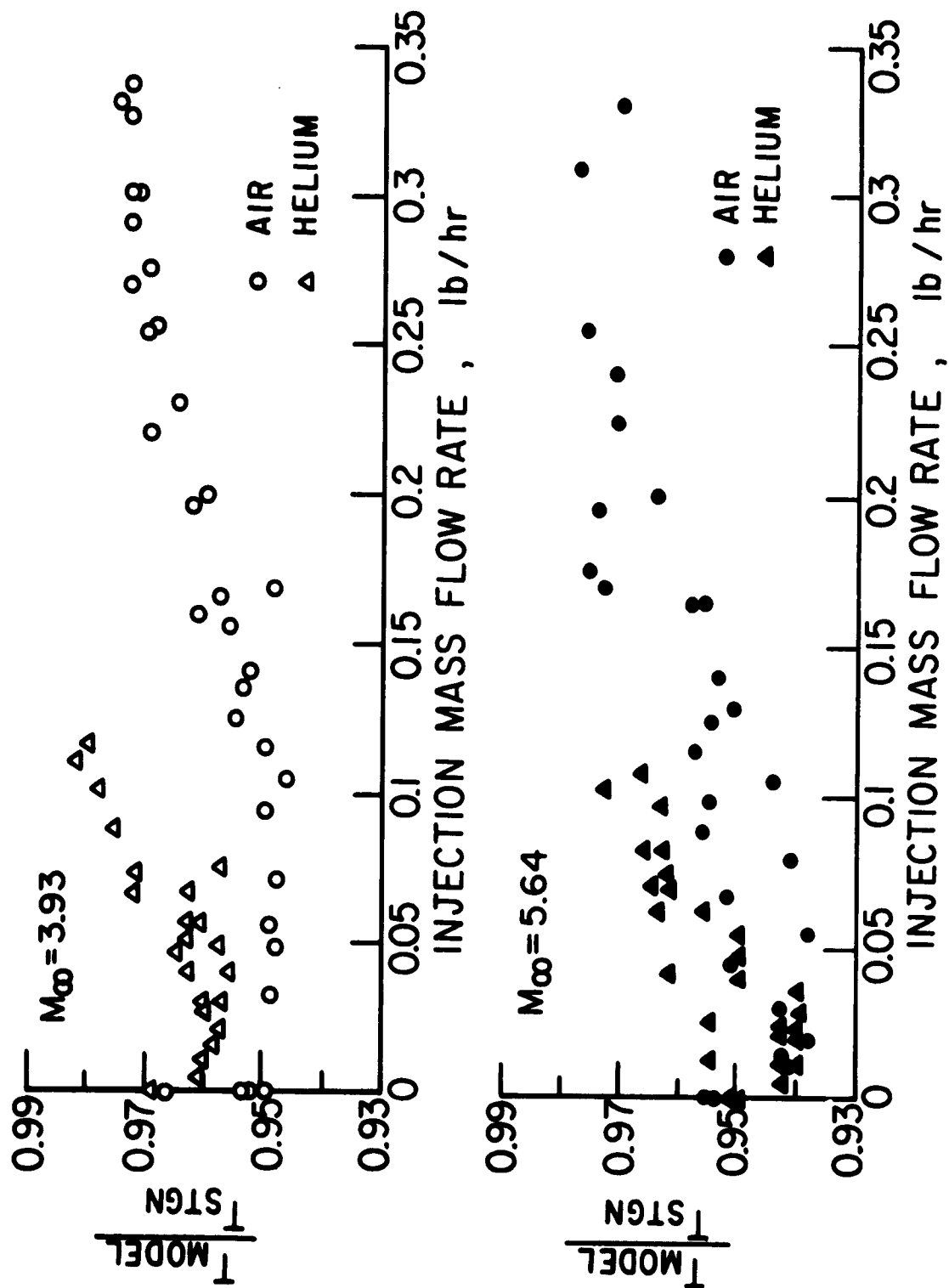


FIG. 34 TEST MODEL TEMPERATURES MEASURED AT THE CONE BASE

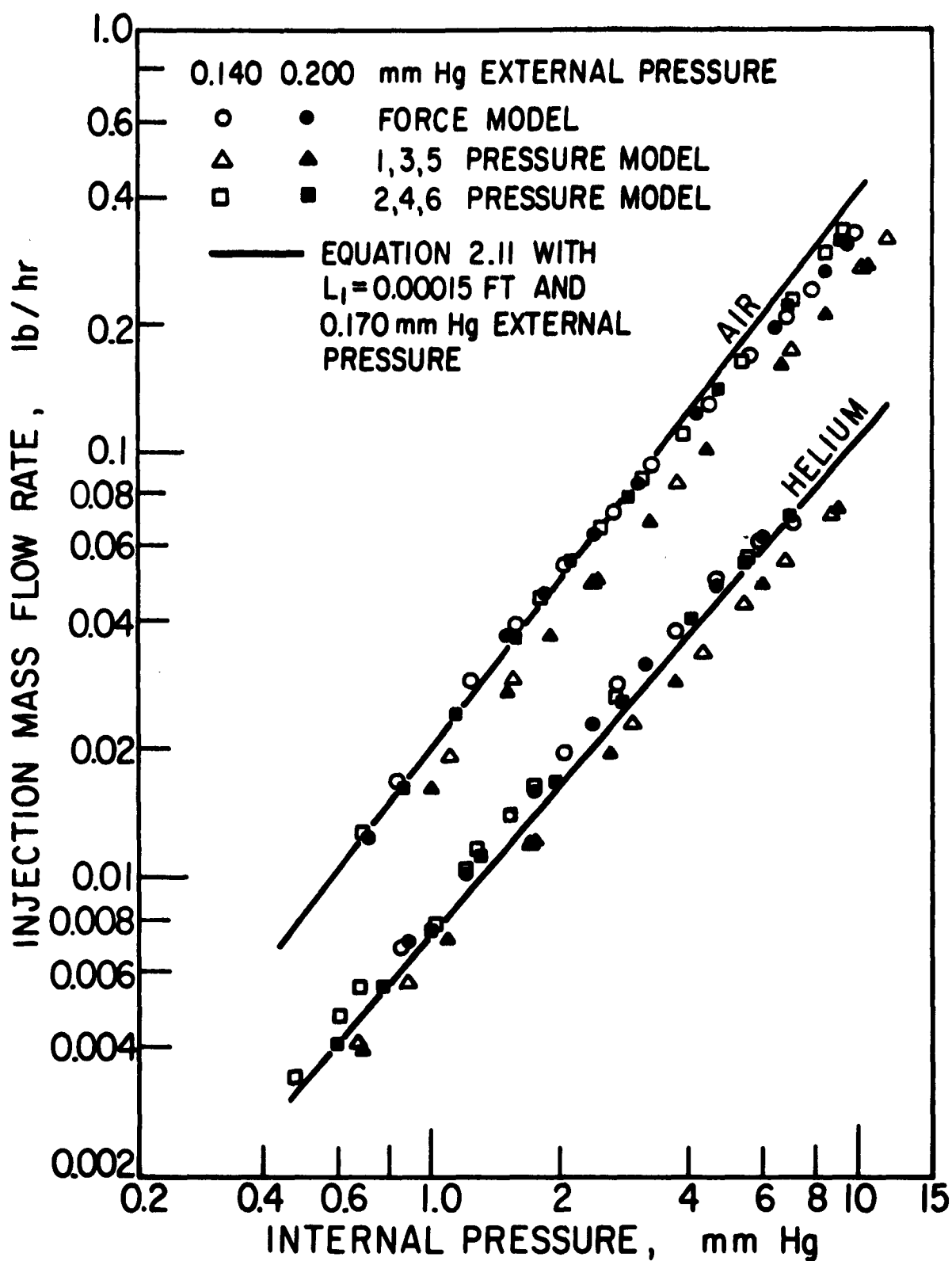


FIG.35 POROUS MODEL FLOW CHARACTERISTICS

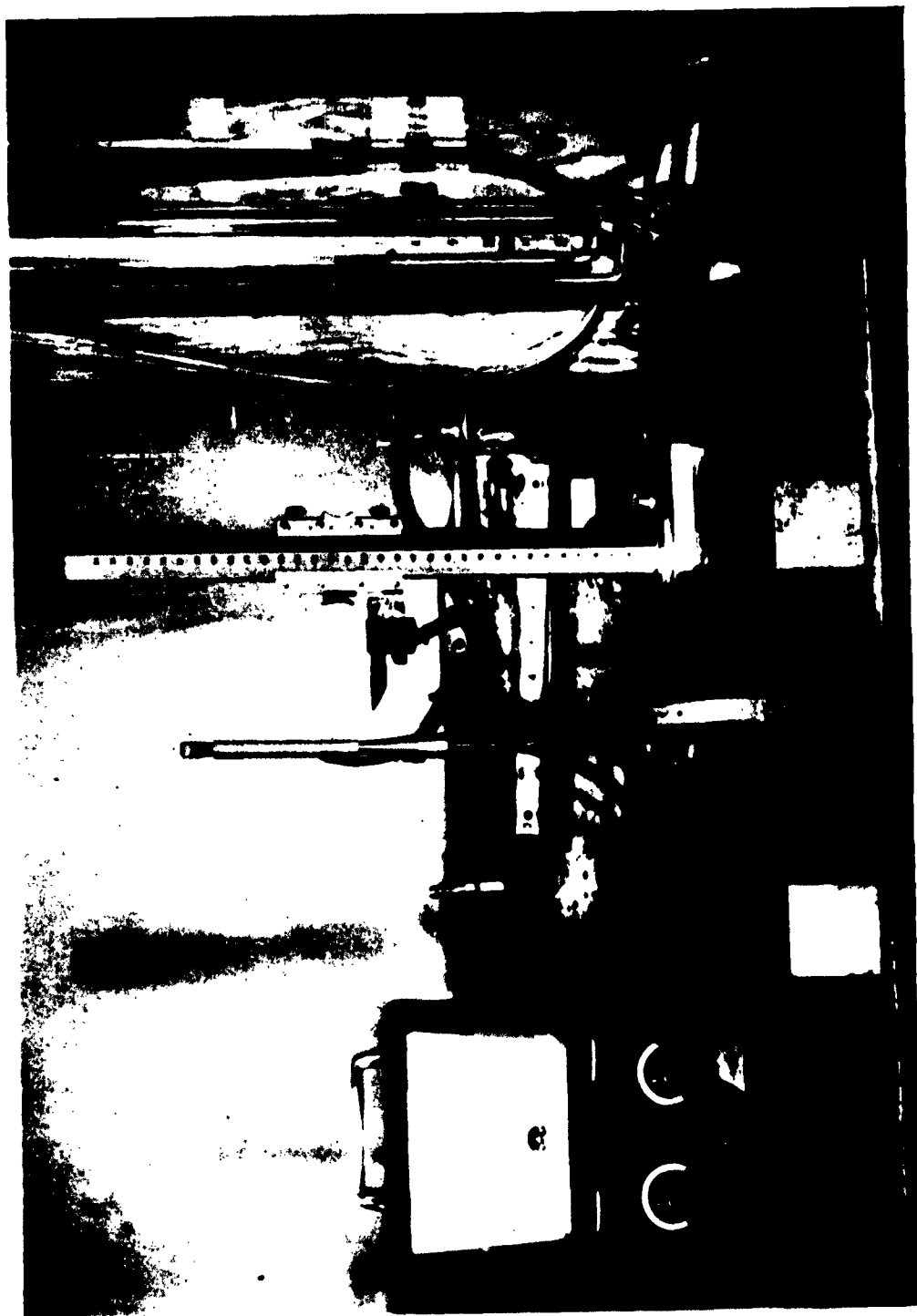


FIG. 36 DETERMINATION OF THE AXIAL INJECTION DISTRIBUTION

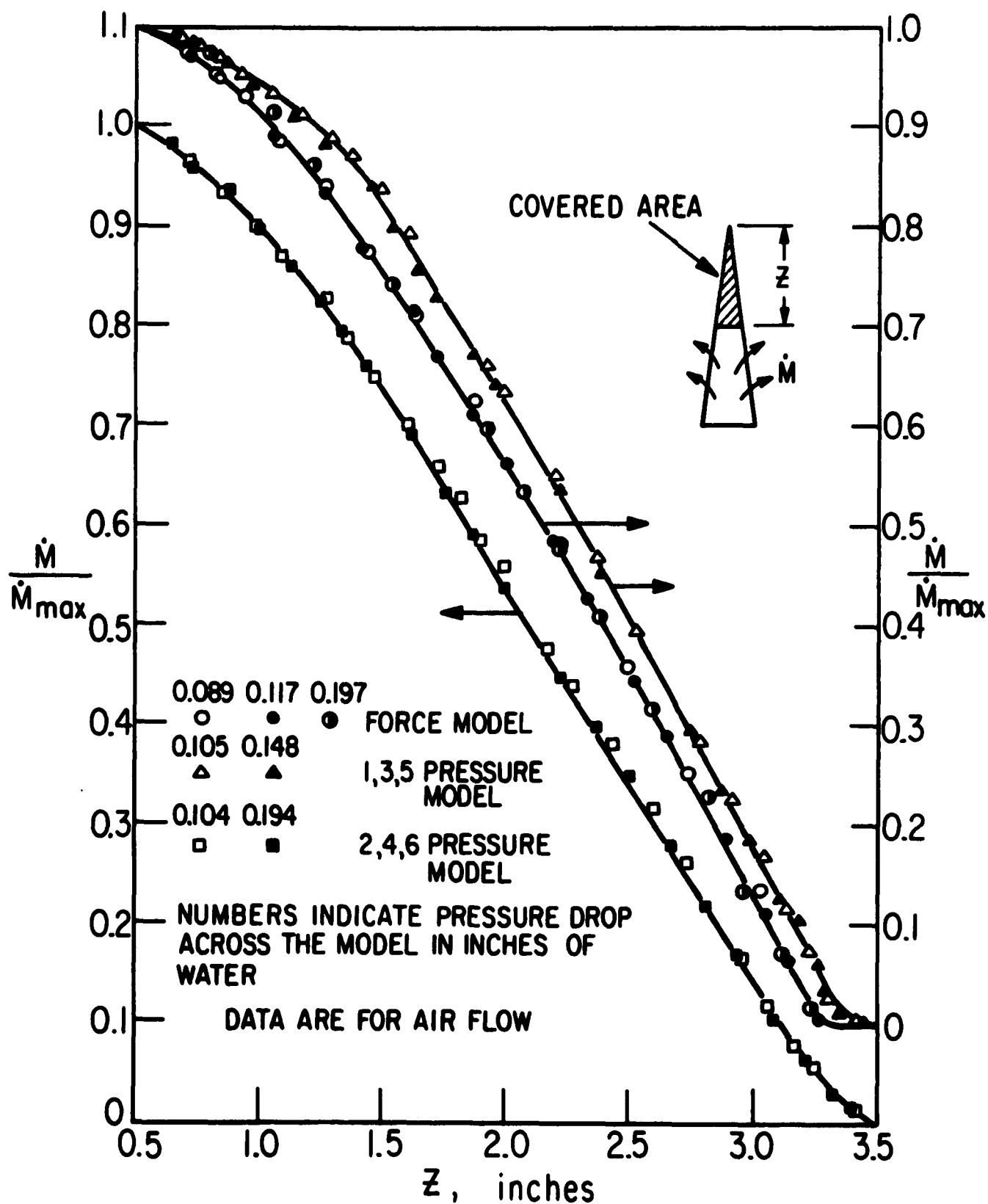


FIG. 37 DATA FOR THE DETERMINATION OF LOCAL MASS FLUX

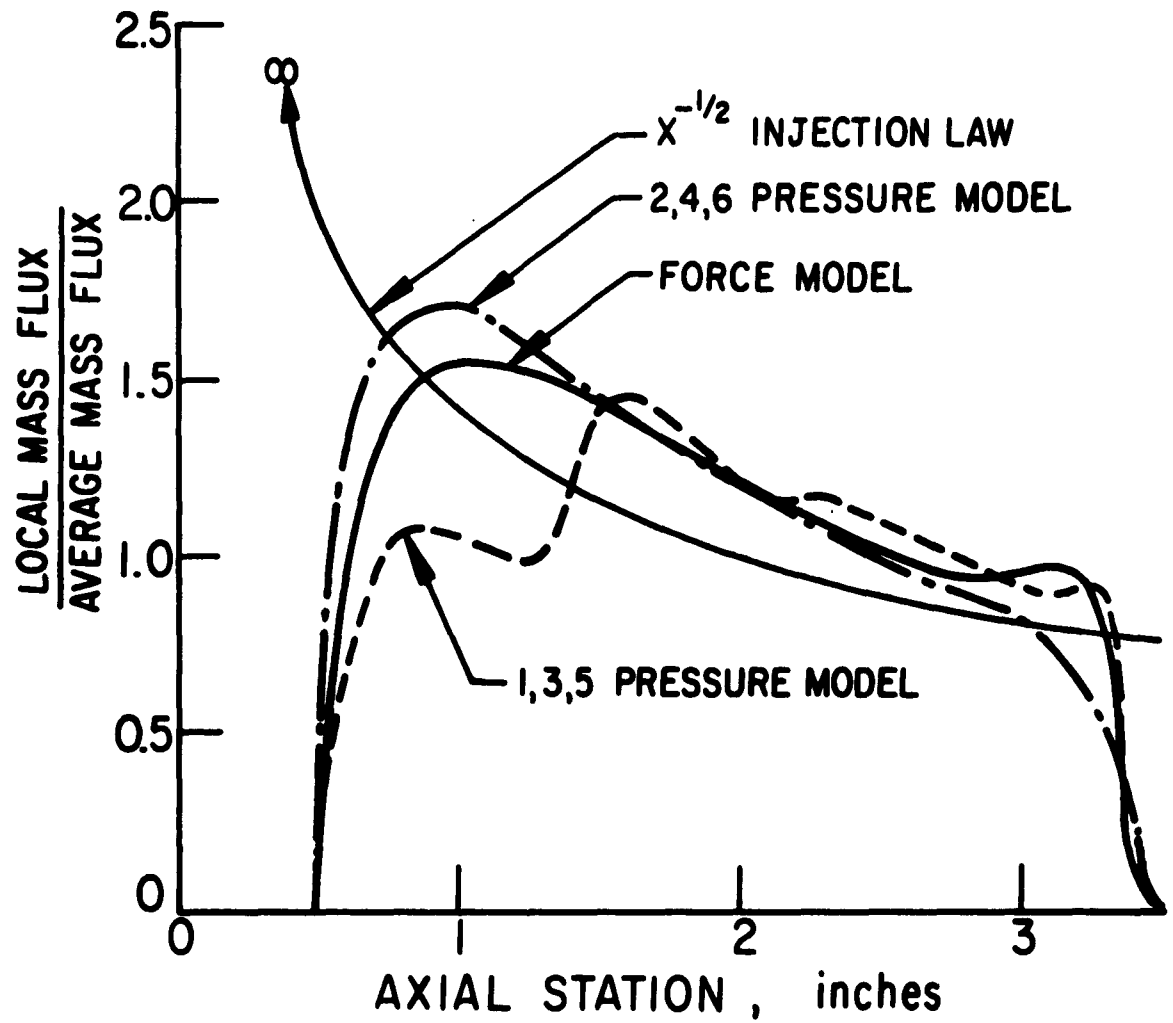


FIG. 38 APPROXIMATE LOCAL MASS FLUX DISTRIBUTION  
BASED ON DATA PRESENTED IN FIG. 37

## PAGE 1.

Chief of Naval Research Department of the Navy Washington 25, D. C. Attn: Code 436 419 421 401	(3) (1) (1) (1)	Dr. L. L. Stokastovich, Chief Gas Dynamics Facility ARD, Incorporated Arnold Air Force Station Tennessee N6 AFLE (OCEER) Wright-Patterson Air Force Base Ohio	(1) (1) (1) (1)	Dr. M. Abele General Applied Science Lab, Inc. Westbury, Long Island, New York Professor J. D. Ahernan Institute of Technology University of Minnesota Minneapolis 14, Minnesota Professor V. Blockner Palmer Physical Laboratory Princeton University Princeton, New Jersey Mr. Wallace F. Davis, President VSPA, Incorporated 2424 Monover Street Palo Alto, California Mr. E. L. Dumas, Jr. Assistant Mgr., Engineering and Sciences Extension University of California 3451 Bancroft Way Berkeley 4, California	(1) (1) (1) (1) (1)	Professor Leslie Division of Engineering Brown University Providence 12, Rhode Island Professor Mader Division of Engineering Brown University Providence 12, Rhode Island Professor S. S. Fanner Engineering Division California Institute of Technology Pasadena 4, California Jet Propulsion Laboratory 4800 Oak Grove Drive Pasadena, California Attn: Library	(1) (1) (1) (1)
Commanding Officer Office of Naval Research Branch Office 491 Summer Street Boston 10, Massachusetts	(1)	Commander Wright Air Development Command Wright-Patterson Air Force Base Ohio Attn: Library ASD (ASDWP-1) Wright-Patterson Air Force Base Ohio ARL (ASD) Building 450 Wright-Patterson Air Force Base Ohio	(1) (1) (1) (1)	Professor S. L. Van Goshan Department of Aeronautical and Astronautical Engineering Ohio State University 3036 Neil Avenue Columbus 10, Ohio Professor Antonio Perri Aerodynamics Laboratory Polytechnic Institute of Brooklyn 537 Atlantic Avenue Brooklyn, New York Professor S. G. Sumner Physics Department University of Oklahoma Norman, Oklahoma Dr. J. E. Glaze Institute of Aerophysics University of Toronto Toronto 5, Ontario Dr. Harold C. Gourdin Electric & Magneto Fluid Dynamics Lab. Raytheon Corporation 3579 B. Main Street Santa Ana, California	(1) (1) (1) (1) (1)	Professor Probst Division of Engineering Brown University Providence 12, Rhode Island Professor S. S. Fanner Engineering Division California Institute of Technology Pasadena 4, California Professor C. B. Millikan, Director Guggenheim Aeronautical Laboratory California Institute of Technology Pasadena 4, California Professor L. Lees Guggenheim Aeronautical Laboratory California Institute of Technology Pasadena 4, California Professor F. Ulrich Department of Physics California Institute of Technology Pasadena 4, California Professor G. Swartz Department of Mechanical Engineering Case Institute of Technology 10900 Build Avenue Cleveland 4, Ohio Professor P. Ruch Columbia University New York, New York	(1) (1) (1) (1) (1) (1)
Commanding Officer Office of Naval Research Branch Office 346 Broadway New York 13, New York	(1)	Elmer G. Johnson, Chief Fluid Dynamics Facilities Branch Aeronautical Research Laboratory Wright-Patterson Air Force Base Ohio United States Army Research Office (Durham) Box 28, Duke Station Durham, North Carolina Commanding General Aberdeen Proving Ground, Maryland Attn: Technical Library (BSL) Dr. J. H. Frazer Internal Ballistics Laboratory Aberdeen Proving Ground, Maryland	(1) (1) (1) (1)	Professor S. L. Van Goshan Department of Aeronautical and Astronautical Engineering Ohio State University 3036 Neil Avenue Columbus 10, Ohio Professor Antonio Perri Aerodynamics Laboratory Polytechnic Institute of Brooklyn 537 Atlantic Avenue Brooklyn, New York Professor S. G. Sumner Physics Department University of Oklahoma Norman, Oklahoma Dr. J. E. Glaze Institute of Aerophysics University of Toronto Toronto 5, Ontario Dr. Harold C. Gourdin Electric & Magneto Fluid Dynamics Lab. Raytheon Corporation 3579 B. Main Street Santa Ana, California	(1) (1) (1) (1) (1)	Professor Probst Division of Engineering Brown University Providence 12, Rhode Island Professor S. S. Fanner Engineering Division California Institute of Technology Pasadena 4, California Professor C. B. Millikan, Director Guggenheim Aeronautical Laboratory California Institute of Technology Pasadena 4, California Professor L. Lees Guggenheim Aeronautical Laboratory California Institute of Technology Pasadena 4, California Professor F. Ulrich Department of Physics California Institute of Technology Pasadena 4, California Professor G. Swartz Department of Mechanical Engineering Case Institute of Technology 10900 Build Avenue Cleveland 4, Ohio Professor P. Ruch Columbia University New York, New York	(1) (1) (1) (1) (1) (1)
Commanding Officer Office of Naval Research Branch Office 1030 East Green Street Pasadena 1, California	(1)	Commanding General Aberdeen Proving Ground, Maryland Attn: Technical Library (BSL) Dr. J. H. Frazer Internal Ballistics Laboratory Aberdeen Proving Ground, Maryland Dr. C. W. Longene Technical Director Ballistic Research Laboratories Aberdeen Proving Ground, Maryland Dr. J. Starnberg Ballistics Research Laboratory Aberdeen Proving Ground, Maryland Dr. P. D. Bennett Interior Ballistics Laboratory BSL Aberdeen Proving Ground, Maryland Army Rocket and Guided Missile Agency Research Laboratory, MB Operations Attn: GEMM-DB Redstone Arsenal, Alabama Chief Defense Atomic Support Agency Washington 25, D. C.	(1) (1) (1) (1) (1) (1) (1)	Professor S. L. Van Goshan Department of Aeronautical and Astronautical Engineering Ohio State University 3036 Neil Avenue Columbus 10, Ohio Professor Antonio Perri Aerodynamics Laboratory Polytechnic Institute of Brooklyn 537 Atlantic Avenue Brooklyn, New York Professor S. G. Sumner Physics Department University of Oklahoma Norman, Oklahoma Dr. J. E. Glaze Institute of Aerophysics University of Toronto Toronto 5, Ontario Dr. Harold C. Gourdin Electric & Magneto Fluid Dynamics Lab. Raytheon Corporation 3579 B. Main Street Santa Ana, California	(1) (1) (1) (1) (1) (1)	Professor Probst Division of Engineering Brown University Providence 12, Rhode Island Professor S. S. Fanner Engineering Division California Institute of Technology Pasadena 4, California Professor C. B. Millikan, Director Guggenheim Aeronautical Laboratory California Institute of Technology Pasadena 4, California Professor L. Lees Guggenheim Aeronautical Laboratory California Institute of Technology Pasadena 4, California Professor F. Ulrich Department of Physics California Institute of Technology Pasadena 4, California Professor G. Swartz Department of Mechanical Engineering Case Institute of Technology 10900 Build Avenue Cleveland 4, Ohio Professor P. Ruch Columbia University New York, New York	(1) (1) (1) (1) (1) (1)
Director Naval Research Laboratory Washington 25, D. C. Attn: Code 2000 2000 7611 (Dr. A.C. Kuhl)	(6) (1) (1)	Dr. C. W. Longene Technical Director Ballistic Research Laboratories Aberdeen Proving Ground, Maryland Dr. J. Starnberg Ballistics Research Laboratory Aberdeen Proving Ground, Maryland Dr. P. D. Bennett Interior Ballistics Laboratory BSL Aberdeen Proving Ground, Maryland Army Rocket and Guided Missile Agency Research Laboratory, MB Operations Attn: GEMM-DB Redstone Arsenal, Alabama Chief Defense Atomic Support Agency Washington 25, D. C.	(1) (1) (1) (1) (1) (1)	Professor S. L. Van Goshan Department of Aeronautical and Astronautical Engineering Ohio State University 3036 Neil Avenue Columbus 10, Ohio Professor Antonio Perri Aerodynamics Laboratory Polytechnic Institute of Brooklyn 537 Atlantic Avenue Brooklyn, New York Professor S. G. Sumner Physics Department University of Oklahoma Norman, Oklahoma Dr. J. E. Glaze Institute of Aerophysics University of Toronto Toronto 5, Ontario Dr. Harold C. Gourdin Electric & Magneto Fluid Dynamics Lab. Raytheon Corporation 3579 B. Main Street Santa Ana, California	(1) (1) (1) (1) (1)	Professor Probst Division of Engineering Brown University Providence 12, Rhode Island Professor S. S. Fanner Engineering Division California Institute of Technology Pasadena 4, California Professor C. B. Millikan, Director Guggenheim Aeronautical Laboratory California Institute of Technology Pasadena 4, California Professor L. Lees Guggenheim Aeronautical Laboratory California Institute of Technology Pasadena 4, California Professor F. Ulrich Department of Physics California Institute of Technology Pasadena 4, California Professor G. Swartz Department of Mechanical Engineering Case Institute of Technology 10900 Build Avenue Cleveland 4, Ohio Professor P. Ruch Columbia University New York, New York	(1) (1) (1) (1) (1) (1)
Commanding Officer and Director David Taylor Model Basin Washington 25, D. C. Attn: Dr. F.H. Frankel (Code 108A) Aerodynamics Laboratory Library	(1) (1)	Dr. P. D. Bennett Interior Ballistics Laboratory BSL Aberdeen Proving Ground, Maryland Army Rocket and Guided Missile Agency Research Laboratory, MB Operations Attn: GEMM-DB Redstone Arsenal, Alabama Chief Defense Atomic Support Agency Washington 25, D. C.	(1) (1)	Professor S. L. Van Goshan Department of Aeronautical and Astronautical Engineering Ohio State University 3036 Neil Avenue Columbus 10, Ohio Professor Antonio Perri Aerodynamics Laboratory Polytechnic Institute of Brooklyn 537 Atlantic Avenue Brooklyn, New York Professor S. G. Sumner Physics Department University of Oklahoma Norman, Oklahoma Dr. J. E. Glaze Institute of Aerophysics University of Toronto Toronto 5, Ontario Dr. Harold C. Gourdin Electric & Magneto Fluid Dynamics Lab. Raytheon Corporation 3579 B. Main Street Santa Ana, California	(1) (1)	Professor Probst Division of Engineering Brown University Providence 12, Rhode Island Professor S. S. Fanner Engineering Division California Institute of Technology Pasadena 4, California Professor C. B. Millikan, Director Guggenheim Aeronautical Laboratory California Institute of Technology Pasadena 4, California Professor L. Lees Guggenheim Aeronautical Laboratory California Institute of Technology Pasadena 4, California Professor F. Ulrich Department of Physics California Institute of Technology Pasadena 4, California Professor G. Swartz Department of Mechanical Engineering Case Institute of Technology 10900 Build Avenue Cleveland 4, Ohio Professor P. Ruch Columbia University New York, New York	(1) (1)
Chief, Bureau of Naval Weapons Department of the Navy Washington 25, D. C. Attn: Code WNA-612 NAW-3 WNA-4	(1) (1) (1)	Dr. P. D. Bennett Interior Ballistics Laboratory BSL Aberdeen Proving Ground, Maryland Army Rocket and Guided Missile Agency Research Laboratory, MB Operations Attn: GEMM-DB Redstone Arsenal, Alabama Chief Defense Atomic Support Agency Washington 25, D. C.	(1) (1)	Professor S. L. Van Goshan Department of Aeronautical and Astronautical Engineering Ohio State University 3036 Neil Avenue Columbus 10, Ohio Professor Antonio Perri Aerodynamics Laboratory Polytechnic Institute of Brooklyn 537 Atlantic Avenue Brooklyn, New York Professor S. G. Sumner Physics Department University of Oklahoma Norman, Oklahoma Dr. J. E. Glaze Institute of Aerophysics University of Toronto Toronto 5, Ontario Dr. Harold C. Gourdin Electric & Magneto Fluid Dynamics Lab. Raytheon Corporation 3579 B. Main Street Santa Ana, California	(1) (1)	Professor Probst Division of Engineering Brown University Providence 12, Rhode Island	

Professor R. Anderson  
Physics Department  
New York University  
University Heights  
New York 53, New York (1)

Professor J. J. Stoker  
Institute of Mathematical Sciences  
4 Washington Place  
New York 3, New York (1)

Professor J. F. Ludloff  
Guggenheim School of Aeronautics  
New York University  
New York 53, New York (1)

Professor Ali Dulent Combel  
Department of Mechanical Engineering  
Northwestern University  
Evanston, Illinois (1)

Dr. Aaron E. Bellinger  
The Ohio State University  
Rachet Research Laboratory  
2340 Olentangy River Road  
Columbus 10, Ohio (1)

Professor R. S. Stoner  
Department of Physics (Ommond)  
Pennsylvania State University  
University Park, Pennsylvania (1)

Professor W. D. Hayes  
Perceptual Research Center  
Princeton, New Jersey (1)

Professor J. Engdahl  
Department of Aeronautical Engineering  
Princeton University  
Princeton, New Jersey (1)

Professor L. Spitzer, Jr.  
Princeton University Observatory  
Princeton, New Jersey (1)

Professor J. Pan  
Department of Aeronautical Engineering  
Rensselaer Polytechnic Institute  
Troy, New York (1)

Dr. C. Cook  
Stanford Research Institute  
Menlo Park, California (1)

Professor D. Gilberg  
Applied Mathematics and Statistics  
Laboratory  
Stanford University  
Stanford, California (1)

Department of Aeronautical Engineering  
Stanford University  
Stanford, California (1)

Professor D. Ratzelander  
Department of Aeronautical Engineering  
Stanford University  
Stanford, California (1)

Professor Allen Chapman, Chairman  
Mechanical Engineering Department  
Jilliam H. Rice Institute  
Box 1093  
Houston 1, Texas (1)

Professor H. Malt  
Division of Aeronautical Sciences  
University of California  
Berkeley 4, California (1)

Professor J. A. Sierensberg  
University of California  
Berkeley, California (1)

Professor A. E. Oppenheim  
Division of Mechanical Engineering  
University of California  
Berkeley 4, California (1)

Dr. S. A. Olgate  
Radiation Laboratory  
University of California  
Livermore, California (1)

Dr. E. Post  
Radiation Laboratory  
University of California  
Livermore, California (1)

Dr. Buff  
Los Alamos Scientific Laboratory  
Los Alamos, New Mexico (1)

Dr. J. L. Tuck  
Physics Division  
Los Alamos Scientific Laboratory  
University of California  
Los Alamos, New Mexico (1)

Dr. R. G. Sheffield  
4114 Washington Street  
Midland, Michigan (1)

Professor A. P. Charvat  
Department of Engineering  
University of California  
Los Angeles 24, California (1)

Dean L.H.E. Beiler  
College of Engineering  
U.C.L.A.  
Los Angeles, California (1)

Dr. R. Chuan  
Engineering Center  
University of Southern California  
University Park  
Los Angeles 7, California (1)

Professor J. Kaplan  
Department of Physics  
U.C.L.A.  
Los Angeles, California (1)

Aeronautical Sciences Laboratory  
University of California  
Richmond Field Station  
1301 South 40th Street  
Richmond, California (1)

Professor R. Bonnelly  
Institute for the Study of Metals  
University of Chicago  
5640 Ellis Avenue  
Chicago 37, Illinois (1)

Professor R. P. Harrington, Head  
Department of Aeronautical Engineering  
University of Cincinnati  
Cincinnati 21, Ohio (1)

Professor T. L. Bailey  
Department of Physics  
University of Florida  
Gainesville, Florida (1)

Dr. H. Kendall Reynolds  
Physics Department  
University of Houston  
3801 Cullen Boulevard  
Houston, Texas (1)

Professor A. H. Hub  
114 Digital Computer Laboratory  
University of Illinois  
Urbana, Illinois (1)

Professor R. S. Stillwell, Chairman  
Department of Aeronautical and  
Astronautical Engineering  
University of Illinois  
Urbana, Illinois (1)

Professor H. E. Gries  
University of Maryland  
College Park, Maryland (1)

Professor Burgess  
Institute for Fluid Mechanics and  
Applied Mathematics  
University of Maryland  
College Park, Maryland (1)

Professor G. E. Uhlenhuth  
The Rockefeller Institute  
New York 21, New York (1)

Professor A. Baer  
Department of Aeronautical Engineering  
University of Michigan  
Ann Arbor, Michigan (1)

Professor V. C. Nelson  
Department of Aeronautical Engineering  
University of Michigan  
Ann Arbor, Michigan (1)

Professor Horro M. Singel  
Radiation Laboratory  
The University of Michigan  
201 Catherine Street  
Ann Arbor, Michigan (1)

Dr. H. Ross E. Hoffman  
Director of Science Service  
Faculty Exchange  
University of Oklahoma  
Norman, Oklahoma (1)

Dr. H. A. Stoudt  
Physics Department  
University of Pittsburgh  
Pittsburgh, Pennsylvania (1)

Professor T. H. Donahue  
University of Pittsburgh  
Pittsburgh, Pennsylvania (1)

H. J. Thompson  
Defense Research Laboratory  
University of Texas  
P. O. Box 8809  
Austin, Texas (1)

The Library  
Institute of Aeronautics  
University of Toronto  
Toronto 5, Ontario (1)

Professor H. A. Cook, Director  
Experimental Research Group  
University of Utah  
Salt Lake City, Utah (1)

A. R. Eubank, Director  
Research Laboratories for the  
Engineering Sciences  
Thurston Hall  
University of Virginia  
Charlottesville, Virginia (1)

Department Librarian  
Department of Aeronautical Engineering  
University of Washington  
Seattle 5, Washington (1)

Professor J. O. Hirschfelder  
Theoretical Chemistry Laboratory  
University of Wisconsin  
Post Office Box 2127  
Madison 5, Wisconsin (1)

Aeroflex-General Corporation  
Attn: Ryan T. Grevier, Librarian  
6352 N. Irwindale Avenue  
Azusa, California (1)

William H. Burman, Head  
Aero-Analytic Department  
2400 East El Segundo Boulevard  
El Segundo, California (1)

American Machine and Foundry Company  
Attn: Mechanics Research Department  
75-1 B. Hatcher Avenue  
Riles, Illinois (1)

Australian Weapons Research  
Establishment  
c/o Defense Research and Development  
Australian Joint Service Staff  
P.O. Box 4837  
Washington 8, D. C. (1)

Dr. S. C. Lin  
AVCO-Everett Research Laboratory  
2385 Revere Beach Parkway  
Everett 49, Massachusetts (1)

AVCO-Everett Research Laboratory  
Attn: Library  
2385 Revere Beach Parkway  
Everett 49, Massachusetts (1)

Mr. W. T. Hamilton (M.S. 15-34)  
Chief of Flight Technology  
The Boeing Company  
Aero-Space Division  
P.O. Box 3707  
Seattle 24, Washington (1)

Technical Information Center  
Chance Vought Corporation  
P.O. Box 3907  
Dallas 22, Texas (1)

Dr. A. E. S. Green  
Chief of Physics  
General Dynamics-Corvair  
Mail Room 4-112  
San Diego 12, California (1)

H.A. Baird, G-25  
Douglas Aircraft Company, Inc.  
3000 Ocean Park Boulevard  
Santa Monica, California (1)

Patchell Engine and Aircraft Company  
Guided Missile Division  
Yonkers, Long Island, New York (1)

Dr. J. S. Isenberg  
Technical Director  
Flight Science Laboratory, Inc.  
1963 Sheridan Drive  
Buffalo 25, New York (1)

Dr. V. Pitt  
General Atomic  
P.O. Box 400  
San Diego 12, California (1)

Dr. Lawrence I. Chasen, Manager  
HNB Library  
General Electric Company HNB  
3190 Chestnut Street  
Philadelphia 1, Pennsylvania (1)

Dr. H. Low  
General Electric Company  
3750 D Street  
Philadelphia 24, Pennsylvania (1)

Dr. Hagmann  
General Electric Company  
Research Laboratory  
P.O. Box 1888  
Schenectady, New York (1)

Dr. Donald R. White  
General Electric Company  
Research Laboratory  
P.O. Box 1888  
Schenectady, New York (1)

Dr. Alpher  
General Electric Company  
Research Laboratory  
P.O. Box 1888  
Schenectady, New York (1)

Dr. G. Wagner  
General Mills, Inc.  
Electronics Group  
2003 E. Hennepin Avenue  
Minneapolis 13, Minnesota (1)

Dr. Robert H. Hillyer, Jr.  
Research Laboratories  
General Motors Corporation  
12 Mile and Wood Road  
Warren, Michigan (1)

Engineering Library  
Grumman Aircraft Engineering Corp.  
Bethpage, Long Island, New York (1)

Mr. S. O. Harriott  
Hughes Aircraft Company  
Building 8/111 Station 1000  
Culver City, California (1)

Mr. Phillip Hosenberg  
Hydronics, Inc.  
200 Monroe Street  
Rockville, Maryland (1)

Mr. Marshall P. Tulin  
Hydronics, Inc.  
200 Monroe Street  
Rockville, Maryland (1)

Dr. S. Cohen  
IBM Research Center  
P.O. Box 218  
Yorktown Heights, New York (1)

Mr. Donald Hult  
Chief Scientist  
Lockheed Missiles and Space Company  
P.O. Box 500  
Sunnyvale, California (1)

Engineering Library  
The Harquardt Corporation  
16555 Station  
Van Nuys, California (1)

Mr. L. G. Cooper  
The Martin Company  
DAWG; Research Library, A-52  
P.O. Box 178  
Denver 1, Colorado (1)

Dr. S. L. Levy, Director  
Midwest Research Institute  
Physics and Mathematics Division  
425 Valher Boulevard  
Kansas City 10, Missouri (1)

Midwest Research Institute  
Attn: Library  
425 Valher Boulevard  
Kansas City 10, Missouri (1)

Dr. H. C. Freeman  
National Physical Laboratory  
Teddington, Middlesex, England (1)

Mr. E. Orlik-Mishermann  
Head, Velocity Aerodynamics  
National Aeronautics Establishment  
National Research Council  
Ottawa 2, Canada (1)

Dr. E. S. van Driest  
North American Aviation, Inc.  
Space and Information Systems Division  
12214 Lakewood Boulevard  
Downey, California (1)

Northrop Corporation  
Research Division  
Attn: Technical Information  
1001 E. Broadway  
Northridge, California (1)

Ram Wooldridge Corporation  
A Division of Thompson Ram Wooldridge  
Incorporation  
Attn: Technical Information Services  
6033 Fallbrook Avenue  
Compton Park, California (1)

Mr. E. Williams  
Road Corporation  
1700 Main Street  
Santa Monica, California (1)

Dr. E. W. Perry, Chief  
Re-entry Simulation Laboratory  
Applied Research & Development  
Republic Aviation Corporation  
Farmdale, New York (1)

Republic Aviation Corporation  
Attn: Mr. E. A. Stidovich  
Space Systems and Research  
Farmdale, Long Island, New York (1)

Dr. L. P. Crabtree  
Ministry of Aviation  
Royal Aircraft Establishment  
Aerodynamics Department  
Farnborough, Hants, England (1)

Dr. J. D. Shreve, Jr. 5112  
Sandia Corporation  
Sandia Base  
Albuquerque, New Mexico (1)

Mr. C. C. Hudson  
Sandia Corporation  
Sandia Base  
Albuquerque, New Mexico (1)

Mr. E. S. Cline, Director  
Physical Research  
Sandia Corporation  
Sandia Base  
Albuquerque, New Mexico (1)

Dr. R. S. Low  
Manager, God Dymond  
Space Sciences Laboratory  
Space Technology Center  
King of Prussia, Pennsylvania (1)

Dr. A. Ritter  
Thorn Advanced Research  
Thorn, Incorporated  
Ithaca, New York (1)

United Aircraft Corporation  
Research Laboratories  
400 Main Street  
West Hartford 5, Connecticut (1)

Dr. Donald E. Buevart, Director  
Ponder Laboratories  
Standard Research Institute  
Menlo Park, California (1)

Dr. Donald  
Standard Research Institute  
Ponder Laboratories  
Menlo Park, California (1)

Hitachi, Incorporated  
200 Putnam Avenue  
Cambridge 20, Massachusetts  
Attn: Dr. E. S. Rubin (1)

AVCO Research & Advanced Development Div.  
201 Lowell Street  
Wilmington, Massachusetts  
Attn: Chief of Aerodynamics